Development of High-Performance Resonant Accelerometers

by

Erfan Ghaderi

M.Sc. (Electrical Engineering), Sharif University of Technology, 2017
B.Sc. (Electrical Engineering), Razi University, 2012

Thesis Submitted in Partial Fulfillment of the
Requirements for the Degree of
Doctor of Philosophy

in the
School of Mechatronic Systems Engineering
Faculty of Applied Sciences

SIMON FRASER UNIVERSITY
Spring 2024

Declaration of Committee

Name:	**Erfan Ghaderi**
Degree:	**Doctor of Philosophy**
Title:	**Development of High-performance Resonant Accelerometers**
Committee:	**Chair: Siamak Arzanpour** Professor, Mechatronic Systems Engineering
	Behraad Bahreyni Supervisor Professor, Mechatronic Systems Engineering
	Ash M. Parameswaran Committee Member Professor, Engineering Science
	Michael Adachi Committee Member Associate Professor, Engineering Science
	Farshid Najafi Examiner Assistant Professor, Mechatronic Systems Engineering
	Sheng Shian Li External Examiner Professor, Institute of NanoEngineering and MicroSystems National Tsing Hua University

Abstract

Micro-Electro-Mechanical-System accelerometers have been integral in various applications for years due to their precision, versatility, and compact size. They have found relevance in sectors ranging from aerospace to inertial sensing, navigation systems, wearables, the Internet of Things (IoT), precision machinery sensing, seismometers, and gravimetry. Substantial research has been conducted in these areas. Among different transduction methods, resonant accelerometers are known for their high precision and dynamic range. However, a notable limitation is their sensitivity. The acceleration in these devices is converted into an axial force on a micro-resonator. Due to the inherent stiffness of these structures, there is a compromise in their sensitivity.

To address this, techniques have been investigated to enhance the sensitivity, aiming to produce a high-performance accelerometer. We introduced "process-agnostic structures" - innovative modifications intended to heighten the sensitivity of microbeams. By altering the boundary conditions of these beams, moving from conventionally clamped beams to pinned beams or free beams, sensitivity has been substantially improved – up to a four-fold increase. Furthermore, these devices have a superior quality factor. A significant advantage of these modifications is their universal applicability. They are compatible with any fabrication process prevalent in the industry and academia, negating the need for material or interface electronics changes.

Additionally, in our quest to amplify mechanical sensitivity, resonator beams with micro-lever structures have been combined. This integration was projected to enhance the sensitivity further. After simulations and fabrication of the experimental devices using Deep Reactive Ion Etching processes, a combination was found that could enhance sensitivity by approximately 30%. Our research, backed by simulations and experimental testing, validates our design approach. We have achieved substantial advancements in resonant accelerometers.

Keywords: MEMS Accelerometer; High Sensitivity; Resonant Sensing; Micro-beams; Micro-levers

Summary for Lay Audience

Have you ever wondered how your phone knows when to switch from portrait to landscape mode or how your car's airbag system knows when to deploy in an accident?

The answer is ***sensors***!

Sensors are devices that can detect environmental changes and turn them into electrical signals that can be read and interpreted through *transduction*. Think of a sensor as a type of "translator" that can take information from the physical world (like light, sound, temperature, pressure, or motion) and convert it into a language that can be *sensed* by a computer or other electronic device. They come in many different types and are used in various applications.

Resonant sensors are a type of sensor that uses the concept of resonance frequency for its transduction method. To understand how resonance works, think of a guitar string. When you pluck a guitar string, it vibrates and creates a sound. This is why a guitar string will produce a louder and more sustained sound when you play it at its resonant frequency. Same as a child on a swing. If you push the child at the right frequency, they will go higher and higher with each swing. This frequency is the child's resonant frequency for swinging. Similarly, objects in the physical world have their natural resonance frequency.

The sound's pitch, or frequency, in the guitar, is determined by the string's length, thickness, and tension. If any of these parameters change, the resonance frequency of the string will change. Similarly, in sensors, when the environment around them changes, the frequency of the sensor's vibration may also change. *The sensor can detect and measure environmental changes by measuring its resonant frequency.*

A MEMS (Micro-Electro-Mechanical Systems) sensor is a tiny device that combines electrical and mechanical components on a small scale. These devices are made using micro-fabrication techniques, which allow them to be manufactured with incredible precision and accuracy. A MEMS accelerometer is a tiny device that can measure acceleration, the rate at which something is speeding up or slowing down. MEMS accelerometers are used in a wide range of applications, including smartphones and other electronic devices, to detect changes in orientation and motion. For example, when you

rotate your phone, the MEMS accelerometer can detect the change in orientation and adjust the display accordingly. They are also used in automotive safety systems to detect changes in speed and direction and activate safety features like airbags.

In MEMS resonant accelerometers, we can observe a resonant structure that vibrates and moves, with the resonator connected to a mass called *proof mass.* As the proof mass moves, it exerts a force on the resonator, thereby altering the resonance frequency of the beam. This change in resonance frequency is similar to the change in tension on a guitar string. MEMS resonant accelerometers are fascinating structures that utilize the principles of resonance to detect movement and vibration. These sensors are susceptible and are used in various applications, from automotive systems to medical devices. As technology advances, we can expect to see even more sophisticated MEMS resonant accelerometers that push the boundaries of what is possible in motion and vibration sensing.

However, in MEMS resonant accelerometers, we are dealing with structures far smaller and stiffer than guitar strings, and it is challenging to employ a large force from the proof mass to the resonant sensor. To overcome this issue, MEMS accelerometers contain three main parts - the resonator, proof mass, and amplification structure. The amplification structure is responsible for amplifying the force exerted by the proof mass to increase the sensitivity of the sensor. Additionally, interface electronics are used to measure the resonance frequencies of the accelerometer. The fabrication of MEMS resonant accelerometers is challenging due to the small size of these structures. By leveraging this technology, we can create susceptible and accurate sensors capable of detecting even the slightest movements and vibrations.

This thesis embarks on an exciting journey through the world of high-performance MEMS resonant accelerometers. With a keen eye on design, fabrication, and characterization, we investigated the factors that impact the performance of these accelerometers. We explored various design factors and their effects on sensitivity. Through innovation and experimentation, we developed novel structures that vastly improved the sensitivity of these accelerometers. We also examined methods to amplify forces within these structures, further increasing their sensitivity. Fabrication of these devices posed unique challenges, which we discussed in detail—carefully comparing our novel systems to state-of-the-art technologies.

Dedication

I dedicate this thesis to Ph.D. students who lost their life in PS752 flight.

Acknowledgements

I extend my gratitude to a multitude of individuals whose support and guidance have been invaluable throughout the course of my project. Their contributions have been diverse yet equally significant, and it is with great appreciation that I acknowledge each one.

First and foremost, I must express my appreciation for my supervisor. His patience and mental fortitude have been a constant source of inspiration during my work. His support has not only facilitated the technical aspects of my project but has also contributed to my personal growth and resilience.

I am particularly thankful to Dr. Soheil Azimi and Dr. Qader Qureshi, who laid the groundwork for my project. Their teachings at the initial stages were crucial, equipping me with the necessary skills and knowledge to embark on this challenging yet rewarding journey.

To my wonderful family, thank you so much for always being there for me while I was working on my big school project, my PhD. Your help and love made everything easier and kept me going, even when things got tough. You always believed in me and cheered me on, and that means everything to me. This big win is for all of us together. I'm deeply thankful for everything you've done. *Zor Supas* Dad, Mom, Fouzieh, Kayvan, Zakieh, Somayeh, Soma, Jalal, Lida, and our dear Vina and Mahbod.

The support provided by my fellow members at Intelligent Sening Lab and friends have been a cornerstone of my journey. Their collective wisdom, encouragement, and assistance have played a pivotal role in navigating the challenges encountered along the way. The sense of community and shared purpose among us has been a source of strength and motivation.

Table of Contents

Declaration of Committee ii
Abstract iii
Summary for Lay Audience iv
Dedication vi
Acknowledgements vii
Table of Contents viii
List of Tables x
List of Figures xi

Chapter 1. Introduction 1
1.1. Motivation 1
1.2. Thesis Structure 4

Chapter 2. MEMS Accelerometers 6
2.1. MEMS Accelerometers 6
2.2. Working Mechanism 7
2.3. Sensing Mechanisms 11
2.3.1. Capacitive Accelerometers 11
2.3.2. Electron Tunneling Accelerometers 12
2.3.3. Optical Accelerometers 13
2.3.4. Thermal Accelerometers 14
2.3.5. Piezoresistive Accelerometers 14
2.3.6. Piezoelectric Accelerometers 15
2.3.7. Resonant accelerometers 16
2.4. High-performance MEMS Accelerometers 16

Chapter 3. Resonant Accelerometers 23
3.1. What Is Resonance? 23
3.2. Working Principle 24
3.2.1. Reported Resonant Accelerometers 28
3.2.2. Existing Challenges 31
3.3. Resonant Beam as Sensing Element 32
3.3.1. Effect of Beam Dimensions on Sensitivity 37
3.3.2. Effect of Vibration Modes on Sensitivity 39

Chapter 4. Modified Beam Structures for Improved Sensitivity 44
4.1. Beam Boundary Conditions and Sensitivity 44
4.2. Modified Beam Design 48
4.3. Simulations 50
4.4. Fabrication 55
4.5. Experiments 59
4.6. Summary 69

Chapter 5. Co-design of Sensing Beam and Mechanical Force Amplifier.....71
5.1. Micro-Levers.....71
5.2. Designs and Simulations.....79
5.3. Fabrication.....89
5.4. Experiments.....98
5.5. Summary.....104

Chapter 6. High-sensitivity resonant accelerometer.....105
6.1. Design.....105
6.2. Simulation.....107
6.3. Fabrication.....110
6.4. Experiments.....112
6.5. Summary.....116

Chapter 7. Conclusions and future work.....117
7.1. Contributions.....117
7.2. Future work.....118

References.....120

Appendix A. Details of Fabrication Process.....129

Appendix B. Phase Noise in Multiplier.....130

List of Tables

Table 1 Comparison between accelerometer transduction methods. 17
Table 2 Summary of some of the reported high-performance accelerometers. 20
Table 3 Summary of reported resonant accelerometers. 29
Table 4 Summary of boundary conditions for Clamped-Clamped (CC), Pinned-Pinned (PP), and Free-Free (FF) beams. 45
Table 5 Summary of the values for ξ for the first three vibration modes 46
Table 6 Summary and comparison of theoretical and simulation performances of the beams 53
Table 7 Summary of the beam performances and comparison between theory, simulation, and measurements 65
Table 8 Summary of the values for the parameters of the microlever used for theoretical calculations. 77
Table 9 Summary of the dimensions of the resonator-lever systems 86
Table 10Summary of the simulation results for the resonator-lever systems presented. 89
Table 11 Summary and comparison of the measurement results for the designs introduced in this chapter 104
Table 12 Summary of the dimensions and simulation results for three types of accelerometers, a Clamped-Clamped beam with regular lever, and two Clamped-Free beams with notched levers while the notch dimensions are different. 108

List of Figures

Figure 2-1 Mass-Spring-Damper model.....7
Figure 2-2 Typical frequency response of a mass on spring system for different values of quality factors.....9
Figure 2-3 A simple schematic of capacitive accelerometers.....12
Figure 2-4 A simple schematic of electron tunneling accelerometers. 12
Figure 2-5 A simple schematic of the optical accelerometer. 13
Figure 2-6 A simple schematic of a thermal accelerometer. 14
Figure 2-7 A simple schematic of piezoresistive accelerometer.....15
Figure 2-8 A simple schematic of a piezoresistive accelerometer.....15
Figure 2-9 A simple schematic of a resonant accelerometer. 16
Figure 2-10 Trade-offs in accelerometer design. 19
Figure 3-1 (a) The amplitude and (b) the phase response of a second-order system at resonance with different quality factors. 24
Figure 3-2 Resonator structures hile vibrating (a) beam (b) bridge 25
Figure 3-3 Different vibration modes of the bridge structure resonator (a) first in-plane mode (b) first out-of-plane mode (c) second in-plane mode (d) third in-plane mode. 26
Figure 3-4 Resonant accelerometer system. 27
Figure 3-5 Schematic of a resonant accelerometer. 27
Figure 3-6 A micro-resonator beam under the axial force 32
Figure 3-7 The deflection shape of the first resonance mode for a clamped-clamped beam solved for unity energy. 35
Figure 3-8 Change in resonance frequency versus axial force for a Silicon resonator designed around 1MHz (L=300μm, w=10μm, h=25μm). The positive values indicate the tensile force, while the negative values indicate the compressive force. 36
Figure 3-9 Deflection shape of the second resonance mode in a Clamped-Clamped resonator.....41
Figure 4-1 Defection shapes of the first resonant mode for three beams with different boundary conditions 47
Figure 4-2 Schematic of (a) Clamped-Clamped (C-C), (b) Pinned-Pinned (P-P), (c) Free-Free (F-F), and their defection shape in the first vibration mode.....49
Figure 4-3 The layout designs and simulated first mode of the vibration for resonators with Clamped-Clamped (a), Pinned-Pinned (b), Free-Free (c), Free-Free with narrower Boundary beam (d). Resonator mode deflections are shown with 50-time exaggeration. 51
Figure 4-4 the comparison between deflections of the C-C and P-P beams at the ends of the beams. 52
Figure 4-5 (a) Designed mask for fabrication (b) The design for Pinned-Pinned beam with electrode configuration.....56

Figure 4-6 SEM images of the fabricated C-C beam (a) with depiction of electrode configuration (b) the point where beam connected to the anchor as clamped boundary condition 57
Figure 4-7 SEM images of the fabricated P-P beam (a) with depiction of electrode configuration (b) the point where beam connected to the anchor as Pinned boundary condition, the extra traiangle structure is for reducing grass and overetching in DRIE step 57
Figure 4-8 SEM images of the fabricated F-F beam (a) with depiction of electrode configuration (b) the point where beam connected to the anchor as Free boundary condition, the extra triangle structure is for reducing grass and over etching in DRIE step.....58
Figure 4-9 SEM images of the fabricated F-F beam (a) with depiction of electrode configuration (b) the point where beam connected to the anchor as Free boundary condition, the extra structure between the boundary beams and the resonant beam is for reducing grass and over etching in DRIE step. 58
Figure 4-10 (a) An image of the packaged devices (b) An optical microscope image of the Free-Free beam as an example of the fabricated devices 59
Figure 4-11 the schematic of the experimental setup 60
Figure 4-12 sample response for the frequency measurement of a P-P beam after removing the feedthrough signal. 61
Figure 4-13 the shift in the resonance of the P-P beam due change in the potential difference ΔV, the corresponding electrostatic force shown at the top. ...62
Figure 4-14 Frequency response of the C-C beam and its 91 Hz shift (b) Frequency response of the P-P beam and its 180 Hz shift, (c) Frequency response of the F-F(1) beam and its 185 Hz shift, (d) Frequency response of the F-F(2) beam and its 402 Hz shift, all the frequencty shifts are due to application of $35\ \mu N$ of axial force. 64
Figure 4-15 the comparison of theory, simulation and measurements of sensitivity for (a) Clamped-Clamped, (b) Pined-Pinned, (c) Free-Free (1), and (d) Free-Free(2). In all Figures the orange line represents the curve obtained from theory, the dashed blue line represents simulation data, and the dashed red line represents the measurement data. 67
Figure 4-16 Comparison of the Quality factor for C-C, P-P and F-F(1) beams at different ambient pressure 68
Figure 4-17 Comparison of the resonance shift results for C-C and P-P beams under the same 35μN axial force at lower Q under ambient pressure of 15 Torr. ...69
Figure 5-1 microlever structure with positive force amplification 73
Figure 5-2 microlever structure with negative force amplification.....73
Figure 5-3 Schematic view of the lever with depiction of the forces and momentums [105].....75
Figure 5-4 the theoretical amplification factor versus different values for l while other parameters are set as values shown in Table 8, in the figure, the unit for horizontal axis is μm.....77
Figure 5-5 The effect of adding a resonant beam on amplification factor (Orange line) compared to a unloaded lever (Blue line), the unit for the horizontal axis is μm.....78

Figure 5-6 Schematic of the lever structure 80
Figure 5-7 Design “C-C-Lever”: Schematic of microlever structure along with a Clamped-Clamped resonator. 82
Figure 5-8 Design “F-F-Lever”: schematic of a microlever structure along with a Free-Free beam resonator 82
Figure 5-9 Design "F-F-Notched Lever": the schematic of novel micro-lever structure with a notch along with a Free-Free beam 84
Figure 5-10 Design "C-F-Notched Lever": the schematic of a Clamped-Free resonator with a notched microlever structure. 85
Figure 5-11 (a) Design (C-F beam with notched lever) in FEM simulations without input force (b) the same system with input force 88
Figure 5-12 The first vibration mode of the C-F beam attached to a lever with a notch. . 88
Figure 5-13 An example of the lever design layout and showing the resonator and force electrodes in more details. 90
Figure 5-14 Oxidized SOI wafer with 2um of oxide on surface and 2um of buried oxide 91
Figure 5-15 Photolithography step 92
Figure 5-16 RIE of Oxide Mask 92
Figure 5-17 Backside lithography and DRIE of handle layer 93
Figure 5-18 DRIE of Silicon on the device layer 94
Figure 5-19 SEM of the cross-section for DRIE 94
Figure 5-20 (a) polymers inside the gas (b) removal of the polymers after heat treatment 95
Figure 5-21 Schematic cross section of the devices after release 96
Figure 5-22 (a) devices after release and separation on VHF chuck (b) the frame that detached from the devices. 96
Figure 5-23 Schematic cross section of the devices after metallization 97
Figure 5-24 SEMs of the fabricated devices , here the Free Free beam with notched lever, Design "C". , the two extra beams within the notch are for prevention of over etching and/or grass formation during the DRIE step. 98
Figure 5-25 SEM images of the Design "D" along with details of the electrode configuration, the two extra beams within the notch are for prevention of over etching and/or grass formation during the DRIE step. 99
Figure 5-26 The schematic of the measurement setup for lever and resonant beam characterization using a lock-in amplifier, in the figure , the symbol V is for the Bias voltage 100
Figure 5-27 A measured resonance signal for a Free-Free beam 101
Figure 5-28 Measurement results of the resonance frequency for four different designs: (a) Design “A”, (b) Design “B”, (c) Design “C”, and (d) Design “D”. The results compare resonance frequencies in structures both without and with axial force. All designs are subjected to a consistent \(\Delta V \) of 25 volts, corresponding to a force of 17.5 micro-newtons. 103
Figure 6-1 Schematic of diiferetial configuration for resonant accelerometer 106

Figure 6-2 Schematic of an accelerometer with Clamped-Free beams and notched levers 107
Figure 6-3 3D Model of the simulated accelerometers (a) Accelerometer 1 described in Table 13, (b) Accelerometer 2 described in Table 13 and (c) Accelerometer 3 described in Table 13 109
Figure 6-4 Drawn layout for accelerometer #3 110
Figure 6-5 SEM images of the fabricated accelerometers 112
Figure 6-6 Schematic of the measurement detup for characterization of resonant accelerometers 113
Figure 6-7 Image of the measurement setup 113
Figure 6-8 the measured shift in the resonance frequencies while the accelerometers were rotated against the gravity. 114

Chapter 1. Introduction

In the middle of the twentieth century, and after the invention of the transistor, there was a drive to develop fabrication methods to put more transistors on a single chip (i.e., smaller transistors). Downsizing transistors would result in cheaper systems with lower power consumption and better performance. Years later, many techniques, such as photolithography, etching, and several deposition processes, were developed for miniaturization in microelectronics and semiconductor device fabrication. It was then that the field of *microfabrication* technology was born. In the 1960s, scientists used this technology to create micro-mechanisms comprised of mechanical structures and electronic devices [1]. Such machines, so-called Micro-Electro-Mechanical Systems (MEMS), became very popular and provided solutions for many challenges in sensors, actuators, and integrated technologies.

MEMS devices are desirable in many applications, such as Optics, Communication and Information, Fluidics, Microscopy and Nanoscopy, Transportation, Aerospace, and Biotechnology. Advanced branches of BioMEMS, Microfluidics, Radio Frequency (RF) MEMS, and Nano-Electro-Mechanical Systems (NEMS) provide critical components for innovative devices that shaped the modern world. Motion sensing devices are one of the fields that widely take advantage of the MEMS industry. In this thesis, we focus on the design and fabrication of sensitive accelerometers as one of the major components of such systems.

1.1. Motivation

Most MEMS technology was initially developed for the automotive industry, especially for safety systems and car control. Today, we can find more than 50 MEMS sensors in a single vehicle [2]. The second driver of MEMS technology was smartphones soon after software companies started using applications such as motion analysis, location-based services, and orientation detections in their products. With the emergence

of the Internet of Things (IoT), another wave of using MEMS devices has been observed. As the systems become more interactive and intelligent, we need more sensing and actuation devices for monitoring and intelligent control. Thus, the MEMS market is one of the promising fields in the semiconductor industry for many years to come.

In the projected timeframe from 2022 to 2029, the MEMS accelerometer sector is anticipated to witness a Compound Annual Growth Rate (CAGR) of 4.21%, increasing from USD 3.49B in 2022 to USD 4.66B in 2029 [3]. These accelerometers are becoming common in various personal electronic items such as mobile phones, wearables, gaming systems, and media devices. Laptops protect by detecting falls and shutting down the system to prevent severe damage. The growing popularity of wearable technologies, widespread adoption of the Internet of Things (IoT), and the surging demand for self-driving vehicles present fresh global opportunities for the accelerometer industry.

The importance of performance indicators varies based on the accelerometer's intended use. The following highlights several crucial metrics, though a comprehensive list of inertial sensors is available in [4].

- Sensitivity: The sensor's "Scale Factor" denotes the relationship between the accelerometer's electrical output and its mechanical input.

- Noise Floor/Resolution: Various energy dissipation mechanisms introduce noise, setting a limit on the smallest detectable signal.

- Bandwidth: The frequency range wherein the sensor retains consistent sensitivity. The 3-dB method is a standard measure for determining BW.

- Linearity: Represents the deviation of the sensor's signal from its optimal linear fit relative in its output range.

- Dynamic Range: The ratio of its maximum detectable signal to its minimum measurable signal.

- Shock Limit: This represents the largest shock the device can endure without hindering its functionality.

Given the vast array of accelerometers, each varying in cost and capability, specific metrics gain prominence based on their application. For instance, a laptop's fall detection system prioritizes a high shock limit and low energy consumption since its accelerometer isn't always active. Conversely, accelerometers monitoring building vibrations should prioritize low noise levels and broad bandwidth. The technologies designed for these applications have reached a level where they meet most sensor criteria, including cost, power, size, dependability, integration ease, performance, and production capability. Yet, there are areas where MEMS accelerometers have yet to gain widespread acceptance.

MEMS resonant accelerometers have gained significant attention in recent years due to their ability to measure accelerations with high precision and accuracy. These devices are used in various applications, including inertial navigation and aerospace applications. The traditional accelerometer designs, which rely on piezoelectric or capacitive transduction, suffer from several limitations, including low Dynamic Range (DR), high noise, and limited bandwidth. On the other hand, resonant accelerometers are based on the principle of mechanical resonance and offer several advantages over traditional designs, including high Dynamic Range, low noise, and wide bandwidth.

Due to the complexity of resonant structures, their packaging and interface electronics, they have often been dismissed in the industrial communities. However, they have recently gained significant attention, particularly for applications in gravimetry and seismic signal detection. Notably, the resonant structures are used for their high precision in aerospace and navigation systems. Scholars who have delved into the complexities of these systems acknowledge their merits, but they also recognize an inherent limitation: a compromised sensitivity. This diminished sensitivity can be attributed to the high stiffness of the resonant element in these structures, which will be discussed in detail in the following chapters. In this thesis, the primary focus is on the resonant accelerometers,

specifically exploring methodologies to enhance their sensitivity. Such advancements can pave the way for revolutionary applications across diverse sectors. In the next section, we present the thesis' structure.

1.2. Thesis Structure

The structure of this thesis is divided into six chapters. Each chapter focuses on a specific topic and builds upon previous chapters to present a high-performance MEMS resonant accelerometer analysis.

Chapter Two focuses on the literature review. It provides a review of the basic principles of MEMS accelerometers. A comparison is made between various transduction methods used in the accelerometers. This chapter also discusses high-performance MEMS accelerometers and provides a literature review of resonant type; the state-of-the-art is also discussed.

In Chapter Three, a novel approach is presented that significantly enhances the sensitivity of resonant accelerometers. The chapter delves into the beams commonly used in resonant accelerometers and explores the effects of these beams' dimensions and boundary conditions on sensitivity. We provide a simple analytical model, and a simulation modelling of the designs follows this. Furthermore, the experimental results of the structures are presented, which provide evidence of the efficacy of the proposed method.

In Chapter Four, the focus shifts towards enhancing the sensitivity of resonant accelerometers via force amplifiers. The chapter starts with a review of the various levers employed in such amplifiers, along with their contribution to the device's sensitivity. The simulations of the proposed designs and their performance are presented, with the results showcasing the potential of these new designs to enhance sensitivity. Moreover, the chapter highlights the proof of concept through experiments, further validating these structures' effectiveness in improving resonant accelerometers' sensitivity.

Chapter Five brings all the previous chapters together to design high-sensitivity resonant accelerometers. Designs, simulations, and experimental results of these devices' performance are presented.

Finally, Chapter Six concludes the thesis by defining this research work's achievements, contributions, and novel aspects. It also discusses possible improvements to the project and recommends future work.

Chapter 2. MEMS Accelerometers

2.1. MEMS Accelerometers

Accelerometers have been used in industry since the 1900s [5]. The early applications of accelerometers were in bridges, dynamometers, and aircraft. For many years, several research groups and industrial companies worked on developing different types of accelerometers for various applications. Before the invention of micromachined accelerometers, strain gauge sensors and pendulum mechanisms were widely used for measuring acceleration in the early 1970s.

The development of the first micromachined accelerometer in the late 1970s marked a significant milestone in the microelectromechanical systems (MEMS) [6]. This accelerometer was based on piezoresistive transduction and was developed using a bulk micromachining process. However, the performance of the accelerometer was limited, and researchers began exploring various transduction methods and fabrication processes to improve its performance. In the following years, a plethora of accelerometers based on different sensing mechanisms, such as capacitive [7], piezoresistive [6], piezoelectric [8], optical [9], thermal [10], tunnelling [11], quartz [12], and resonance [13] were developed, leading to a significant advancement in the field of MEMS accelerometers. There are some new transduction methods and innovative ways to measure acceleration [14]. However, the mentioned transduction remains dominant due to its performance and versatility. To enhance its capabilities, we should concentrate on the design. In this thesis, we aim to improve performance through innovative designs. In the following section, we discuss the principle of operation of these devices. We briefly discuss basic transduction methods before making a comparison between them.

2.2. Working Mechanism

Most MEMS accelerometers detect the movements with the relative displacements of a proof mass and a frame when an acceleration is applied to the frame (i.e., the package). In all cases, the detection of the acceleration signal is based on equations governing the movement of the accelerometer structure. Scientists have widely used the mass on a spring to model the behaviour of an accelerometer. In this model, the mass represents the proof mass, and the spring represents the suspension beams connecting the proof mass to the frame.

The superposition of different harmonic oscillators can model any movement or vibration in a linear system. The mass on the spring is the simplest harmonic oscillator that we can use in our models. Figure 2-1 depicts a schematic of a Mass on Spring model for accelerometer, illustrating the proof mass connected to the frame with suspension beams. we can observe the mass spring damper model where M_o is the mass and K_o is the spring constant.

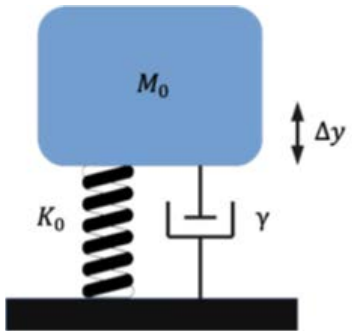

Figure 2-1 Mass-Spring-Damper model.

We initiate the model by considering Newton's second law and the equation of motion to elaborate further on the relationship between an object's motion and the forces acting upon it. We consider the equation of motion for the proof mass when it is driven by external force with excitation $F_{in} = M_0 a_{in}$; we include the damping effect with a term proportional to the speed of the proof mass, $\dot{y}$. We have [15]:

$$M_0 \frac{d^2y}{dt^2} + \gamma \frac{dy}{dt} + K_0 y = F_{in} \tag{2.1}$$

where M_0 is mass, γ is a constant relating the damping force to the speed of the proof mass, and K_0 is spring constant. We assumed that the proof mass is excited sinusoidally. By using Laplace transform, we can calculate the transfer function of the system at the steady-state:

$$H(s) = \frac{Y(s)}{A_{in}(s)} = \frac{1}{s^2 + \frac{\omega_0}{Q} s + \omega_0^2} \tag{2.2}$$

where $\omega_0 = \sqrt{K_0/M_0}$ is the natural frequency of the structure, and typically limits the device's operational bandwidth, and $Q = \omega_0/M_0\gamma$ is the quality factor, typically limits the device's transient response time. Figure 2-2 illustrates the transfer function of a second-order system normalized to the natural frequency. It displays the normalized magnitude response for five distinct quality factor values. When accelerometer is subjected to input acceleration a_{in}, then the displacement of the proof-mass, Δy, using the Hook's law is given by:

$$\Delta y(s = 0) = \frac{M_0 a_{in}}{K_0} = \frac{a_{in}}{\omega_0^2} \tag{2.3}$$

As we can see from the Equation (2.3), the sensitivity of the system and its bandwidth (i.e., resonance frequency) are reversely proportional, which is one of the main challenges in designing the high-performance accelerometers.

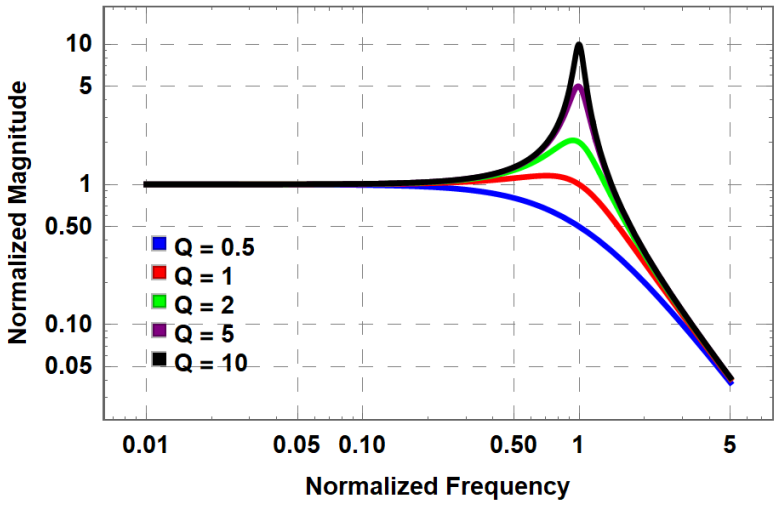

Figure 2-2 Typical frequency response of a mass on spring system for different values of quality factors.

Assuming that the voltage is the output of the system, the sensitivity of the device can be formulated as the rate of change of the voltage at the output to the input acceleration signal. The overall sensitivity is given by:

$$S_{a_{in}}^{Vout} = \frac{\partial V_{out}}{\partial a_{in}} = \frac{\partial V_{out}}{\partial y} . \frac{\partial y}{\partial a_{in}} = \frac{\partial V_{out}}{\partial y} . \frac{1}{\omega_0^2} \tag{2.4}$$

Designing a system with a low noise is another challenge of developing a high-performance accelerometer. The total noise of the system consists of two parts: Mechanical and Electrical noise. The intrinsic mechanism of mechanical noise is thermal noise. The force noise density can be calculated by [16]:

$$F_{noise} = \sqrt{4K_B T\gamma} \tag{2.5}$$

where K_B is Boltzmann constant, T is temperature, $\gamma = \sqrt{K_0 M_0}/Q = M_0\omega_0/Q$ is mechanical damping, K_0 is the structure stiffness of the accelerometer, and Q is the quality factor. As we can see from Equation (2.5), one of the ways to decrease the thermal noise is to increase the quality factor, in other words, using vacuum packaging to decrease the damping. The mechanical noise equivalent acceleration, here we show it with a_{nM}, can be calculated by [17]:

$$a_{nM} = \frac{F_{noise}}{M_0} = \sqrt{\frac{4K_B T \omega_0}{M_0 Q}} \tag{2.6}$$

In addition to mechanical noise, electronic noise adversely affects the performance of the accelerometer sensors. Three significant types of noise contribute to the electronic noise: (1) Thermal noise floor that has an approximate constant magnitude as a function of frequency caused by fluctuation in carrier densities, this type of noise is related to the temperature, (2) Flicker noise that nearly all electronic devices exhibit and it is inversely proportional to frequency ($1/f$), this type of noise caused by energy trap bands in semiconductor devices, and (3) Electrons in a conductor don't flow smoothly but move with varying energy across barriers, similar to a ball rolling over bumps. This irregular motion causes variations in current, resulting in noise. Semiconductors experience more of this "shot noise" due to increased barriers and higher currents or wider bandwidths amplify it.

Since electronic noise and mechanical noise are assumed to be independent sources of noise, we can calculate the total noise equivalent acceleration (a_{nT}) by taking the square root of summation of the mechanical noise equivalent acceleration (a_{nM}) square and electrical noise equivalent acceleration (a_{nE}) square:

$$a_{nT} = \sqrt{a_{nM}^2 + a_{nE}^2} \tag{2.7}$$

The upcoming section will cover common transduction methods used in accelerometer design. However, the discussion on resonant accelerometers will be reserved for next chapter, where we will delve into the topic in greater detail. In this section, we will focus on sensing mechanisms and compare their performance based on concepts introduced earlier.

2.3. Sensing Mechanisms

Movements of the proof mass can be detected through various transduction methods such as capacitive, piezoresistive, tunnelling, and optical. A brief description of different transduction methods is presented to help understand the technological advancements in MEMS accelerometers. These methods can be classified into two major categories:

(a) Displacement-based measurement

- Capacitive
- Electron tunneling
- Optical
- Thermal

(b) Stress based measurement

- Piezoresistive
- Piezoelectric
- Resonance

While most of the devices can be grouped into two mentioned categories, it is essential to acknowledge that some devices do not fit these classifications.

2.3.1. Capacitive Accelerometers

Capacitive accelerometers are a popular type that used in various applications. These accelerometers measure input signal by detecting changes in capacitance between two electrodes. One electrode is stationary, while the other is part of a movable proof mass. The movement of the proof mass causes a change in a parameter between the electrodes, either the gap or the overlap, depending on the structure, resulting in a change in capacitance and allowing for the measurement of acceleration. Figure 2-3 provides a simple schematic of a capacitive accelerometer with a proof mass attached to the frame using suspension beams, demonstrating how changes in the gap g between the proof

mass and the electrode result in changes in capacitance ΔC and input acceleration measurements a_{in}.

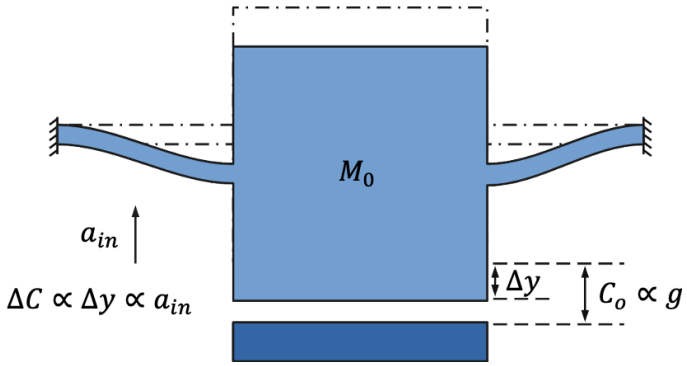

Figure 2-3 A simple schematic of capacitive accelerometers.

2.3.2. Electron Tunneling Accelerometers

Electron tunnelling accelerometers are highly sensitive and measure acceleration based on the electron tunnelling between a tip and a silicon structure that is located very close to it. The silicon structure is usually the proof mass, and as it moves, the distance between the tip and the silicon structure changes, causing a change in tunnelling current through the tip. Figure 2-4 shows a simple schematic of an electron tunnelling accelerometer with a proof mass attached to the frame using suspension beams

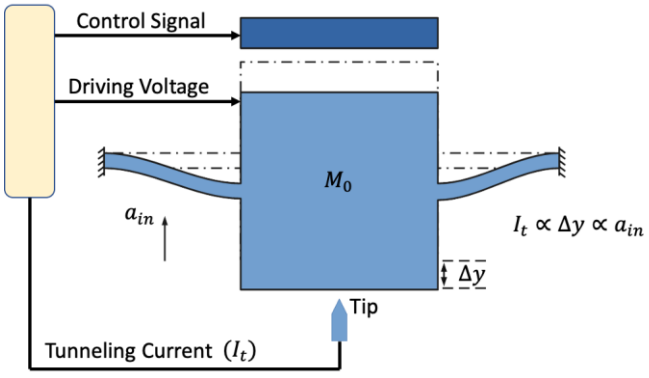

Figure 2-4 A simple schematic of electron tunneling accelerometers.

By measuring the change in tunnelling current, I_t, the amount of displacement can be determined, Δy, which is proportional to the input acceleration, a_{in}. To maintain a certain distance between the tip and proof mass, this accelerometer operates in a closed loop and uses an actuator to apply a control signal to the proof mass.

2.3.3. Optical Accelerometers

The optical accelerometer operates by detecting changes in optical properties caused by motion. In order to measure the displacement of the proof mass, an optical fiber is incorporated into the structure as seen in Figure 2-5.

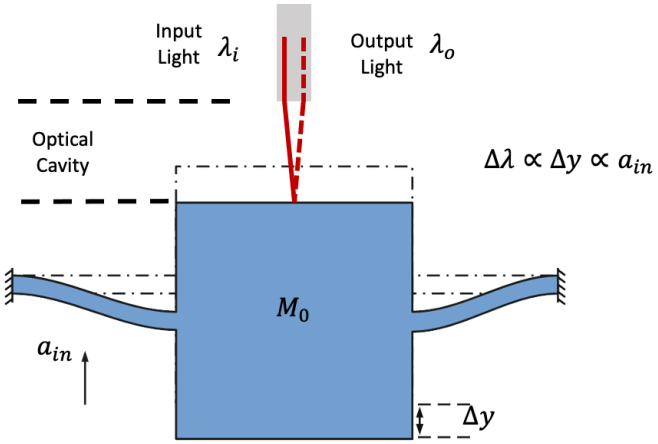

Figure 2-5 A simple schematic of the optical accelerometer.

This creates the cavity of the Fabry-Perot interferometer (FPI), which acts as a two-beam interferometer with an optical path difference equal to twice the distance between the fibre and silicon. The readout beam is sent through the optical fibre and reflects on the FPI cavity. Any variation in the FP cavity length leads to a wavelength shift of this spectrum, making it spectrally modulated.

2.3.4. Thermal Accelerometers

Thermal accelerometers utilize thermal energy gradients within structures by detecting alterations in energy flow. The depicted figure demonstrates a possible configuration for thermal sensing, comprising two heatsinks and a proof mass suspended by two beams from a frame. When we heat the proof mass, it becomes hot; the gap between the heatsinks changes as it moves. This movement triggers a leakage of thermal energy, Q_t, from the proof mass to one of the heatsinks, which we can detect by noting temperature changes between them. By quantifying the displacement, we can derive the acceleration.

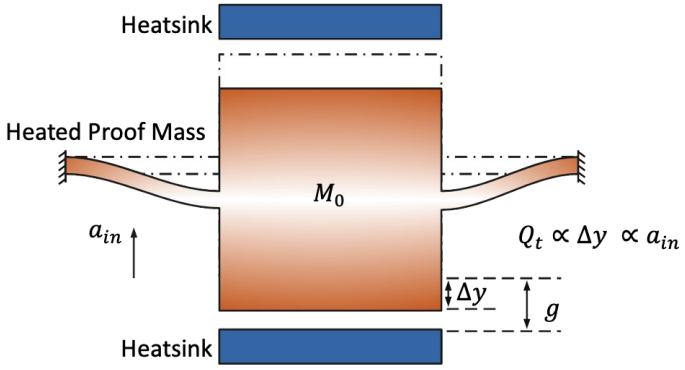

Figure 2-6 A simple schematic of a thermal accelerometer.

2.3.5. Piezoresistive Accelerometers

So far, all the accelerometers discussed were displacement-based. However, another type of accelerometer, stress-based accelerometers, is being introduced. The first type of stressed accelerometer is the piezoresistive accelerometer, which detects resistance changes R, that occur in piezoresistive material when subjected to stress. Figure 2-7 shows a simple schematic of such an accelerometer when acceleration is applied to a proof mass suspended by microbeams from a frame. As the proof mass moves, strain is generated within the beams. By measuring the change in resistance, we

can determine the stress on the piezoresistive material. Ultimately, we can establish a proportionality between the resistance and the acceleration applied to the structure.

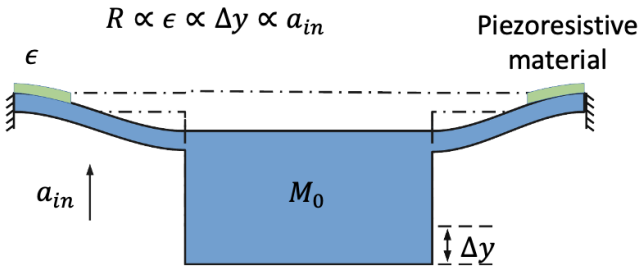

Figure 2-7 A simple schematic of piezoresistive accelerometer.

2.3.6. Piezoelectric Accelerometers

The Piezoelectric accelerometer is another type of stress-based accelerometer which detects changes in electric charges generated in piezoelectric material when subjected to stress. Figure 2-8 shows a simple schematic of such an accelerometer when acceleration is applied to a proof mass suspended by microbeams from a frame.

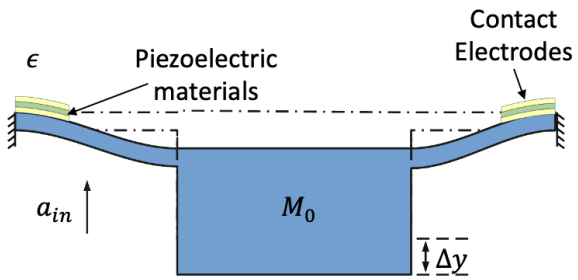

Figure 2-8 A simple schematic of a piezoresistive accelerometer.

As the proof mass moves, stress is generated within the beam by placing piezoelectric material where the beams experience the highest stress, causing the electric charge to change. We can measure this change by placing two electrodes on the top and bottom of piezoelectric material.

2.3.7. Resonant accelerometers

Resonant accelerometers are stress-based accelerometers that utilize a microbeam structure as a sensing element. When the proof mass in this device moves, Δy, stress is applied to the microbeam structure,ϵ, causing changes in its stiffness and resonance frequency, ω_r. This is illustrated in Figure 2-10.

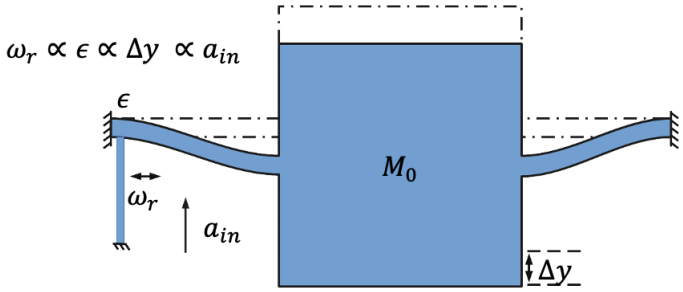

Figure 2-9 A simple schematic of a resonant accelerometer.

Many references in the literature compared these transduction methods[15], [17], [18], [19]. Table 1 summarizes the performance of various accelerometers based on their transduction methods. In the table, a *positive* (or *negative*) sign indicates an advantage or disadvantage; and a *dot* sign represents average performance.

2.4. High-performance MEMS Accelerometers

Since accelerometers have found a place for themselves in various advanced industries, the need to design and fabricate accelerometers with high-performance characteristics has grown in the past few decades. Characteristics such as high sensitivity, low noise, high dynamic range, high bandwidth, high linearity and small size were among the requirements that created an ongoing interest in this field. Consequently, many high-performance accelerometers were developed for applications in tactical grade quality, mainly for high-precision inertial navigation systems. However, a micro-machined

accelerometer that can meet these requirements in a single device is yet to be commercialized.

Table 1 Comparison between accelerometer transduction methods (+ indicates an advantage, - represents disadvantage, and • indicates average performance).

	Capacitive	Electron Tunneling	Optical	Thermal	Piezoresistive	Piezoelectric	Resonant
DC Performance	+	+	+	+	+	-	+
Total Noise	•	+	+	-	•	+	+
Interface Electronics	+	•	-	+	+	+	•
Dynamic Range	-	•	+	•	•	+	+
Fabrication	+	-	•	+	•	•	+
Packaging	+	-	-	•	+	+	-
Bandwidth	•	•	•	-	•	•	-

When designing an accelerometer, there are numerous tradeoffs to consider. One of the most critical factors determining whether an accelerometer can achieve high performance is the fabrication technology and design constraints imposed by the fabrication process. The size of the proof mass and the spring design of the accelerometer are two parameters that are heavily influenced by these fabrication limitations. These parameters are critical because the mass and spring stiffness define the resonance frequency of the accelerometer. Accelerometer cannot detect signals with a frequency higher than its resonance frequency. This means that the mechanical bandwidth of the

sensor is determined by its resonance frequency, which is, in turn, determined by its mechanical properties. Figure 2-10 depicts the effect of fabrication limitations on the mechanical bandwidth schematically.

The resonance frequency is a critical property of an accelerometer as it influences multiple parameters that define its performance. As Equation (2.3) demonstrates, the mechanical response of an accelerometer depends on its frequency, meaning that a lower resonance frequency results in a greater displacement response. Furthermore, Equation (2.5) illustrates that the resonance frequency impacts the total mechanical noise of the accelerometer, with higher frequencies resulting in more significant amounts of noise. By defining the maximum possible displacement of the accelerometer as Δy_{Max}, we can determine the maximum input acceleration possible using Equation (2.3); we have:

$$\Delta y_{Max} = \frac{a_{inMax}}{\omega_o^2} \tag{2.8}$$

We can define the dynamic range as the ratio between maximum and minimum detectable input acceleration. Thus, the resonance frequency also affects the system's dynamic range, with higher resonance frequencies resulting in a stiffer accelerometer and greater dynamic range. This is particularly important for displacement-based accelerometers as they measure the displacement. Stress-based accelerometers typically have a much higher dynamic range than displacement-based accelerometers. Figure 2-10 depicts the impact of the resonance frequency or mechanical bandwidth on other parameters schematically.

The quality factor of the accelerometer is a critical parameter that significantly impacts its performance, as evident from Equation (2.5), where it affects the mechanical noise of the system. Additionally, as seen in Figure 2-2, the mechanical response of the second-order system varies based on its quality factor. Assuming a linear and constant response of the accelerometer within its range, higher quality factors result in a lower actual mechanical bandwidth than its resonance frequency. Furthermore, the total sensitivity of the accelerometer can be defined as:

$$S_T = S_E \times S_M \times \frac{1}{\omega_o^2} \tag{2.9}$$

where $1/\omega_o^2$ corresponds to the mechanical response, and S_T represents the transduction sensitivity of the accelerometer known as scale factor. The type of transduction and MEMS design influences the sensitivity and scale factor value. The type of electronics used will also have an impact on the total output of the sensor. Finally, considering electronic noise and assuming that it is independent of mechanical noise, we can define the total noise of the system. Figure 2-10 summarizes the trade-offs involved in designing an accelerometer.

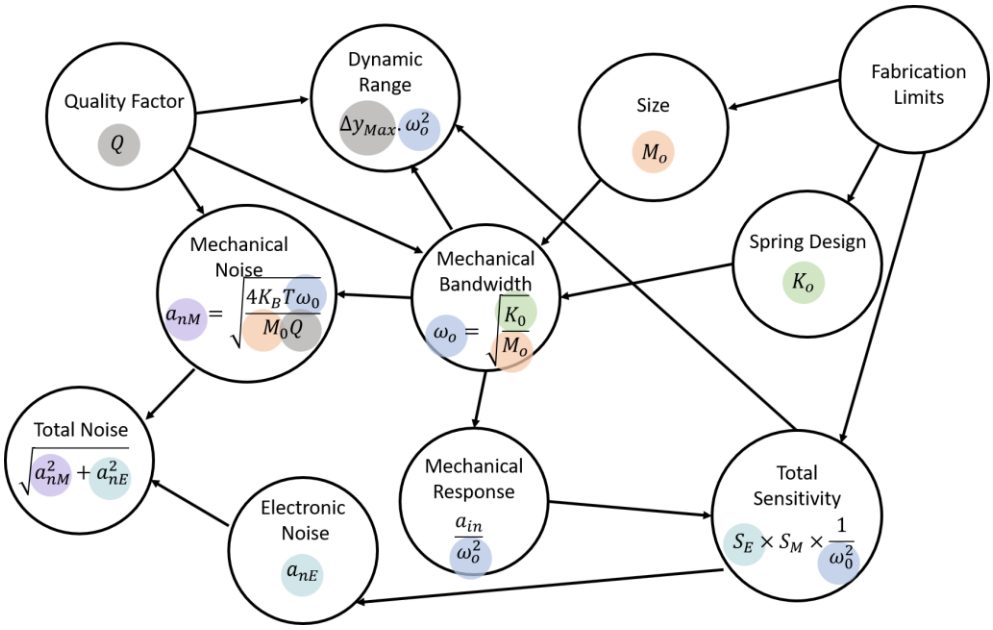

Figure 2-10 Trade-offs in accelerometer design.

In the development of high-performance accelerometers, the capability to detect even the slightest signal fluctuations is a crucial aspect. This precision becomes particularly significant in applications where granular vibration measurements are vital. A crucial metric in evaluating the performance of such accelerometers is their noise floor, and mechanical bandwidth which represents the minimum detectable signals. Therefore, a comparative analysis of noise floor and bandwidth among various high-performance

accelerometers provides valuable insights, assisting in the selection process for specific applications.

In light of the tradeoffs discussed in the previous section, there are several ways to enhance the performance of accelerometers, which numerous researchers and groups have pursued. These include:

1. Increasing the size of the proof mass or utilizing innovative fabrication method to increase M_o.
2. Reducing the resonance frequency by spring designs or innovative approaches to decrease stiffness in the structures (decreasing ω_o).
3. Increasing the quality factor through vacuum packaging or other design modifications (increasing Q).
4. Utilizing novel sensing structures to increase the scale factor of the accelerometer (increasing S_T).
5. Development of low noise and sensitive interface electronics (increasing S_E , or decreasing a_{nE})

Table 2 summarizes the reported high-performance accelerometers and their method of performance improvement.

Table 2 Summary of some of the reported high-performance accelerometers. Bandwidth is assumed to be the same as the mechanical resonant frequency of the structure.

#	type	BW Hz	Noise Floor $\frac{ng}{\sqrt{Hz}}$	Methods to reduce Minimum Detectable Signal			
				Large proof mass	Low stiffness	High Q	Structural Design
[20]	Capacitive	1000	160	✓			

(2000)							
[21] (2001)	Tunneling	1500	20	✓		✓	✓
[22]	Optical	1000	40	✓			✓
[23]	Capacitive	200	213	✓		✓	✓
[24]	Optical	36	17	✓		✓	✓
[25]	Capacitive	300	300	✓		✓	
[26]	Resonant	50	144	✓		✓	✓
[27]	Capacitive	700	200			✓	
[28]	Capacitive	28	2	✓	✓	✓	✓
[29]	Optical	-	900				✓
[30]	Optical	63000	196				✓
[31]	Capacitive	6	0.25	✓			
[32]	Resonant	-	160	✓		✓	✓
[33]	Optical	34.5	186	✓			✓
[34]	Resonant	2.7	380	✓		✓	✓
[17]	Capacitive	4500	350	✓			
[35]	Capacitive	80	10	✓			✓

[36]	Optical	100	312				✓
[37]	Capacitive	5000	216		✓	✓	
[38]	Capacitive	13	50	✓			
[39]	Optical	2.5	8	✓	✓	✓	✓
[40]	Resonant	5	17.8	✓		✓	
[41]	Capacitive	300	30	✓	✓	✓	✓
[42]	Resonant	3	680	✓		✓	✓
[43]	capacitive	158	52	✓	✓	✓	
[44]	Resonant	30	42			✓	✓
[45]	Optical	3	8	✓	✓	✓	✓
[46]	Capacitive	9	17	✓	✓	✓	
[47]	Optical	30	43				✓

In the following chapter, we will discuss the performance of the resonant accelerometers in more detail.

Chapter 3. Resonant Accelerometers

3.1. What Is Resonance?

Resonance happens when an external force oscillates in sync with an object's natural frequency, amplifying the object's vibrations. A resonant sensor (i.e. a resonant accelerometer) is a device in which the output frequency of a vibrating element changes due to the change of a physical quantity that needs to be measured. The conversion from the measured quantity to the resonance frequency of the vibrating element can be accomplished by means of a change in mass, usually in Bio and gas sensors, stress, temperature, or form of the resonator.

. One of the best ways to understand the resonant behavior of the system is to model it as a mass on the spring system, Equation (2.1). We consider that the system is excited by external sinusoidal acceleration $a_{in} = A_{in}\cos(\omega t)$. By solving the equation to find the amplitude and the phase response of the roof mass, if we assume that the response of the system is in the form of $y = A\cos(\omega t + \phi)$. We have:

$$A = \sqrt{\frac{A_{in}^2}{\left(1 - \frac{\omega^2}{\omega_0^2}\right) + \frac{1}{Q^2}\frac{\omega^2}{\omega_0^2}}} \qquad and \quad \phi = \tan^{-1}\left(-\frac{\frac{\omega}{\omega_0}}{Q\left(1 - \left(\frac{\omega}{\omega_0}\right)^2\right)}\right) \tag{3.1}$$

Figure 3-1 displays the amplitude and phase response of a driven mass-spring system. At low driving frequencies, the proof mass displacement is in-phase with external excitation, nearing zero phase shift. Conversely, at high frequencies, it's out-of-phase, nearing -180°, while at resonance frequency, the phase is precisely -90°. The amplitude at the resonance frequency can be calculated from Equation (3.1), we have:

$$A(\omega_0) = Q \times A_{in} \tag{3.2}$$

The amplitude at resonance is Q times higher than the excitation amplitude. For the case of sensing systems, this number can reach tens of thousands for micromachined resonance systems.

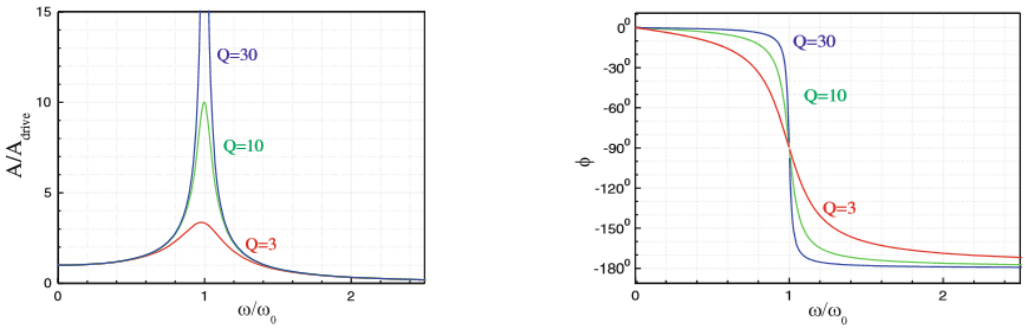

(a) (b)

Figure 3-1 (a) The amplitude and (b) the phase response of a second-order system at resonance with different quality factors.

Since we can observe amplified response while operating at resonance, this phenomenon is advantageous for micromechanical sensors. A resonant sensor comprises of a resonator that vibrates at its resonance frequency. Detection of frequency shift is advantageous due to its high dynamic range, high sensitivity, Frequency Modulated (FM) output, which is more adaptable to digital electronics.

3.2. Working Principle

In resonant accelerometers, applied acceleration leads to a change in the resonance frequency of a resonator that has been included in the accelerometer's structure. This change usually is as result of applying stress on the resonator element. Many considerations have to be put into account while designing a high performance resonant accelerometer:

- Resonator material
- Fabrication technology

- Type of resonator
- Vibration modes
- Damping and Q-factor
- Temperature stability
- Excitation and detection mechanism
- Frequency measurement methods
- Noise

MEMS resonant accelerometers usually fabricated with Silicon. Silicon has excellent mechanical properties and is widely used in IC industry, it is a candidate for the fabrication material of such accelerometers. Some of the properties that make single crystal Si an excellent material for resonant accelerometers are:

- Fabrication process maturity
- High intrinsic Q-factor
- Ease of IC integration
- High strength elastic material
- High purity with low levels of defects
- Silicon oxide properties

The structure of the vibrating element can be a cantilever (or Clamped -Free), a bridge (or Clamped-Clamped), or in most cases, a double-ended tuning fork.

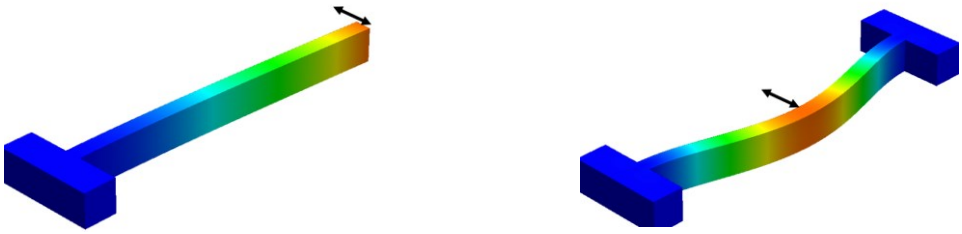

(a) (b)

Figure 3-2 Resonator structures hile vibrating (a) beam (b) bridge

We can have different mode shapes in each one of these structures in which they have their specific pattern of movement, resonance frequency and damping (Quality factor).

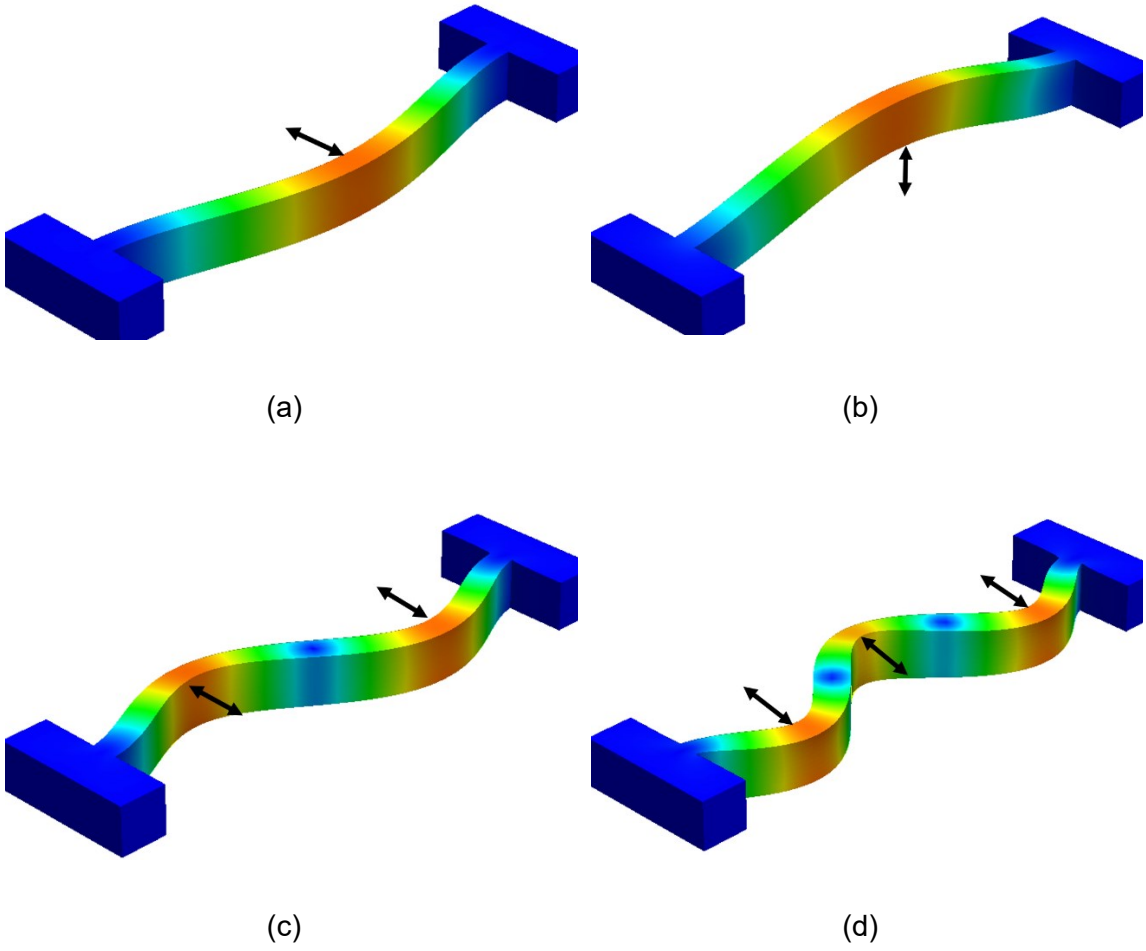

Figure 3-3 Different vibration modes of the bridge structure resonator (a) first in-plane mode (b) first out-of-plane mode (c) second in-plane mode (d) third in-plane mode.

The mechanical resonator structure has to be brought into vibration and the vibration has to be detected. A feed-back circuitry makes sure that the resonator is maintained in the desired resonance mode also when the resonance frequency is changing as a result of a change in the measured quantity. Various actuation mechanisms can be used to excite the resonator, in the same way, the vibration frequency can be sensed using different transductions such as capacitive, piezoelectric or piezoresistive. Figure 3-4 illustrates the

systematic layout of a resonant accelerometer with its mechanical design part and electronic feedback subsystem.

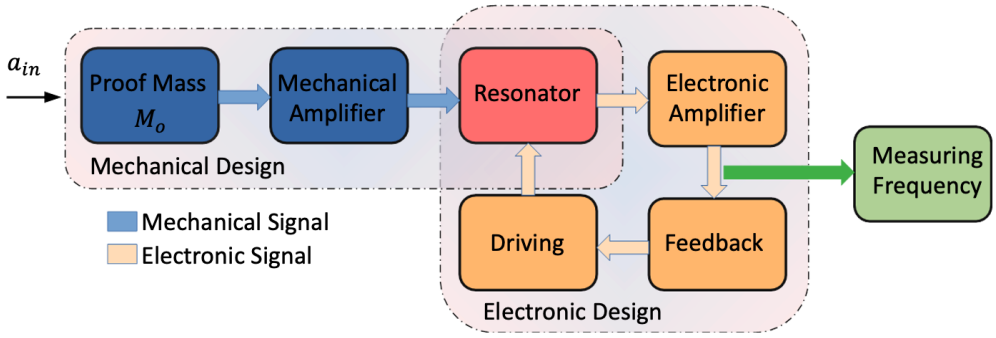

Figure 3-4 Resonant accelerometer system.

The figure below shows the silicon resonant accelerometer. When an acceleration is applied to the proof mass in the direction of sensing axis. This acceleration creates an inertial force that can be described with the well-known Newton's law:

$$F = M_0 a_{in} \tag{3.3}$$

Where M_0 is proof mass, and F is the inertial force.

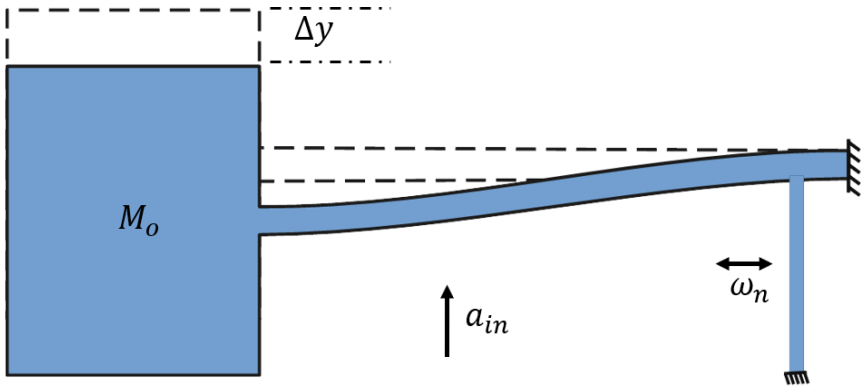

Figure 3-5 Schematic of a resonant accelerometer.

The inserted force on the proof mass creates a moment it, which results in the displacement in the direction of sensing axis; on the other side, since the displacement near the anchor is negligible, the beam experience the large amount of stress near the anchor. This stress changes the stiffness of the structure.

Assume that the natural resonant frequency of the resonant beam can be expressed as:

$$\omega_n' = \omega_n\sqrt{1+\beta a_{in}} \tag{3.4}$$

In this case, β is a constant relative to the accelerometer structure. From Taylor series:

$$\omega_n' = \omega_n\left(1+\frac{1}{2}\beta a_{in}-\frac{1}{8}\beta^2 a_{in}^2+\frac{1}{16}\beta^3 a_{in}^3+\cdots\right) \tag{3.5}$$

Therefore, by ignoring higher order terms, the frequency variation of the resonator under acceleration a_{in} is:

$$\Delta\omega = \omega_n' - \omega_n = \frac{1}{2}\beta a_{in}\,\omega_n \tag{3.6}$$

It can be seen from the Equation 3.6 in a specific acceleration input range, the measured acceleration is linearly proportional to the change in resonance frequency. Therefore, the measurement of the measured acceleration can be achieved by measuring the variation in the frequency. Based on the mechanism outlined in this chapter, numerous resonant accelerometers have been developed over the past two decades. In the following section, we will review these accelerometers and compare some of their most important properties.

3.2.1. Reported Resonant Accelerometers

The construction of a resonant accelerometers fundamentally based on three critical elements: the Resonant Beam, the Micro-lever Mechanism, and the Proof Mass. Each of these components is integral to the overall operation of the accelerometer and contributes distinctively to the device's function and performance.

Resonant beam designs have a significant impact on the sensitivity of resonant accelerometers, making them an essential part of the accelerometer's construction. The geometry of the resonant beam, including its length, width, thickness, and shape, directly affects the accelerometer's response. Moreover, the choice of material for the resonant beam also plays a crucial role. By carefully selecting the beam's geometry and shape, the

sensitivity of the accelerometer can be significantly improved. Differential sensing, which measures the difference between signals instead of absolute values, enhances device sensitivity and manages interferences. By using this method, accelerometers become more resistant to noise, improving their accuracy. Incorporating differential sensing is crucial for optimizing accelerometer performance.

Table 3 Summary of reported resonant accelerometers.

# (year)	Sensitivity $\frac{\Delta f_r}{a_{in}}$ $[\frac{Hz}{g}]$	Resonance Frequency f_r $[Hz]$	Quality Factor Q	Noise Floor $\overline{a_{in}}$ $[\frac{\mu g}{\sqrt{Hz}}]$	Size of proof mass M_0 (gram)
[48] (1990)	28	35000	-	-	65.2
[49] (1995)	200	90000	-	-	2.09 m
[50] (1995)	-	-	10000	2	-
[51] (1996)	700	400000	20000	-	0.011 m
[52] (1997)	45	68000	72000	900	-
[53] (2001)	70	400000	-	-	0.0001 m
[54] (2002)	8	6500	-	-	-
[55] (2002)	30	145,000	10000	40	0.0002 m
[56] (2003)	24.7	5,700	-	-	-
[57] (2005)	555	173000	-	-	0.418 m

[58] (2005)	35	70000	-	-	-
[59] (2005)	160	130000	-	-	-
[60] (2008)	140	130000	30000	20	-
[61] (2009)	430	50000	-	-	0.001 m
[62] (2011)	584	65000	400	-	-
[63] (2012)	496	133000			0.23 m
[64] (2012)	3.7MHz	1.9 GHz	-	-	-
[65] (2013)	82	304000	-	13.5	-
[66] (2013)	250	84000	-	-	0.00001 m
[67] (2013)	66	31400	-	-	-
[68] (2014)	14	25000	-	-	0.001 m
[26] (2014)	14.2	950	-	3.16	0.557 m
[69] (2014)	14	25000	870	-	0.00065 m
[70] (2015)	275	290000	-	-	0.0002 m
[71] (2015)	211	25000	-	-	
[72] (2015)	295	39000			0.0034 m
[73] (2015)	9600	149000	25000	0.150	0.0023

[74] (2016)	10	379000	17000	-	-
[75] (2016)	1271	26000	-	-	1.271 m
[76] (2017)	280	180000	-	1.2	-
[77] (2017)	430	803000	-	0.65	
[32] (2017)	61	550000	-	-	0.00007
[78] (2019)	120	35000	-	-	-
[79] (2019)	2802	420000	-	0.017	70 m
[42] (2019)	2752	352200	30160	0.098	72 m
[80] (2021)	4800	-	-	0.030	-

3.2.2. Existing Challenges

In recent studies on resonant accelerometers, two primary challenges have been identified. One of the most significant challenges with resonant accelerometers is their packaging. Due to the resonator's structure, these devices require vacuum packaging to achieve a higher quality factor.

The second challenge is sensitivity. Despite some resonant accelerometers having large proof mass, their sensitivity and accelerometer scale factor still need to be improved. This lack of sensitivity can be attributed to the resonant beam structures, which serve as the sensing elements in these accelerometers. These structures exhibit notably high axial stiffness. Consequently, a large force must be applied to these resonators to observe a notable change, making their sensitivity inherently low. This thesis primarily aims to

address and propose solutions for the sensitivity issue associated with resonant accelerometers.

3.3. Resonant Beam as Sensing Element

The microbeam structure is a fundamental resonant element that has found extensive application in a wide range of resonant force sensors [40], [55], [63], [81], [82], [83]. This structure consists of a microbeam, wherein one end is clamped while the other end is used to apply force. Here, we investigate the axial force's influence on the microbeam structure's resonance frequency. To analyze this effect, we employ the renowned Euler Bernoulli equations. For the analysis, we examine a simplified resonance structure depicted in Figure 3-6. In this scheme, we have a micro beam with a length denoted by "L" and a width represented by "w." The micro beam exhibits its i^{th} resonance frequency mode with the deflection equation of ϕ_i. Figure 3-6 illustrates the deflections observed in the beam for the first flexural resonance frequency. The end of the beam serves as the input axial force, while the excitation force, denoted as "P," is generated through electrostatic excitation.

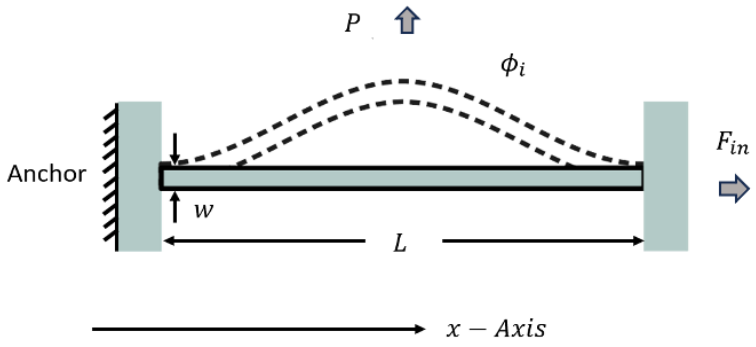

Figure 3-6 A micro-resonator beam under the axial force

From Euler–Bernoulli equation (ignoring damping) we can write:

$$\rho A \frac{\partial^2 \Phi(x,t)}{\partial t^2} + F_{in} \frac{\partial^2 \Phi(x,t)}{\partial x^2} + EI \frac{\partial^4 \Phi(x,t)}{\partial x^4} = P \tag{3.7}$$

where ρ is the density of the material, A is the cross section of the beam, E is the Young's Module of the material, I is the moment of inertia. Since the beam can be considered clamped-clamped [84], [85], we have the following boundary conditions [86]:

$$\begin{aligned} \Phi(0,t) &= \frac{\partial \Phi(0,t)}{\partial x} = 0 \\ \Phi(L,t) &= \frac{\partial \Phi(L,t)}{\partial x} = 0 \end{aligned} \tag{3.8}$$

We assume that the solution for the equation above has the following form using the technique of separation of variables:

$$\Phi(x,t) = \phi_i(x)\mathcal{T}_i(t) \tag{3.9}$$

Where $\phi_i(x)$ represents the i^{th} mode shape, a function of x alone, and indicts how the amplitude of the shape varies with time. Each solution for individual mode or superposition of the different modes are answers to the equation. By substituting the Equation 3.9 into the Equation 3.7. We have:

$$(\rho A \phi_i)\, \ddot{\mathcal{T}}_i + \left(F_{in} \frac{\partial^2 \phi_i}{\partial x^2} + EI \frac{\partial^4 \phi_i}{\partial x^4} \right) \mathcal{T}_i = 0 \tag{3.10}$$

By inserting the inner product of mode shapes from the left and using the orthogonality of these modes, we can rewrite the equation in the following form:

$$\left(\int_{x=0}^{L} (\rho A \phi_i^2)\, dx \right) \ddot{\mathcal{T}}_i + \left(\int_{x=0}^{L} F_{in} \left(\frac{\partial \phi_i}{\partial x} \right)^2 dx + \int_{x=0}^{L} EI \left(\frac{\partial^2 \phi_i}{\partial x^2} \right)^2 dx \right) \mathcal{T}_i = 0 \tag{3.11}$$

By comparing the equation with the general form of the equation for the mass-spring system. We have the relations for effective mass and spring constant as follow:

$$M_{eff} = \int_{x=0}^{L} \rho A \phi_i^2 dx \tag{3.12}$$

$$K_{eff} = \int_{x=0}^{L} F_{in} \left(\frac{\partial \phi_i}{\partial x}\right)^2 dx + \int_{x=0}^{L} EI \left(\frac{\partial^2 \phi_i}{\partial x^2}\right)^2 dx \tag{3.13}$$

In order to calculate the resonance frequency for the beams, we need to have the deflection equations for ϕ_i. We know that vibration modes are calculated from the free vibrations of the Clamped-Clamped beam [19], we have:

$$\rho A \frac{\partial^2 \Phi}{\partial t^2} + EI \frac{\partial^4 \Phi}{\partial x^4} = 0 \tag{3.14}$$

By using Equation (3.9), we have:

$$\frac{\rho A}{EI} \frac{\partial^4 \phi_i}{\partial x^4} \cdot \frac{1}{\phi_i} = -\frac{\partial^4 \mathcal{T}_i}{\partial t^4} \cdot \frac{1}{\mathcal{T}_i} \tag{3.15}$$

Since each side of the equation just depends on one variable, thus:

$$\frac{\partial^4 \phi_i}{\partial x^4} - \xi_i^4 \phi_i = 0 \tag{3.16}$$

We know from linear differential equations that solution for the Equation (3.16), vibration modes, will be in the following form:

$$\phi_i(x) = A \sin \xi x + B \sinh \xi x + C \cos \xi x + D \cosh \xi x \tag{3.17}$$

With the boundary conditions presented in Equation (3.8), We have the equation of deflection for the Clamped-Clamped beam, denoted as ϕ_{iCC}:

$$\phi_{icc}(x) = C\left(-\cos\xi_i x + \cosh\xi_i x - \left(\frac{\sin\xi_i L + \sinh\xi_i L}{-\cos\xi_i L + \cosh\xi_i L}\right)(-\sin\xi_i x + \sinh\xi_i x)\right) \tag{3.18}$$

where ξ_i is the eigen value calculated from eigen value solutions, and can be calculated for the first four modes as follows:

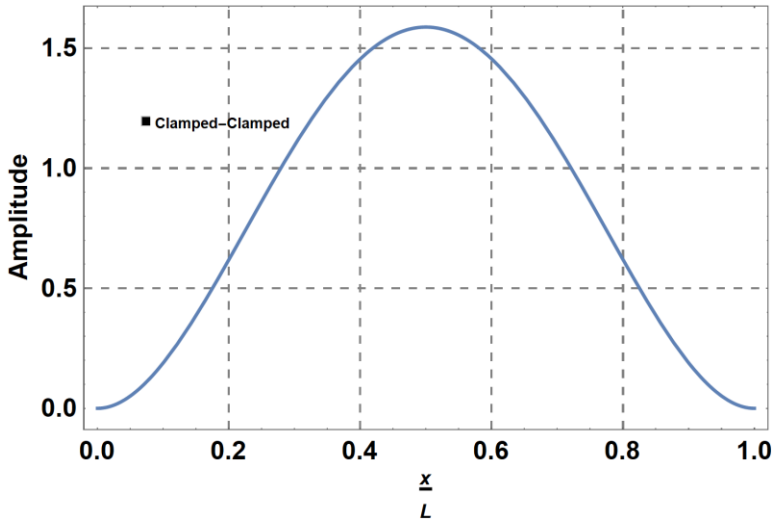

Figure 3-7 The deflection shape of the first resonance mode for a clamped-clamped beam solved for unity energy.

$$\xi_{1,2,3} = 4.72122 \quad , 7.85359 \quad , 10.9956 \tag{3.19}$$

Letting C to be calculated for the unity energy solutions we can plot the normalized first mode shape of a Clamped-Clamped beam. Figure 3-7 shows the deflection shape of the first resonance mode.

By solving the deflection equations, we can find the values for the integrals presented in Equation (3.12) and (3.13), and the resonance frequency in the presence of axial force:

$$f_{0cc} = \frac{1}{2\pi}\sqrt{\frac{198\frac{EI}{L^2} + 4.837\ F_{in}}{0.398\ M_0 L}} \tag{3.20}$$

Where $M_0 = \rho h w L$, h is the thickness of the structure. We can plot the resonance frequency versus applied axial force as shown in Figure 3-8.

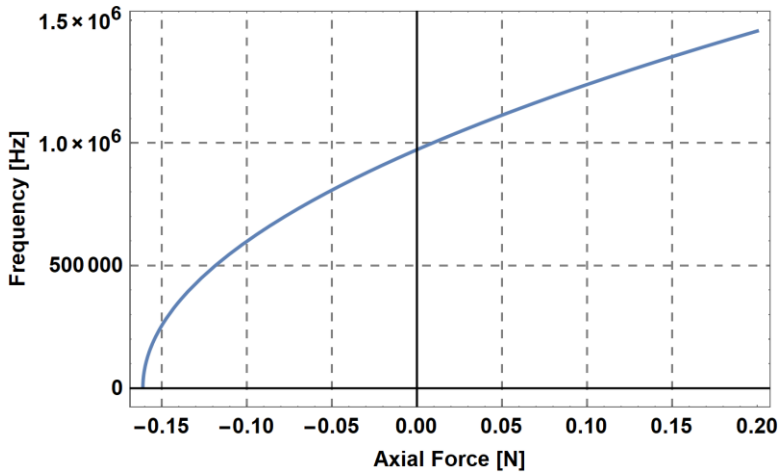

Figure 3-8 Change in resonance frequency versus axial force for a Silicon resonator designed around 1MHz (L=300μm, w=10μm, h=25μm). The positive values indicate the tensile force, while the negative values indicate the compressive force.

Figure 3-8 illustrates the fundamental principle underlying the operation of resonant force sensors. It presents the relationship between the resonance frequency and the applied axial force. As the absolute value of the compressive applied force increases, the resonance frequency decreases. This decrease is a direct consequence of our understanding that applying compressive force to the resonant beam reduces its resonance frequency. This decrease continues as the axial force progressively increases until it reaches the critical buckling region. The force required to buckle the beams is typically high. Considering the magnitude of the forces that we usually work with within MEMS resonant accelerometers, it is improbable that the beams would breach the buckling force threshold. Conversely, when applying force in the opposite direction, namely tensile force, the resonance frequency of the beam increases.

Furthermore, it is evident from Figure 3-8 that the sensitivity of the sensors, or the rate of change in resonance frequency to the axial force, does not exhibit a perfectly linear relationship. Instead, the sensor's sensitivity varies nonlinearly as a function of the applied force. However, this nonlinearity is typically observed at higher force magnitudes. In contrast, for smaller-scale forces, particularly within the MEMS structures, it can be reasonably approximated that the relationship between the changing resonance frequency and the applied force follows a linear function. In the subsequent subsections, we will analyze the factors that influence the sensitivity of resonant beam sensors.

3.3.1. Effect of Beam Dimensions on Sensitivity

Numerous studies have been undertaken focusing on the calculation and optimization of the resonant force sensors dimensions. The aim of these studies is to optimize the sensitivity of these resonant sensors [87], [88], [89]. The dimensions of a resonant beam are key parameters influencing the performance of these sensors, and hence, require meticulous optimization to enhance their effectiveness. To examine the impact of length on the sensitivity of the resonant beam, we expand the equation presented in the previous section. By incorporating all the relevant variables within the equation, we gain an understanding of the factors that influence sensitivity. This expanded equation allows for a detailed analysis, specifically highlighting the effect of the resonant beam's length on sensitivity. We have:

$$f_{0CC} = \frac{1}{2\pi}\sqrt{\frac{198\frac{EI}{L^2} + 4.837\ F_{in}}{0.398\ M_0 L}} = \frac{1}{2\pi}\sqrt{\frac{198\frac{E}{L^2}(\frac{hw^3}{12}) + 4.837\ F_{in}}{0.398 \times \rho hwL \times L}} \tag{3.21}$$

The equation for sensitivity can be derived by taking the derivative of the function with respect to the applied axial force. We have:

$$S_{F_{in}}^{f_{0CC}} = \frac{\partial f_{0CC}}{\partial F_{in}} = \frac{0.610}{\sqrt{M_0 \frac{4.837 F_{in} L^2 + 16.5 E h w^3}{L}}} \tag{3.22}$$

Ignoring high-order terms, the sensitivity of the resonance frequencies of the beams to axial force (for small forces around $F_{in} = 0$) is estimated from the Equation (3.22):

$$S_{F_{in}}^{f_{0CC}} = \frac{\partial f_{0CC}}{\partial F_{in}} \approx \frac{0.150 \sqrt{\frac{E}{\rho}}}{E h w^2} \tag{3.23}$$

As observed from the Equation 3.23, the sensitivity of the resonance beams with respect to the axial force is independent of the length of the resonant beams.

Another important factor to take into account during the design of a resonant sensor relates to the difficulty of measuring small changes in resonance at high frequencies. For instance, measuring a $10\,Hz$ shift in resonance frequency when the resonance frequency is $1\,GHz$, $10\,ppb$, presents a different set of challenges in comparison to identifying a $10\,Hz$ change in resonance frequency when the resonance frequency is at $1\,kHz$, $10000\,ppm$. As a result, one crucial performance criterion that we must take into consideration is the normalization of the change in resonance frequencies relative to the unloaded resonance frequency. By doing so, we can formulate the following equation:

$$\frac{\frac{\partial f_{0CC}}{\partial F_{in}}}{f_{0CC}} = \frac{0.0122 L^2}{E\left(\frac{h w^3}{12}\right)} = \frac{0.0122 L^2}{EI} \tag{3.24}$$

As Equation 3.23 illustrates, the length of the beam doesn't affect the absolute sensitivity of the resonator. However, a longer beam length proves advantageous when it comes to relative sensitivity (Equation 3.24). This implies that with an increased length,

we are able to lower the resonance frequency without affecting the sensitivity. Hence, we can measure the same shift in the resonance frequency for a given axial force, but at lower resonance frequencies. This is an advantage in terms of measurement accuracy.

It is evident that the beam's width substantially impacts the sensitivity of the resonant structure. This impact is proportional to the width's square; consequently, as the beam's width diminishes, the structure's sensitivity escalates significantly. In terms of relative sensitivity , we can once again derive the equation for relative sensitivity in relation to the unloaded resonance frequency. This derived equation reveals that by reducing the beam's width, the structure's relative sensitivity notably enhances. For these resonant structures, narrowing the beam width is the primary strategy to boost the sensitivity.

$$\frac{\frac{\partial f_{0CC}}{\partial F_{in}}}{f_{0CC}} = \frac{0.1464L^2}{Ehw^3} \tag{3.25}$$

3.3.2. Effect of Vibration Modes on Sensitivity

Previous studies have indicated that higher vibration modes yield greater sensitivity to axial force [90]. In this section, we intend to thoroughly examine its impact. Next-generation MEMS resonators are anticipated to operate iat high-frequency to meet the escalating demands of numerous applications. However, it remains challenging to actuate and modulate conventional resonators at multiple higher modes using parallel-plate electrodes or comb-drive electrodes, standard Double-Ended Tuning Fork (DETF) resonators, being electrostatically actuated, only vibrate at lower modes [91]. Nevertheless, resonators that offer higher modes have gained considerable interest. Reports have documented higher-order vibration of ring resonators [92], along with the employment of support beams situated at several flexural-mode node points for beam resonators [93], [94], [95], [96]. This technique allows for higher-order vibrations, but the resonator is limited to a specific mode and lacks tunability. By introducing driving

electrodes at appropriate locations, it is possible to drive the first and third modes. However, the resonator is still unable to vibrate at higher modes [97]. Fishbone-shaped clamped-clamped beam resonators have been demonstrated to facilitate frequency tuning and mode selection functions for a broader range of modes. By manipulating the electrode configuration, the resonator can vibrate at the first five resonant modes [91], [98], [99].

Referencing back to the formulations presented in Equations (3.9) and (3.10), we can observe that these equations are valid for all mode shapes, encompassing any deflections that the resonators might adopt. Our approach is to solve the equations identifying the mode shape for the second resonant mode. Following this, we calculate the resonance frequency and the sensitivity to the axial force, while the resonator operates at higher resonance frequency. From Equation (3.19), we can use the eigen value for the second mode and substitute that in Equation (3.18). We have:

$$\phi_{2CC}(x) = C\left(-\cos\xi_2 x + \cosh\xi_2 x - \left(\frac{\sin\xi_2 L + \sinh\xi_2 L}{-\cos\xi_2 L + \cosh\xi_2 L}\right)(-\sin\xi_2 x + \sinh\xi_2 x)\right);\ \xi_2 = 7.85359 \tag{3.26}$$

Letting C be calculated for the unity energy solutions we can plot the second mode shape of a Clamped-Clamped beam for the normalized length. Figure 3-9 shows the deflection shape of the second resonance mode.

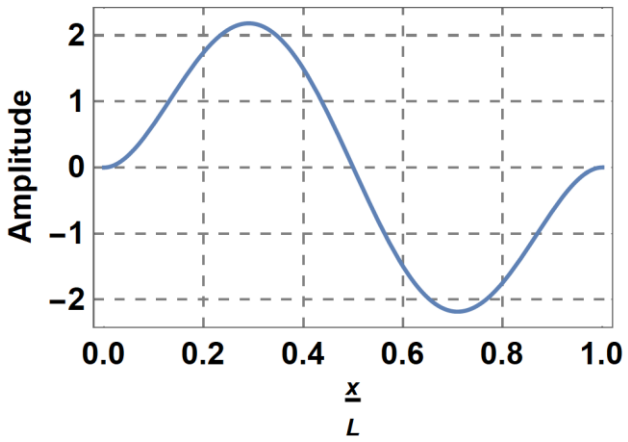

Figure 3-9 Deflection shape of the second resonance mode in a Clamped-Clamped resonator

By finding the deflection equation, we can find the values for the integrals presented in Equation (3.8) and (3.9), and the resonance frequency with the presence of axial force:

$$f_{0CC2} = \frac{1}{2\pi}\sqrt{\frac{1822.29\frac{EI}{L^2} + 22.061\,F_{in}}{0.478\,M_0 L}} \tag{3.27}$$

Ignoring high-order terms, the sensitivity of the second resonance frequency of the beams to axial force (for small forces around $F_{in} = 0$) is estimated from the Equation (3.27):

$$S_{F_{in}}^{f_{0CC2}} = \frac{\partial f_{0CC2}}{\partial F_{in}} \approx \frac{0.206\sqrt{\frac{E}{\rho}}}{Ehw^2} \tag{3.28}$$

After a comparative analysis of the equations illustrating the sensitivity of the resonance beam at the two frequencies - denoted as the first and second resonance frequencies in Equations 3.25 and 3.29, respectively - it is evident that operating at the second (higher resonance frequency) tends to yield a greater sensitivity towards axial force. This implies that increasing the operational frequency to a second for a beam with same dimensions, could enhance the system's sensitivity to the axial force.

Similar to our previous analysis concerning the first resonance frequency and its associated relative sensitivity, we can extend the same analysis to the second resonance frequency. Correspondingly, we can calculate an equation relevant to the second resonance frequency. For a comprehensive comparison and to maintain continuity in our investigation, we will also revisit the equations related to the first resonance frequency. By doing this, we aim to present a comparative study between the first and second resonance frequencies, thereby enlightening our understanding of the impact each frequency has on the system's sensitivity.

$$\frac{\frac{\partial f_{0CC1}}{\partial F_{in}}}{f_{0CC1}} = \frac{0.0122L^2}{EI} \tag{3.29}$$

$$\frac{\frac{\partial f_{0CC2}}{\partial F_{in}}}{f_{0CC2}} = \frac{0.0060L^2}{EI} \tag{3.30}$$

Through an examination of the Equations (3.233) and (3.28)-(3.30), we note that the absolute sensitivity of a resonator operating in the second mode, assuming identical dimensions, is significantly greater than the sensitivity observed in the first mode. However, it's crucial to address the relative sensitivity, or in other words, the sensitivity normalized to unloaded resonance frequency. For the second resonance mode, this relative sensitivity is much lower than that in the first resonance mode. This differential aspect leads to a crucial trade-off in the design of resonant sensors, further emphasizing the importance of such considerations in the system's design process.

For instance, if we aim to design a resonant sensor that requires the resonance frequency of the sensing element to be at a certain frequency - let's assume, $1MHz$ - it might be more beneficial to design the system to operate at a higher resonance frequency, such as in the second mode. The rationale here is that the shift in resonance due to axial force at $1MHz$ for the second mode exceeds that of the first mode at $1MHz$.

However, in the design of a specific sensing element, design a resonant sensor that requires the sensing element has a certain dimension, it's critical to note that although moving to a higher frequency increases sensitivity, the elevation in the resonance frequency for the second mode is so substantial that it results in a dramatic reduction in relative sensitivity. This shift can complicate the measurement process, both from an electronic and measurement perspective.

Chapter 4. Modified Beam Structures for Improved Sensitivity

4.1. Beam Boundary Conditions and Sensitivity

For most resonant sensors, changes in the natural frequency are caused by fluctuations in the system's effective stiffness. Consequently, resonant force sensors are key elements in the design and operation of the majority of resonant sensors [55], [81], [82]. In these force sensors, the central sensing component usually takes the form of a mechanical resonator such as a beam or a membrane. The most basic resonant component is a microbeam, anchored at one end to a fixed reference, and at the other end to the mechanism applying force to it [73], [84], [87], [100]. A significant drawback in the evolution of resonant beam sensors is their high axial stiffness, which diminishes their sensitivity.

This section introduces a strategy for enhancing sensitivity by modifying the beam's boundary conditions. We demonstrate that the sensitivity of these sensors can be significantly improved by implementing Pinned-Pinned or Free-Free boundary conditions, among others. The suggested approach for enhancing the sensitivity of resonant sensors involves altering the beam's boundary conditions, which subsequently affects ϕ_i. Nonetheless, adding axial force complicates Equation (3.7) solutions, potentially making a straightforward, closed-form expression for ϕ_i unattainable. Given that minor axial forces do not substantially modify the beam's geometry, the modal forms of the unloaded beam can serve as approximate models for beams under axial load, as shown in Equation (3.7). As a result, we consider that vibration modes will be in the form of Equation (3.17) where A, B, C, and D are determined by applying appropriate boundary conditions and solving the equations for unity energy. We consider the classic boundary conditions for Clamped-Clamped (CC), Pinned-Pinned (PP), and Free-Free (FF) beams as they are presented in Table 4 [101]. The dynamic behavior of a beam is significantly influenced by the choice of boundary conditions. Three commonly used boundary conditions for slender beams are

Clamped-Clamped (C-C), Free-Free (F-F), and Pinned-Pinned (P-P). In a C-C configuration, both ends of the beam are fixed, preventing rotation and displacement. In contrast, F-F boundary conditions allow the beam ends to freely move and rotate. Meanwhile, a P-P boundary condition dictates that while the beam ends cannot displace, they are able to rotate.

Table 4 Summary of boundary conditions for Clamped-Clamped (CC), Pinned-Pinned (PP), and Free-Free (FF) beams.

Clamped-Clamped (CC)	$\Phi(0,t) = \frac{\partial \Phi(0,t)}{\partial x} = 0$ $\Phi(L,t) = \frac{\partial \Phi(L,t)}{\partial x} = 0$
Pinned-Pinned (PP)	$\Phi(0,t) = \frac{\partial^2 \Phi(0,t)}{\partial x^2} = 0$ $\Phi(L,t) = \frac{\partial^2 \Phi(L,t)}{\partial x^2} = 0$
Free-Free (FF)	$\frac{\partial^2 \Phi(0,t)}{\partial x^2} = \frac{\partial^3 \Phi(0,t)}{\partial x^3} = 0$ $\frac{\partial^2 \Phi(L,t)}{\partial x^2} = \frac{\partial^3 \Phi(L,t)}{\partial x^3} = 0$

The equations for different types of beams can be obtained by solving equation (3.9) with the boundary conditions provided above. These equations are presented below:

$$\phi_{0CC}(x) = C_{CC}\left(\cosh \xi_i x - \cos \xi_i x - \left(\frac{\sin \xi_i L + \sinh \xi_i L}{-\cos \xi_i L + \cosh \xi_i L}\right)(\sinh \xi_i x - \sin \xi_i x)\right) \quad (4.1)$$

$$\phi_{0PP}(x) = C_{PP}(\sin \xi_i x) \quad (4.2)$$

$$\phi_{0FF}(x) = C_{FF}\left(\cos\xi_i x + \cosh\xi_i x - \left(\frac{\cos\xi_i L - \cosh\xi_i L}{\sin\xi_i L - \sinh\xi_i L}\right)(\sin\xi_i x + \sinh\xi_i x)\right) \qquad (4.3)$$

The amplitudes C_{CC}, C_{PP}, and C_{FF} represent the amplitude of vibrations that depends on excitation signal amplitude. It is important to note that these amplitudes do not impact the final resonance frequency of the system. Additionally, the variable ξ_i can be determined from the solution of the eigenvalue problem. The table below presents the corresponding values for these solutions of each beam for the first three modal shapes.

Table 5 Summary of the values for ξ for the first three vibration modes

C-C	$\xi_{1,2,3} = 4.72122 \quad , 7.85359 \quad , 10.9956$
P-P	$\xi_{1,2,3} = \pi \quad , 2\pi \quad , 3\pi$
F-F	$\xi_{1,2,3} = 4.72122 \quad , 7.85359 \quad , 10.9956$

Letting C_{CC}, C_{PP}, and C_{FF} to be calculated for the unity energy solutions we can plot the normalized first mode shape of a Clamped-Clamped (CC), Pinned-Pinned (PP), and Free-Free (FF) beam. Figure 4-1 shows the deflection shape of the first resonance mode.

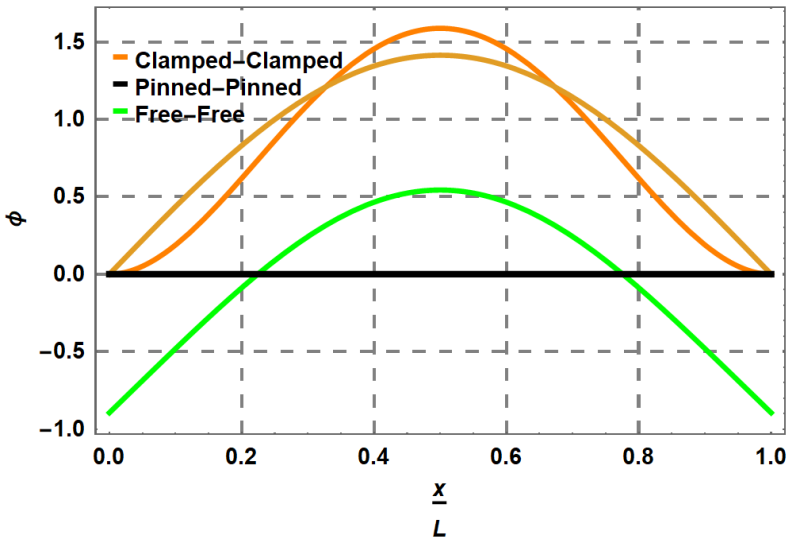

Figure 4-1 Defection shapes of the first resonant mode for three beams with different boundary conditions.

Subsequent to the above analysis, these deflection equations are then integrated into Equations (3.8) and (3.9), thereby enabling us to calculate the relation between the resonance frequency and the applied axial force for each respective beam type. This computation aids us in understanding the behavior of the beams under varying conditions. Equations below, like the equation that was presented earlier in chapter 3 for C-C beam, present the resonance frequency of the beams in the presence of an axial force:

$$f_{CC} = \frac{1}{2\pi}\sqrt{\frac{198\frac{EI}{L^2} + 4.837\ F_{in}}{0.398\ M_0 L}} \tag{4.4}$$

$$f_{PP} = \frac{1}{2\pi}\sqrt{\frac{48.6\ \frac{EI}{L^2} + 4.938\ F_{in}}{0.5\ M_0 L}} \tag{4.5}$$

$$f_{FF} = \frac{1}{2\pi}\sqrt{\frac{50\ \frac{EI}{L^2} + 4.948\ F_{in}}{0.1\ M_0 L}} \tag{4.6}$$

where M_0 is the static mass of the beam (i.e., $M_0 = \rho whL$). Ignoring high-order terms, the sensitivity of the resonance frequencies of the beams to axial force normalized to unloaded resonance frequencies, f_{0CC}, f_{0PP}, and f_{0FF}, respectively, are estimated from:

$$S_{F_{in}}^{f_{CC}} = \frac{1}{f_{CC0}} \frac{\partial f_{CC}}{\partial F_{in}} \approx 0.0122 \frac{L^2}{EI} \tag{4.7}$$

$$S_{F_{in}}^{f_{PP}} = \frac{1}{f_{PP0}} \frac{\partial f_{PP}}{\partial F_{in}} \approx 0.0508 \frac{L^2}{EI} \tag{4.8}$$

$$S_{F_{in}}^{f_{FF}} = \frac{1}{f_{FF0}} \frac{\partial f_{FF}}{\partial F_{in}} \approx 0.0495 \frac{L^2}{EI} \tag{4.9}$$

It is evident from the equation presented above that the sensitivity of the Pinned-Pinned and Free-Free beam surpasses that of the clamped-clamped, exhibiting an potential increase of nearly fourfold in sensitivity. Thus, we will employ this concept to enhance the sensitivity of resonance sensors. In the subsequent section, we will introduce modified beam structures to improve sensitivity by adjusting their boundary conditions.

4.2. Modified Beam Design

To facilitate a comparison of resonators with different boundary conditions, a C-C beam design with a length of L and a width of w is depicted in Figure 4-2(a) as a reference. Due to the limitations of microfabrication techniques, achieving true boundary conditions is not feasible. In Figure 4-2(b), an approximation is demonstrated to realize P-P boundary conditions at the beam ends. This involves adding two flexible beams at angles to both ends of the main beam, which fixes the location of the beam ends while allowing for some flexibility in rotation. By employing boundary beams with sufficient flexibility, the resonant patterns of the main beam approach those of a P-P beam.

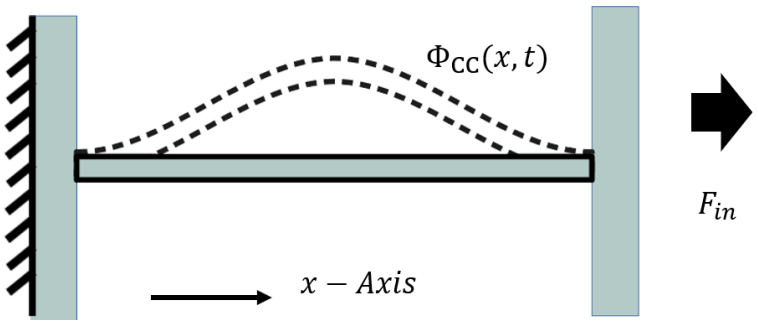

(a)

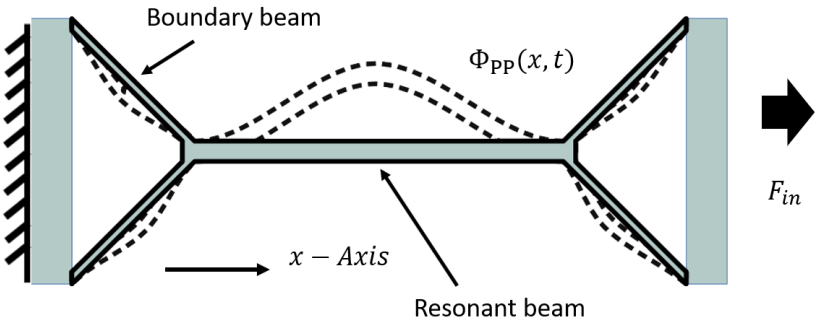

(b)

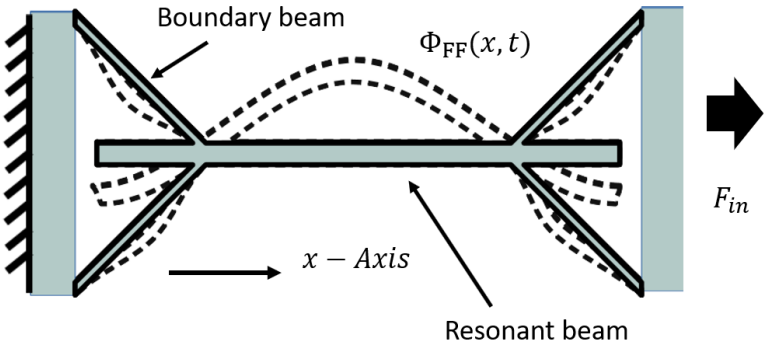

(c)

Figure 4-2 Schematic of (a) Clamped-Clamped (C-C), (b) Pinned-Pinned (P-P), (c) Free-Free (F-F), and their defection shape in the first vibration mode.

Figure 4-2(c) showcases the design of an F-F beam. In this configuration, the main beam is connected to the boundary beams at points where deflection during vibration approaches zero. The purpose of this method is to minimize the impact of the microbeams on the vibrational mode of the F-F frame without compromising the sensitivity of the samples. By attaching two boundary beams at 45-degree angles to the resonant beam, a vibrational mode resembling an ideal F-F beam is achieved. Similar to the P-P configuration, as the widths of the boundary beams decrease, the vibrational modes of the resonant beam progressively resemble an ideal F-F beam. In the Figure 4-2, the approximate schematic of the first vibration is shown with $\Phi(x,t)$ with CC, PP, and FF indexes for Clamped-Clamped, Pinned-Pinned and Free-Free.

4.3. Simulations

The behavior of device structures was analyzed through Finite Element Analysis (FEA) using CoventorWare software [102]. This simulation aimed to investigate the deviations from idealized theoretical models. The material properties and layer dimensions employed in the analysis were based on the specifications provided for the SOI-MuMPS process, which were subsequently used for fabricating the samples. We proceed with the model analysis which allows us to determine the natural resonance frequency of the devices, both with or without axial force.

To ensure coherence among the frequencies, particularly for the free-free beam type 2, we explore adjustments in the length of the devices. By fine-tuning the length, we aim to align the frequencies within a desired range. Ultimately, we obtain four distinct designs each with its unique characteristics and considerations. Figure 4-3(a) illustrates the clamped-clamped beam, while Figure 4-3(b) showcases a painted beam. In Figure 4-3(d), we observe a free-free beam, where the boundary beam is narrower than that in Figure 4-3(c).

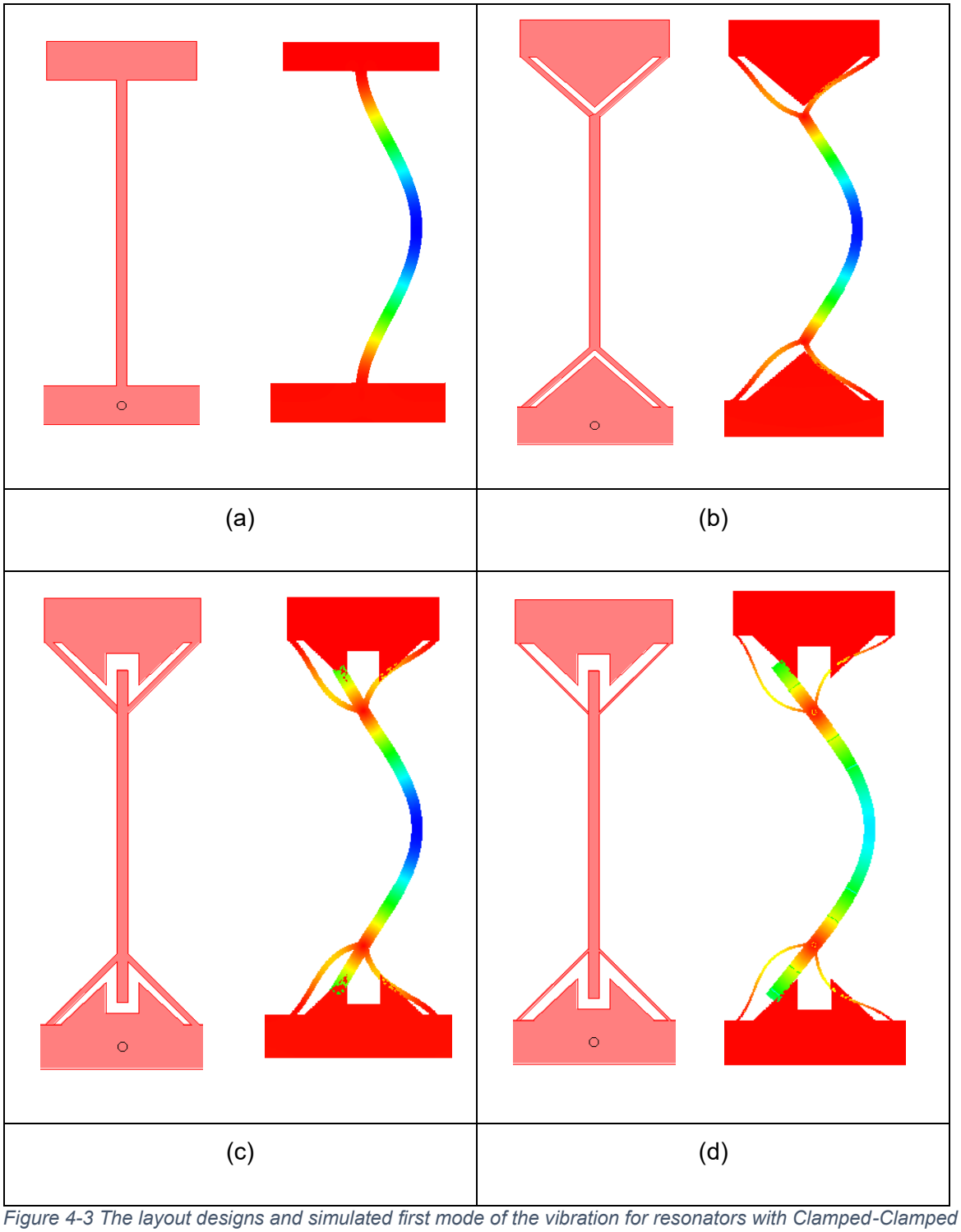

Figure 4-3 The layout designs and simulated first mode of the vibration for resonators with Clamped-Clamped (a), Pinned-Pinned (b), Free-Free (c), Free-Free with narrower Boundary beam (d). Resonator mode deflections are shown with 50-time exaggeration.

By comparing the deflections of C-C and P-P beams, we notice that the addition of two boundary beams alters the slope of deflection at the beam's ends. In other words, the slope of deflection at the P-P beam is nonzero. Figure 4-4 shows this difference in deflection visually. Consequently, the beam is no longer devoid of deflection and exhibits slight rotation at both ends. This deviation indicates that the beam is closer to a pinned-pinned boundary condition, although we must emphasize that it is not ideal. Our objective is to bring the beams as close as possible to the ideal beams of deflection.

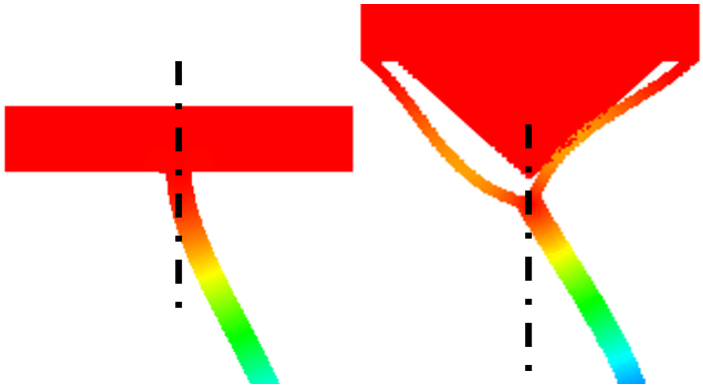

Figure 4-4 the comparison between deflections of the C-C and P-P beams at the ends of the beams.

Moreover, by comparing Figures 4-3(c) and 4-3(d), we can observe that narrowing the boundary beam allows for greater deflection, bringing the beam closer to a free-free boundary condition. Table 5 provides the summary for the dimensions of the beams simulated.

By referring to the dimensions provided in Table 5, we can calculate the theoretical values for the resonance frequency, as well as the shift in resonance frequency for an applied force. For this analysis, we consider an applied force of $35\mu N$, which roughly results in about 100 Hz shift in resonance of the Clamped-Clamped beam as a base of our comparison. We apply these calculations to all the beams depicted in Figure 4-3. Notably, the formulas for beams shown in Figures 4-3(c) and 4-3(d) remain the same.

Table 5 Summary of the design dimensions

Beam type	Resonant Beam $[\mu m]$	Boundary Beam $[\mu m]$
Clamped-Clamped (Figure 4-3(a))	Length=310 Width=10	NA
Pinned-Pinned (Figure 4-3(b))	Length=245 Width=10	Length=91 Width=10
Free-Free (1) (Figure 4-3(c))	Length=300 Width=10	Length=91 Width=5
Free-Free (1) (Figure 4-3(d))	Length=300 Width=10	Length=91 Width=2

Subsequently, we employ a numerical simulation to determine the shift in resonance frequency resulting from the application of axial force to all the beams. The obtained results are summarized in Table 6, which provides an overview of the performance of these beams. It includes the resonance frequency and the corresponding shift in resonance frequency when subjected to an applied force of $35\mu N$.

Table 6 Summary and comparison of theoretical and simulation performances of the beams

Beam type	Unloaded resonance frequency (Hz)		Resonance-shift due to $35\mu N$ force (Hz)	
	Theory	Simulation	Theory	Simulation
Clamped-Clamped	910843	829749	105	97
Pinned-Pinned	629080	842054	194	175
Free-Free (1)	975421	1056970	428	180
Free-Free (2)	975421	847003	428	357

A noticeable distinction arises between the theoretical and numerical models when examining the impact of non-ideal boundary conditions. Specifically, in the case of the clamped-clamped (C-C) beam, the numerically calculated resonant frequency is lower due to the softer connections between the beam and the anchors, deviating from the resonance frequency estimated under ideal clamped boundary assumptions. Conversely, for the free-free (F-F) and pinned-pinned (P-P) beams, the numerical resonance frequencies surpass the theoretical values due to the increased stiffness resulting from the realistic boundaries employed.

It should be highlighted that the sensitivity of F-F beams is highly dependent on the geometry and position of the boundary beams. This can cause noticeable variations in the responses of different devices. However, the results from both numerical and experimental analyses, which will be discussed in the following section, show good agreement.

One important factor to consider when designing sensors is the angle of the boundary beams. This angle refers to the orientation between the boundary beam and the resonance beam at their connection point. It is important to note that reducing the angle decreases sensitivity. This is because, as the angle approaches zero, the beam becomes more like a clamped beam, which has lower sensitivity. On the other hand, increasing the angle, for example from 45 degrees to 90 degrees, also decreases sensitivity. This is because most of the force applied to the boundary beam results in deflection in the boundary beams rather than introducing stress to the resonant beam. For the devices in this thesis, we used an angle of 45 degrees for the developed devices.

To further improve the sensitivity of the sensors, additional modeling and experimentation are needed. The results presented here serve as a proof of concept, showing that devices at a 45-degree angle demonstrate nearly four times the sensitivity compared to the transition from a clamped-clamped beam to a pinned-pinned beam.

However, to achieve maximum performance enhancements, a comprehensive system-level simulation is needed, which will be explored in future work.

To validate our simulation findings, we fabricated and tested a set of devices based on our theory. The following sections will discuss the fabrication process and the experimental results obtained from the devices.

4.4. Fabrication

To validate the design principles, a set of sample devices was designed and fabricated utilizing the SOI-MuMPS (Silicon-On-Insulator - Multi-User MEMS Processes) process [103]. This fabrication technology allows for a minimum width and gap resolution of 2μm for the micromechanical structures. The structural layer is a single crystal Silicon layer with thickness of 25μm. The release of the devices is achieved through a backside etching process of the handle wafer. A mask was prepared for the fabrication process, consisting of three layers. The first layer comprises a silicon structure that will be etched in the second layer to form contacts. The third layer is utilized for the backside etching process, which creates the release structure. The image of the mask can be seen in Figure 4-5 (a). Figure 4-5(b) presents a more detailed view of the design for Pinned-Pinned beams, as an example, including the electrode configurations. The electrode configuration remains broadly consistent across all the devices. As depicted in Figure 4-5(b), two electrodes are positioned on the resonant beam's left and right sides. The resonant beam itself is situated at the center. These electrodes serve the purpose of exciting the resonator at its resonance frequency. Additionally, there is an electrode located at the bottom, directly connected to the resonant beam, which is used to apply a DC voltage; this electrode is denoted by the letter "R". The excitation and sensing electrodes are represented by "E1" and "E2" respectively.

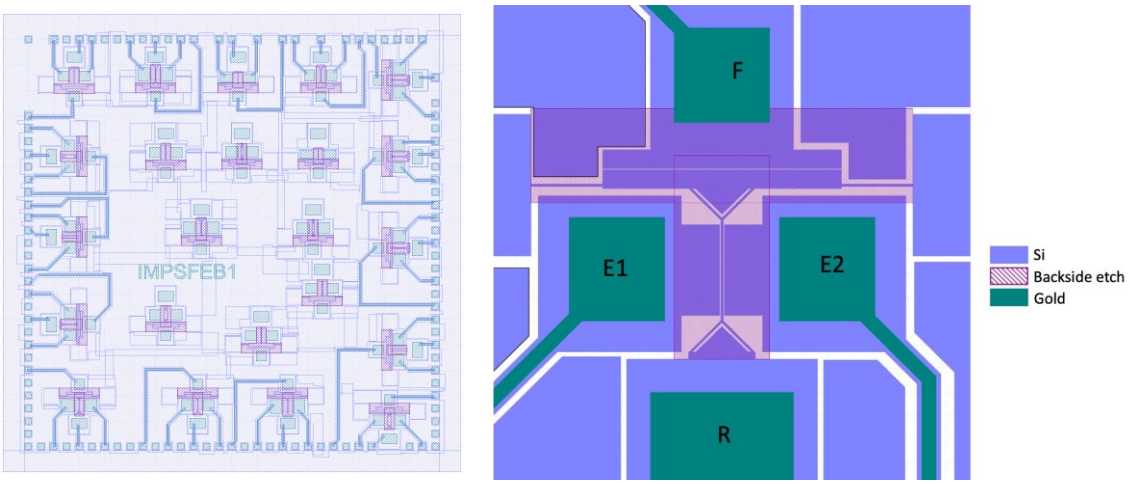

(a) (b)

Figure 4-5 (a) Designed mask for fabrication (b) The design for Pinned-Pinned beam with electrode configuration.

Furthermore, an additional electrode is positioned at the top of the design to apply electrostatic force on the resonator. This electrode remains consistent across all the devices to ensure the same voltage difference and, subsequently, the same force is applied to all the devices. In the figure, this electrode is identified by the letter "F".

The PiezoMUMPs procedure is a modified version of a 5-mask level SOI patterning and etching method developed by MEMSCAP [102]. This process improvement aims to incorporate more features into the existing SOIMUMPs protocol. Below, we provide a brief overview of this micromachining process.

The process begins with 150mm n-type double-sided polished Silicon-On-Insulator wafers. After doping the top surface of the Silicon layer, a phosphosilicate glass (PSG) layer is deposited and then annealed at 1050°C for an hour in an Argon atmosphere. Next, the PSG layer is removed through wet chemical etching, and a $200\ nm$ thermal oxide is grown. After patterning, the region defined by the PADOXIDE mask is left behind after post-reactive ion etching. The silicon layer is then patterned with the SOI mask and

subjected to a Deep RIE etch using Inductively Coupled Plasma technology. A protective material is applied to the top surface of the silicon layer. After flipping the wafers, the Substrate layer is patterned from the underside using the TRENCH mask. An etching process is then carried out using Reactive Ion Etching, followed by etching of features throughout the Substrate layer. SEMs of the fabricated samples are shown in Figure 4-6 to 4-8.

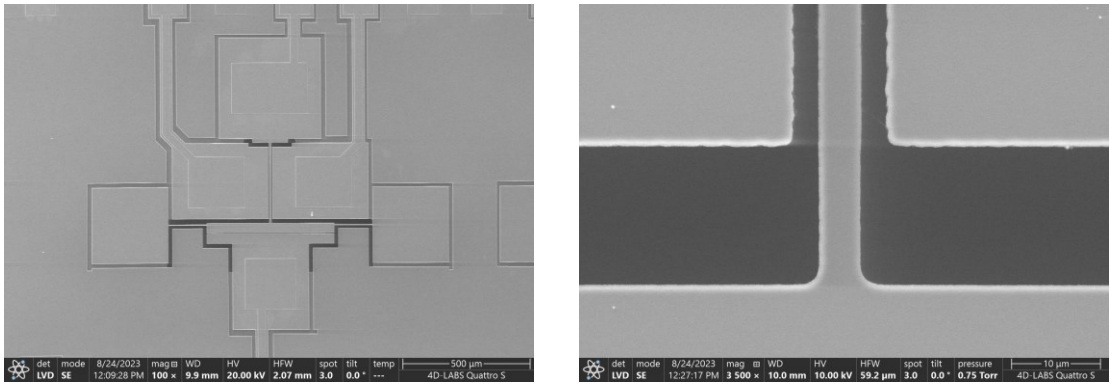

(a) (b)

Figure 4-6 SEM images of the fabricated C-C beam (a) with depiction of electrode configuration (b) the point where beam connected to the anchor as clamped boundary condition

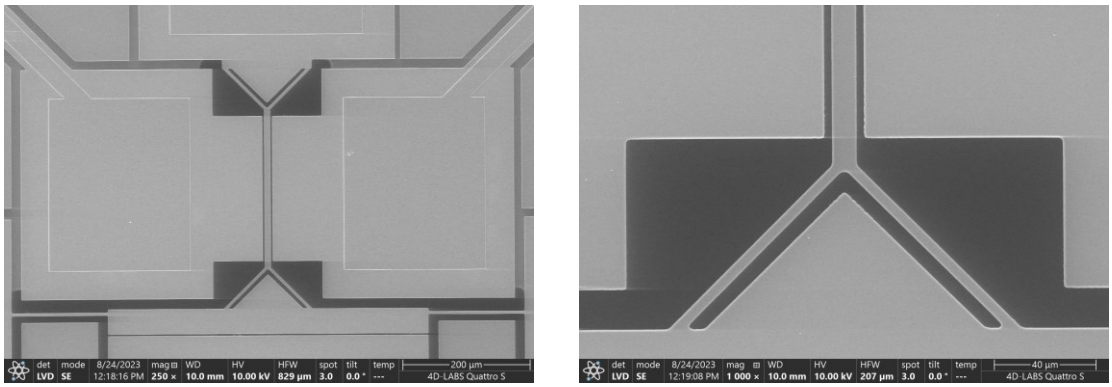

(a) (b)

Figure 4-7 SEM images of the fabricated P-P beam (a) with depiction of electrode configuration (b) the point where beam connected to the anchor as Pinned boundary condition, the extra traiangle structure is for reducing grass and overetching in DRIE step

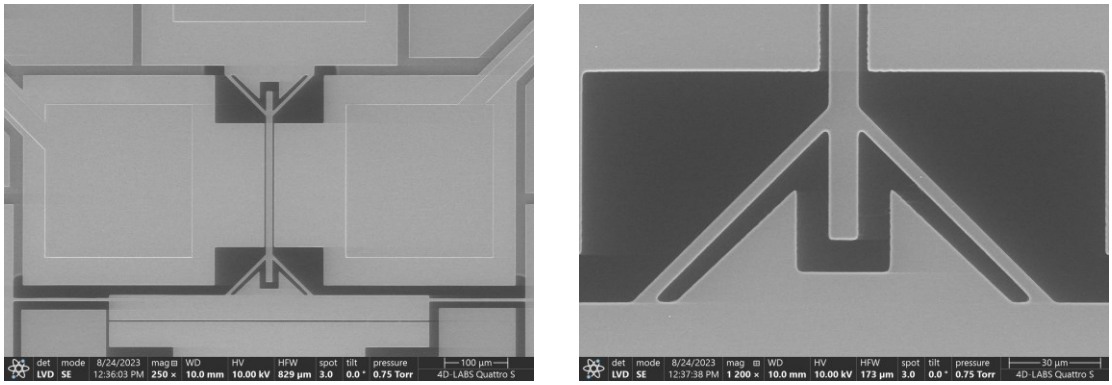

(a) (b)

Figure 4-8 SEM images of the fabricated F-F beam (a) with depiction of electrode configuration (b) the point where beam connected to the anchor as Free boundary condition, the extra triangle structure is for reducing grass and over etching in DRIE step

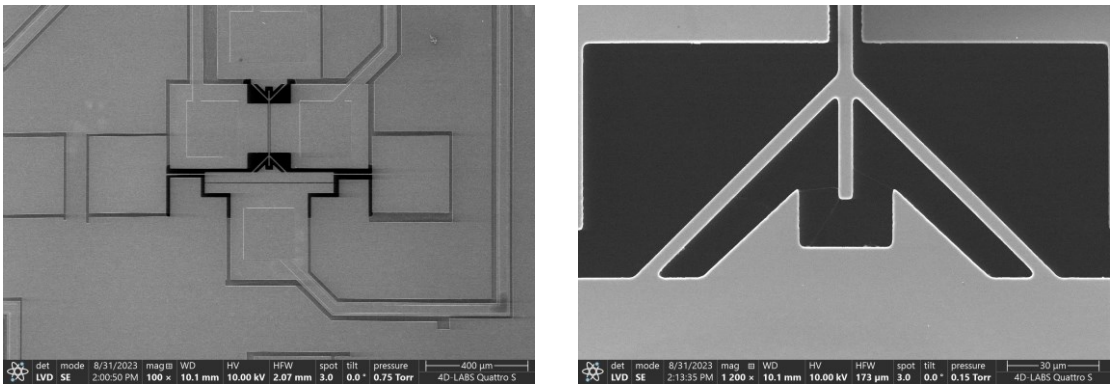

(a) (b)

Figure 4-9 SEM images of the fabricated F-F beam (a) with depiction of electrode configuration (b) the point where beam connected to the anchor as Free boundary condition, the extra structure between the boundary beams and the resonant beam is for reducing grass and over etching in DRIE step.

Final steps involve removing the Buried Oxide layer through a wet oxide etch process and eliminating the front side protection material. This exposes any mechanical Silicon layer structures over the through-holes in the substrate layer. Finally, the wafers are diced.

4.5. Experiments

Following the fabrication process, the devices were subsequently packaged and wire bonded. The packaged devices can be observed in the figure 4-9(a). The Figure 4-9(b) displays an optical microscope view of the fabricated devices, revealing the electrode configurations.

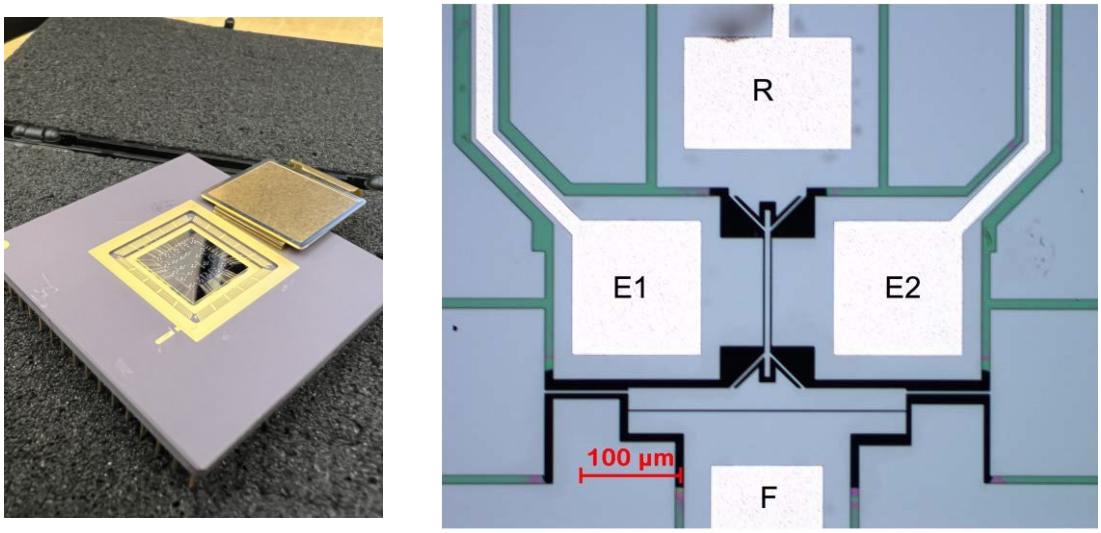

(a) (b)

Figure 4-10 (a) An image of the packaged devices (b) An optical microscope image of the Free-Free beam as an example of the fabricated devices

We discussed the fabricated devices, each featuring a sizable electrode on top, as shown in Figure 4-10 (b), for applying electrostatic force. These devices were positioned within a vacuum chamber, maintaining a vacuum level of approximately 20mTorr to reduce the impact of the external environment. The devices' resonance frequency was determined using a lock-in amplifier and the synchronous demodulation method [104]. To negate any resonance shift caused by electrostatic voltages, all resonant beams were held at a consistent DC voltage during measurements. The innate resonance frequency of each beam was identified by applying the same AC voltage with the lock-in amplifier,

ensuring no electrostatic force. Figure 4-10 shows the schematic of the experimental setup.

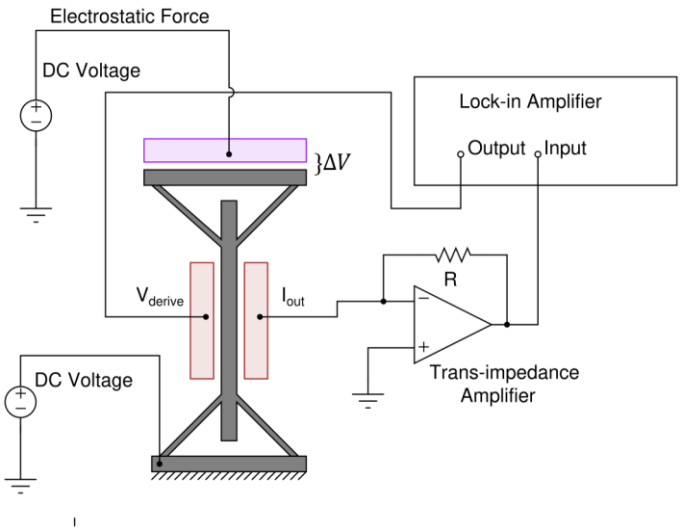

Figure 4-11 the schematic of the experimental setup

Figure 4-12 presents the measured data for the Pinned-Pinned resonant beam, showing its resonance frequency without axial force as a simple of measured resonance signals in this research, similar measurements have been performed on other samples to measure the resonance frequencies and their quality factors.

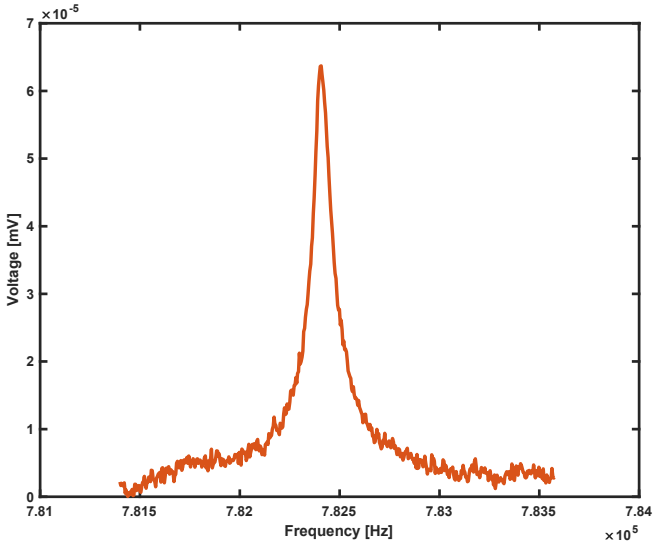

Figure 4-12 sample response for the frequency measurement of a P-P beam after removing the feedthrough signal.

Following the measurement of the resonance frequency of the beam, the subsequent step involves increasing the voltage difference between the resonator and the electrode responsible for applying the electrostatic force. In this scenario, we manipulate the voltage levels between the electrodes, denoted as "F" and "R".

The Figure 4-13 illustrates the response of the P-P resonator and the corresponding shifts in resonance frequency resulting from the application of $0 - 50\ volts$ with the step of $10\ volts$. A clear observation can be made regarding the quadratic relationship between the applied voltage and the corresponding shift in resonance frequency. As we previously established in this chapter, the equations presented indicated a linear relationship between small forces and the change in resonance frequency. However, it is now evident that there exists a quadratic relationship between the applied voltage and the resulting force exerted on the resonators. This aligns perfectly with our prior understanding that the application of a constant voltage on an electrode generates an electrostatic force proportional to the square of the voltage difference on that electrode. We proceed to measure the resultant changes in resonance frequency for all the devices.

For this analysis, we apply a voltage difference of $50\ volts$, which corresponds to a force of $35\ \mu N$ based on the dimensions of the electrode.

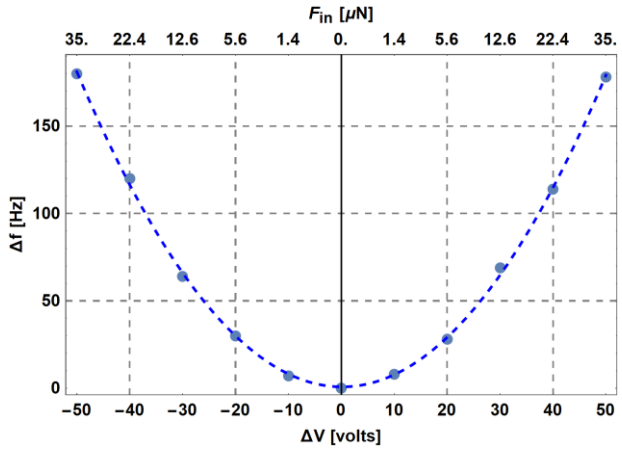

Figure 4-13 the shift in the resonance of the P-P beam due change in the potential difference ΔV, the corresponding electrostatic force shown at the top.

So far, our observations have focused on the effect of applied voltage, specifically the electrostatic force, and the resulting resonance shift in one of the resonators (P-P beam). Having established this relationship, our current objective is to investigate the disparity in resonance shift among the previously introduced resonators discussed in this chapter. The measurement data presented in Figure 4-13 depicts the application of a constant force of $35\ \mu N$ on the electrode, exerting the same force on all electrons. Notably, we observe that modifying the boundary conditions of the beams significantly impacts the sensitivity of these resonators. As demonstrated in Figure 4-13, by applying an equal amount of force, we can observe nearly four times the sensitivity in the free-free beam compared to the Clamped-Clamped. To provide specific values, for the Clamped-Clamped, Pinned-Pinned, Free-Free 1, and Free-Free 2 resonators, we observe resonance frequency shifts of $91\ Hz$, $180\ Hz$, $185\ Hz$, and $402\ Hz$, respectively.

(a)

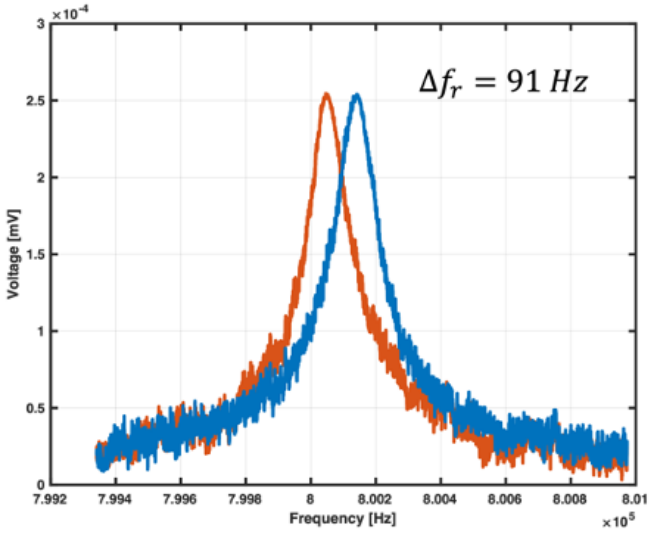
$\Delta f_r = 91\ Hz$
Voltage [mV]
Frequency [Hz]
×10^-4
×10^5

(b)

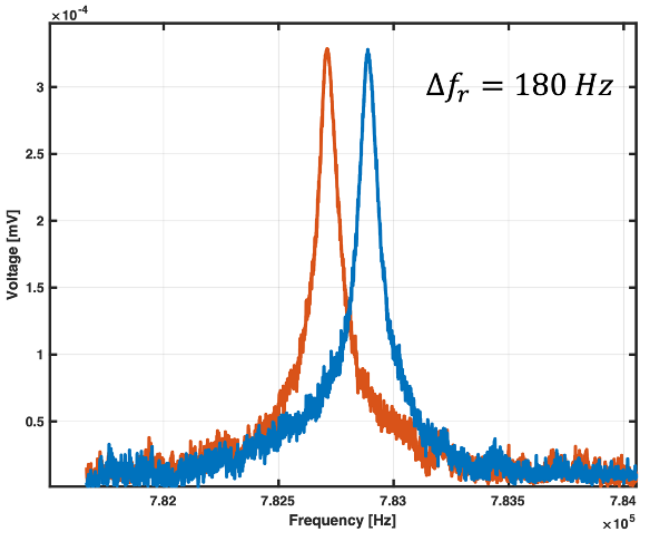
$\Delta f_r = 180\ Hz$
Voltage [mV]
Frequency [Hz]
×10^-4
×10^5

(c)

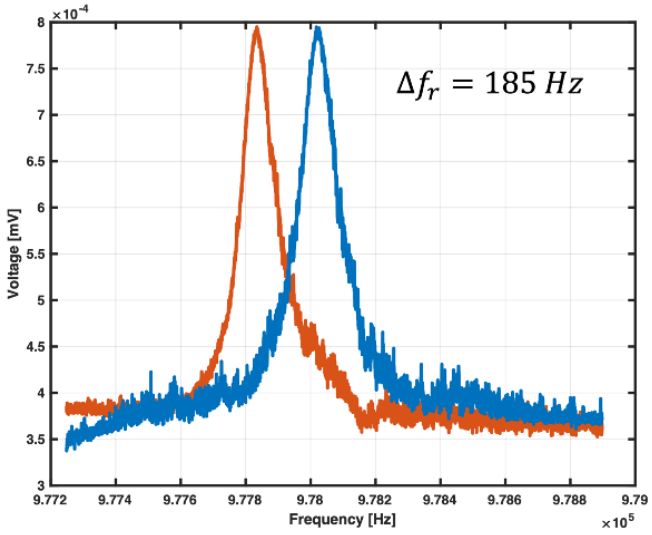

(d)

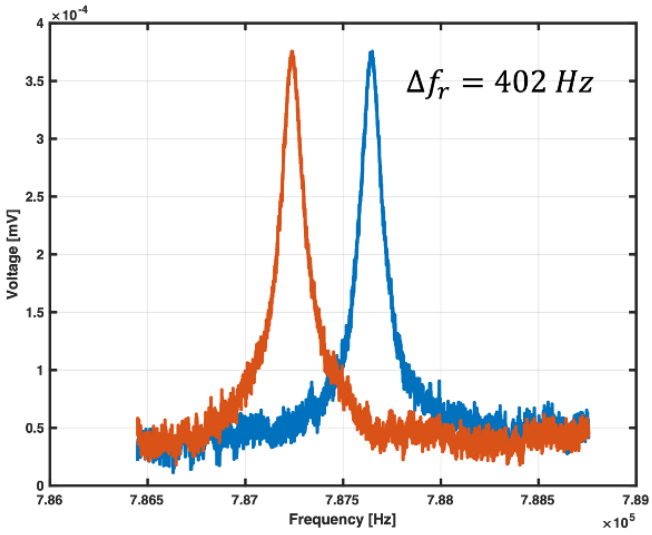

Figure 4-14 Frequency response of the C-C beam and its 91 Hz shift (b) Frequency response of the P-P beam and its 180 Hz shift, (c) Frequency response of the F-F(1) beam and its 185 Hz shift, (d) Frequency response of the F-F(2) beam and its 402 Hz shift, all the frequency shifts are due to application of $35\ \mu N$ *of axial force.*

A summary of the measurement data, simulation results, theoretical data, and their corresponding comparisons can be found in the Table 8.

Table 7 Summary of the beam performances and comparison between theory, simulation, and measurements

Beam Type		C-C	P-P	F-F(1)	F-F(2)
Unloaded Resonance Frequency	Theory	910843	629080	975421	975421
	Simulation	829749	842054	1056970	977690
	Measurement (Q @ 20mTorr)	801085 (8500)	782407 (11500)	847003 (12500)	787646 (15200)
Resonance shifts due to $35\ \mu N$ of force	Theory	105	194	428	428
	Simulation	97	175	180	357
	Measurement	91	180	185	402

The validation of our simulation theory results by our measurement data is evident in the table provided. As observed, the measured values closely align with the simulated values, emphasizing the accuracy and reliability of our theoretical predictions. This congruence between simulation and measurement further strengthens the credibility of our research findings. Moreover, an additional advantage offered by the newly introduced resonators in this study is their higher quality factor compared to the existing. This enhancement in quality factor represents yet another factor contributing to the overall improvement achieved through these designs.

Figure 4-14 presents a comparison between the theoretical, simulation, and measurement results obtained for the investigated beams. The experimental findings align closely with the modeling results, thereby confirming the validity of the design principle. Notably, the F-F beam exhibits a higher sensitivity to changes in boundary conditions, resulting in the most prominent deviation between the experimental and numerical outcomes compared to the theoretical model. This observation highlights the importance of considering and accounting for the impact of boundary conditions when analyzing the

behavior of the F-F beam. The disparities between the experimental and numerical results underscore the need for further investigation and refinement of the model to accurately capture the intricate dynamics of the F-F beam under different boundary conditions. The agreement between the theoretical and simulation results with the experimental data supports the reliability and effectiveness of the proposed design approach. These findings contribute to a deeper understanding of the behavior of the studied beams and provide valuable insights for future research and optimization in this field.

(a)

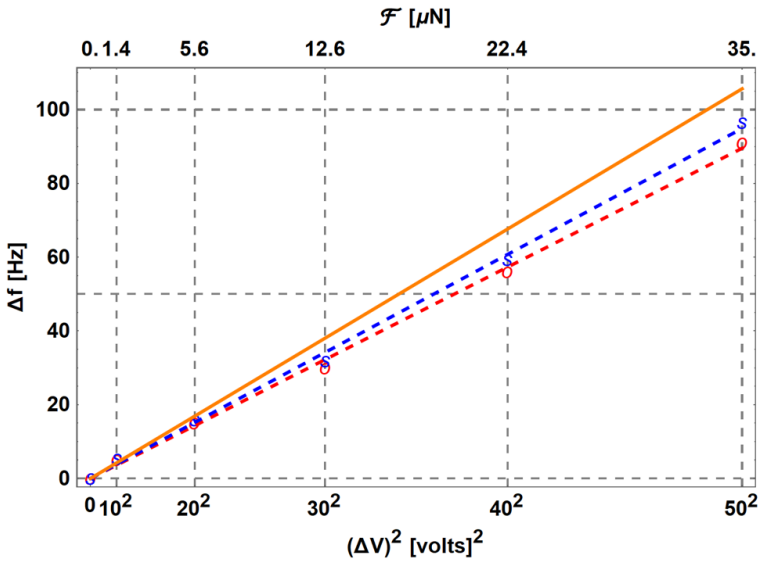

(b)

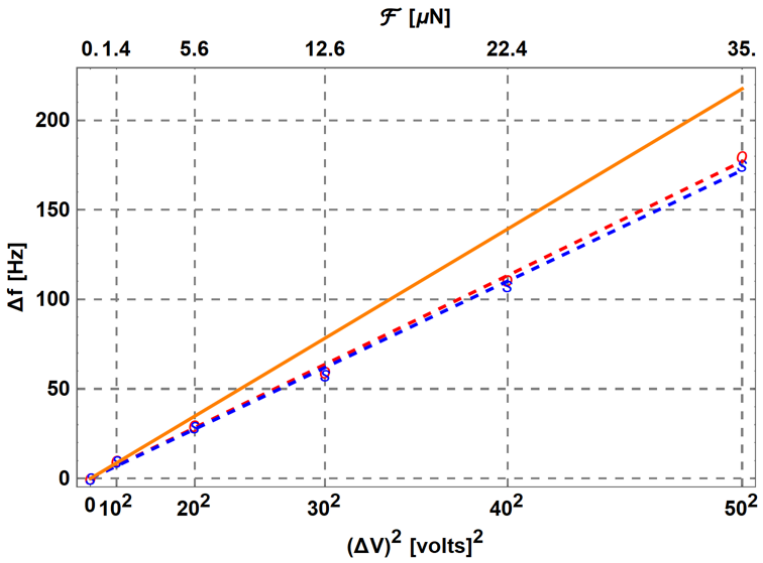

(c)

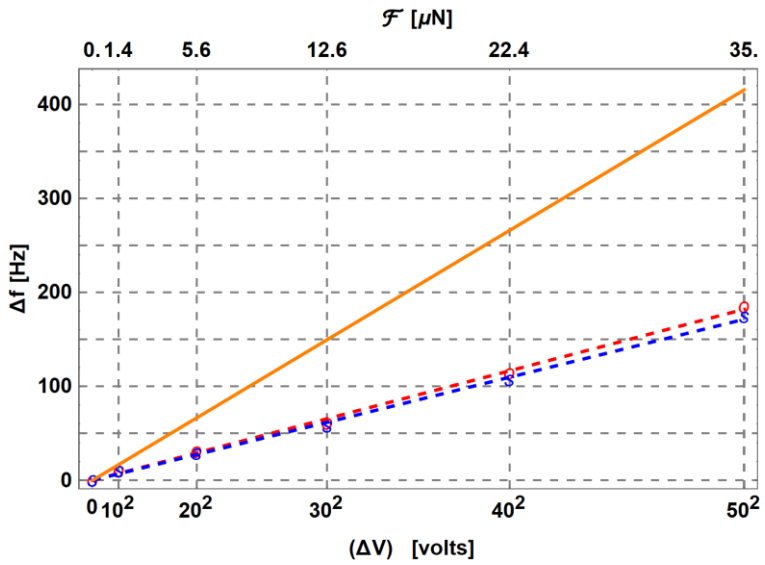

(d)

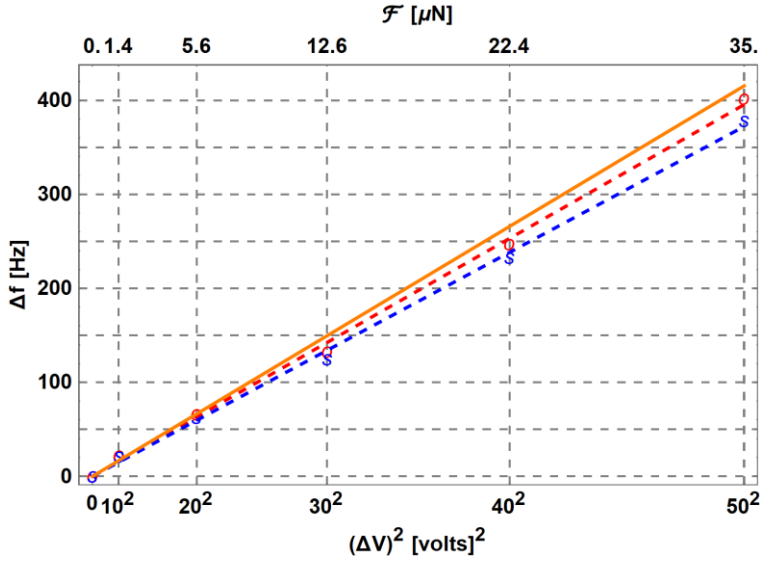

Figure 4-15 the comparison of theory, simulation and measurements of sensitivity for (a) Clamped-Clamped, (b) Pined-Pinned, (c) Free-Free (1), and (d) Free- Free (2). In all Figures the orange line represents the curve obtained from theory, the dashed blue line represents simulation data, and the dashed red line represents the measurement data.

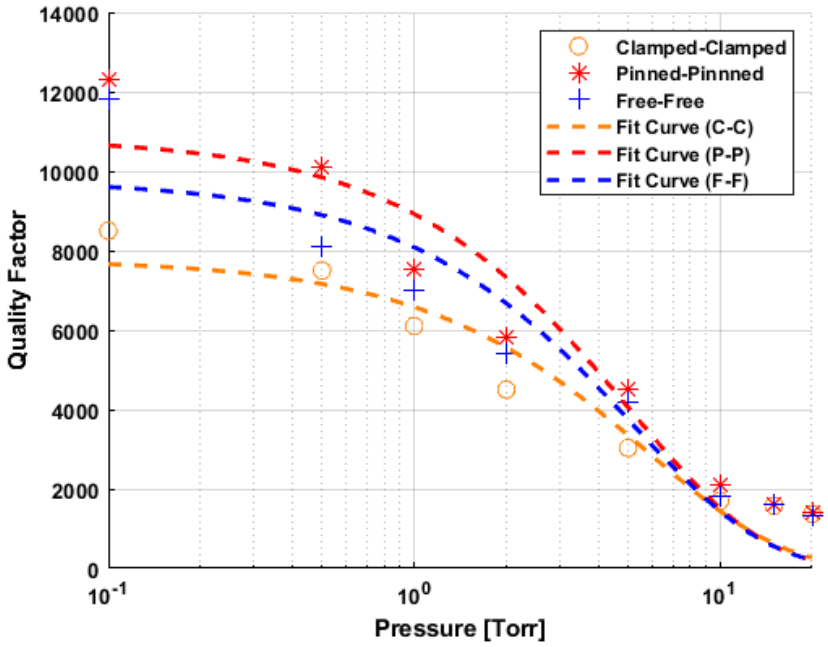

Figure 4-16 Comparison of the Quality factor for C-C, P-P and F-F(1) beams at different ambient pressure

The response of force sensors under different pressures was thoroughly investigated in this study. It is important to note that the primary energy loss mechanism for flexural resonators is viscous gas damping, which can be effectively mitigated by operating at lower pressures. In Figure 4-15, a comparison of the quality factors of the resonating beams under varying pressures is presented. As anticipated, both the P-P and F-F beams demonstrate higher quality factors at lower pressures compared to the C-C beam. This improvement can be attributed to the reduced anchor losses in the modified resonant beam structures, thereby showcasing another advantage of these designs. A higher quality factor signifies enhanced coupling between the electrical and mechanical domains, resulting in a stronger output signal. Simultaneously, a sharper resonance peak contributes to reduced measurement noise when tracking the resonance peak or signal phase shift. Figure 4-16 illustrates a comparison of the signals obtained from the P-P and C-C structures at 15 Torr. At this pressure, the resonant signals of the C-C beam largely overlap, posing challenges in distinguishing changes in resonance frequency. Conversely,

the P-P beam, benefiting from its higher quality factor and sensitivity, exhibits a more

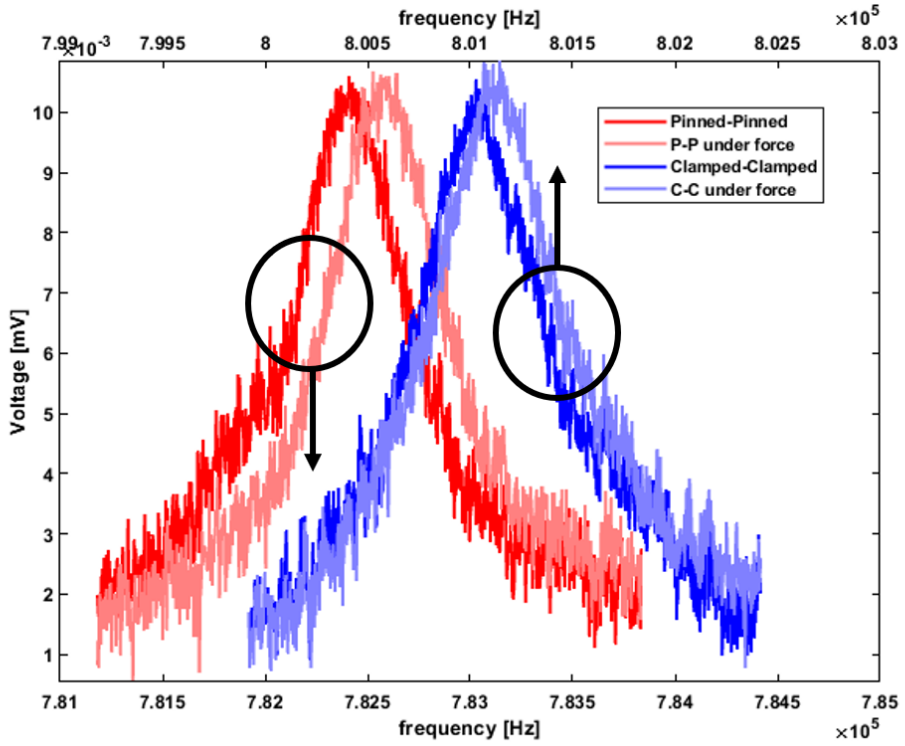

Figure 4-17 Comparison of the resonance shift results for C-C and P-P beams under the same 35μN axial force at lower Q under ambient pressure of 15 Torr.

pronounced shift in its resonance peak for the same input force. This analysis underscores the significant advantages offered by the modified resonant beam structures in terms of improved quality factors, signal strength, and noise reduction. These findings contribute to advancing the field of force sensing and pave the way for further optimization and applications in practical systems.

4.6. Summary

Novel designs for resonant beam force sensors that offer significantly higher sensitivities compared to the conventional clamped-clamped beam structure have been introduced in this chapter. The design principle incorporates unexplored boundary conditions for these force sensors, leading to enhanced performance. Analytical and

numerical models demonstrated for achieving over a four-fold increase in sensitivity. To validate the design principle and assess the feasibility of the proposed approach, sample devices were fabricated and subjected to testing.

An important advantage of the proposed resonant beam force sensor designs is that they can replace the commonly used clamped-clamped beam resonance force sensors in existing resonant micro- and nano-sensor systems without requiring modifications to the fabrication process or the use of different materials. Furthermore, the interface electronics can remain unchanged. This aspect highlights the practicality and ease of implementing these designs into current sensor configurations, allowing for immediate performance improvements.

As highlighted in both the current and preceding chapters, a notable challenge associated with silicon micro resonant force sensors is the high stiffness exhibited by the resonant microstructures. To achieve a significant shift in resonance frequency, a substantial force must be applied to the resonant beam. Consequently, various approaches, such as the utilization of micro levers and other force amplification techniques, have been employed in the literature to enhance the sensitivity of these sensors. While the current chapter introduced novel resonators aimed at increasing sensitivity, the subsequent chapter will delve into the exploration of force amplification methods. In the next chapter, novel force amplifiers will be introduced with the objective of further enhancing the performance of micro resonant force sensors.

Chapter 5. Co-design of Sensing Beam and Mechanical Force Amplifier

Resonant accelerometers, as well as other resonant force sensors, rely on measuring the change in resonance frequency resulting from the application of axial force on sensing beam. In microstructures and micro resonators, axial forces do not cause significant changes in resonance frequency due to their inherent stiffness. The force generated by the acceleration acting on these proof masses is small. This small force is insufficient to produce a significant shift in conventional resonance frequency, thus requiring the implementation of force amplification structures to enhance the system's response. These force amplification structures, typically microlever structures, will be explored in detail in this chapter.

5.1. Micro-Levers

Lever mechanisms, having seen extensive use since the era of ancient time, have persisted through centuries up until the present day. Interestingly, the fundamental principle governing the operation of these lever structures are similar across both macro and micro dimensions. However, when comparing the structures at the micro level with their conventional, larger-scale counterparts, one can observe subtle differences. These disparities primarily result from constraints imposed by microfabrication techniques.

In the realm of the microscopic, creating ideal hinge boundary conditions at the pivot point—common in macro lever structures—is typically unfeasible. Instead, levers at this scale are often constructed from two co-planar flexures [105]. The ends of these beams are anchored to the overall structure, thus forming a mechanism akin to a lever but with distinct micro-level characteristics. This provides us with a basic understanding of the difference we encounter when transitioning from the macro world of conventional levers to the micro world of lever structures.

The potential of harnessing force amplification mechanisms, specifically micro-leverage mechanisms, to enhance the force applied on resonant and sensing beams was initially demonstrated in the literature over two decades ago. It was during this period that pioneering research by Roessig [52] illustrated the benefits of leveraging this system to amplify the force exerted on a tuning fork, thereby maximizing the scale factor available for the small inertial mass.

In the following years, Su [106] introduced a more comprehensive model focused on one-stage and two-stage force amplifiers and micro-leverage structures, with particular emphasis on resonant sensors [59], [105], [107], [108]. Researchers subsequently designed further models based on these principles. There has been a significant amount of research conducted on various force amplification techniques [34], [109], [110], [111], [112]. This research has also encompassed the design and optimization of these force amplifiers.

Over the past two decades, these structures have been extensively utilized, as evidenced by their frequent appearances in literature. This not only highlights the practical relevance of these mechanisms but also shows their significance within the field. During this study, we undertake a review of the fundamental structures that have been consistently referenced in the literature. An efficient, concise introduction to these structures is provided for the familiarity with their basic concepts. In the next subsection, we shift our focus to the co-design of the resonant beams and amplification mechanisms that are being presented in this research. These novel structures have been designed with the primary goal of enhancing the sensitivity of resonant accelerometers.

The Figures 5-1 and 5-2 illustrate two common structures used as leverage mechanisms. These configurations comprise a primary, long beam functioning as the main lever beam, coupled with three smaller, attached beams. One of these three beams serves to apply an input force, represented here by $'F_{in}'$. Another beam is responsible for transmitting this force to the resonator, thereby generating an output force, denoted as $'F_{out}'$. The third beam is uniquely connected to the pivot point of the resonator. Each of

these beams has distinct dimensions length and width as depicted in the Figure 4-1 and 4-2

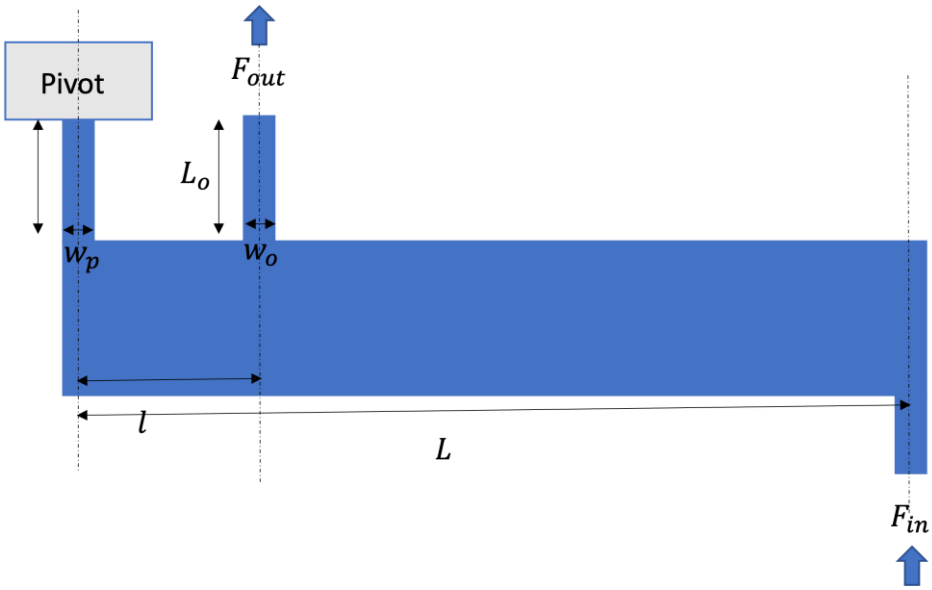

Figure 5-1 microlever structure with positive force amplification

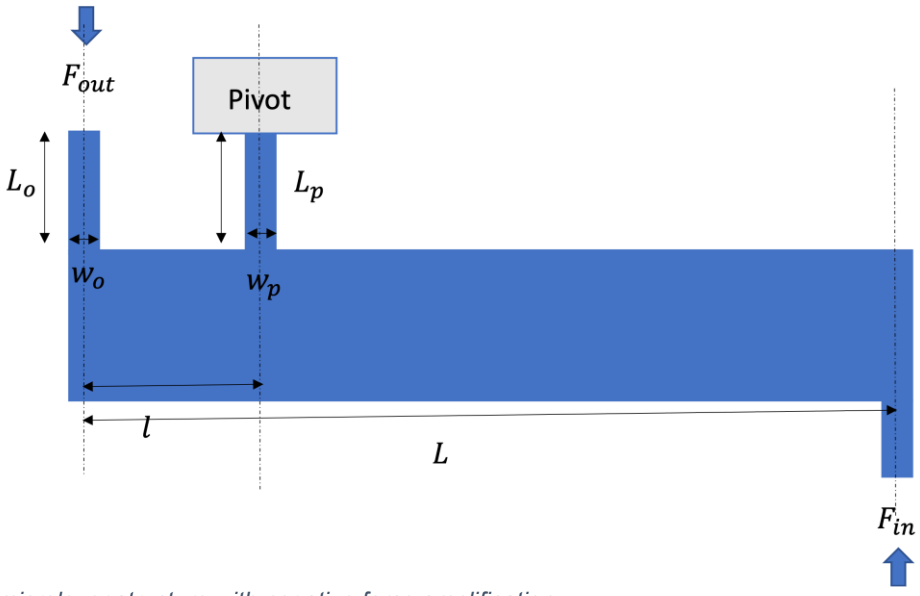

Figure 5-2 microlever structure with negative force amplification

In the first configuration, the output beam is positioned between the pivot and the input beam. Conversely, in the second arrangement, the pivot beam is located between the input and output beams. This positioning difference impacts the directionality of force. In the second structure where the pivot beam lies between the input and output beam, the output force is exerted in the opposite direction of the input force (negative force amplification).

Principles of balance and conservation of energy fundamentally govern the operation of leverage mechanisms. In an ideally constructed system – featuring a stiff, unbending lever arm and a pivot that perfectly preserves energy while allowing rotation– balance must be achieved at the pivot point. With the lever at a static equilibrium, the product of the input force (F_{in}) and its distance from the pivot (L) matches the product of the output force (F_{out}) and its distance (l); this can be summarized as $F_{in}L = F_{out}l$.

From an energy conservation standpoint, the work done by the input force should match the work done by the output force, provided no energy loss occurs due to strain at the pivot or flexure beam bending. For a flexible mechanism, the energy introduced should be equivalent to the summation of the output energy and the elastic energies exerted during the flexing of the components. Employing a lever to achieve a particular function often necessitates a compromise between the force employed and the displacement achieved.

The leverage ratio, denoted by L/l, represents the maximal mechanical or geometric advantage that a leverage mechanism can attain. In the context of force amplification, this ratio can also be referred to as the amplification factor, denoted by 'A_F'. This factor essentially represents the relationship between the output force and the input force. Similar analytical methods can be applied to the two types of microlevers.

When an input force is applied, it causes the lever arm to rotate slightly and displaces it by a minimal distance. This loaded system can be conceptually represented as illustrated in Figure 4-3. Here, the flexural pivot is represented by a combination of a torsional spring and a vertical spring.

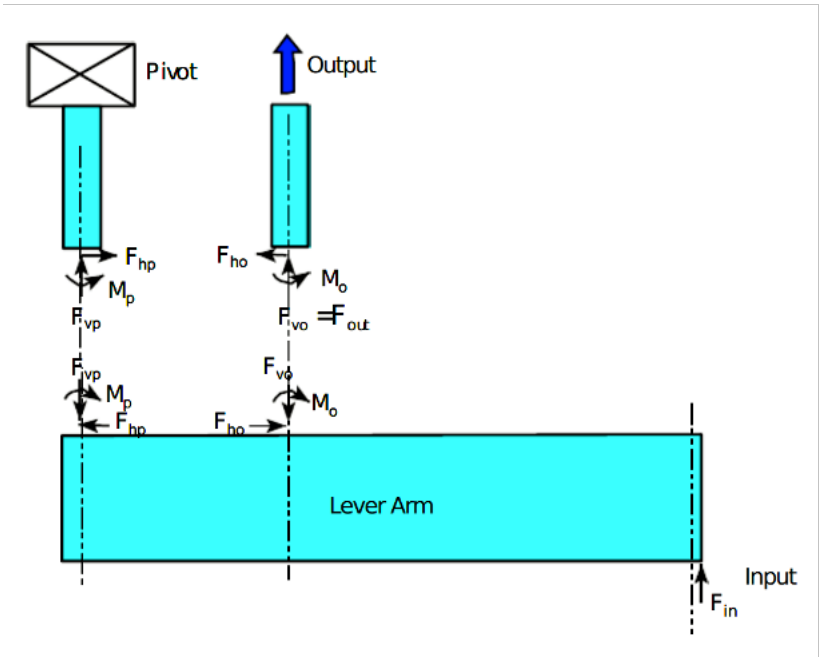

Figure 5-3 Schematic view of the lever with depiction of the forces and momentums [105]

By applying the principles of force and moment equilibrium, specifically in relation to the joint connecting the pivot beam and the lever arm, we derive the following equations [113]:

$$F_{in} = k_{vvo}(l\theta + \delta) + k_{vvp}\delta$$

$$F_{ho} + F_{hp} + F_{hi} = 0 \qquad (5.1)$$

$$F_{in}L = kvvo(l\theta + \delta)l + M_o + M_i + M_p$$

Where in these equations, $'F_{in}'$ represents the input force. $'k_{vvo}'$ refers to the vertical (denoted by the first subscript $'v'$) spring constant of the output (indicated by the third subscript $'o'$) system under a vertical (designated by the second subscript $'v'$) force. Similarly, $'k_{vvp}'$ denotes the vertical spring constant of the pivot under a vertical force. $'k_{\theta mo}'$ is the rotational spring constant of the output system when subjected to a bending

moment, while $'k_{\theta mp}'$ stands for the rotational spring constant of the pivot under a similar load. By collectively solving these equations, we can compute the ratio of ouput and input forces of the lever [105]:

$$\frac{F_{out}}{F_{in}} = \frac{\frac{1}{K_{ap}}\left(k_{to} + k_{tp}\right) + lL}{\left(\frac{1}{k_{ao}} + \frac{1}{k_{ap}}\right)\left(k_{to} + k_{tp}\right) + l^2} \tag{5.2}$$

Where 'K_a' is the axial spring constant and $'K_t'$ is the torsional spring constant, and subscript 'o' and 'p' represents output and pivot beams. K_a and K_t can be calculated from the following equations [105]:

$$K_{ti}(w_i, h, L_i, G) := \frac{G}{L_i} \times \left(\frac{h}{2} \times \left(\frac{w_i}{2}\right)^3 \times \left(\frac{16}{3} - 3.36\frac{w_i}{h} \times \left(1 - \frac{w_i^4}{12 \times h^4}\right)\right)\right) \tag{5.3}$$

$$K_{ai} = Ey \times w_i \times \frac{h}{L_i} \tag{5.4}$$

Where 'w' id the width, 'L' is the length, 'h' is the thickness, 'E' is the Young's module, and 'G' is the Shear Module.

The Figure 4-4 illustrates the amplification factor for a lever structure with a length of 2015 microns. The factor is plotted against various values of $'l'$. The plot reveals a highly nonlinear relationship with respect to $'l'$. Notably, as 'l' increases, we observe a peak at the halfway mark. For this lever structure, we utilize values presented in Table 9.

Table 8 Summary of the values for the parameters of the microlever used for theoretical calculations.

w_p	$5\mu m$	w_o	$5\mu m$
L	$2050\ \mu m$	E	$170\ GPa$
L_p	$15\mu m$	L_o	$10\mu m$
G	$60\ GPa$	h	$100\mu m$

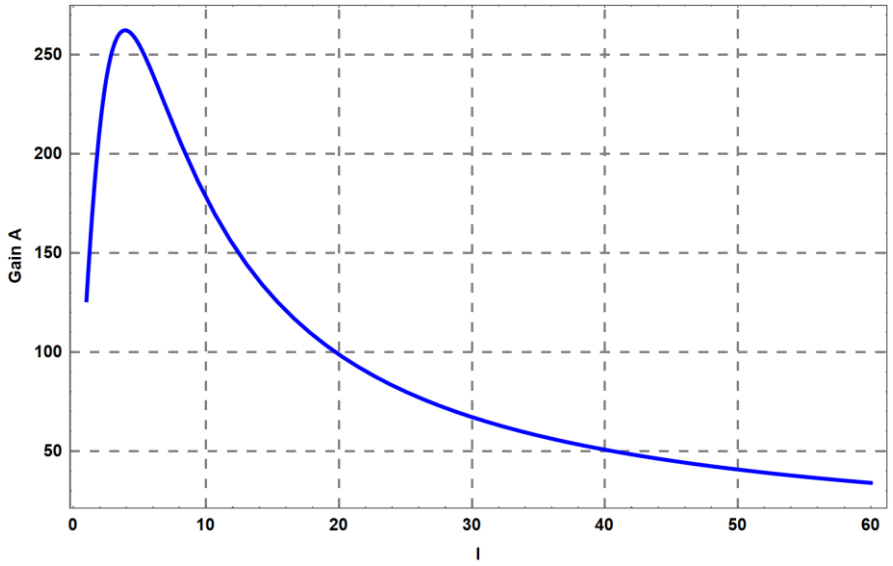

Figure 5-4 the theoretical amplification factor versus different values for l while other parameters are set as values shown in Table 8, in the figure, the unit for horizontal axis is μm

It's important to note that the graph depicted in Figure 5-4 was calculated without considering the lever's connection to any resonator. This omission can be likened to designing a voltage amplifier in electronics without accounting for the connection to a low resistance load, which invariably affects the amplifier's output resistance and consequently its amplification gain. Drawing a parallel with mechanical systems, when a

lever is connected to a resonator or output, this connection imposes a loading effect on the lever. This, in turn, reduces the level of amplification.

As can be seen in Equation 5.2, the amplification afforded by this system is directly proportional to the total stiffness connected to the amplifier's output. As another resonator is connected to this output, the total stiffness undergoes a change, taking into account the stiffness, or the spring constant, of the newly connected resonating beam. By theoretically considering these factors, we can calculate the impact on the system's amplification capability. The figure 4-5 illustrates the impact of connecting a lever to a resonator and contrasts it with the amplification of an unloaded lever. The employed resonator possesses a length of 300 µm and a width of 5µm.

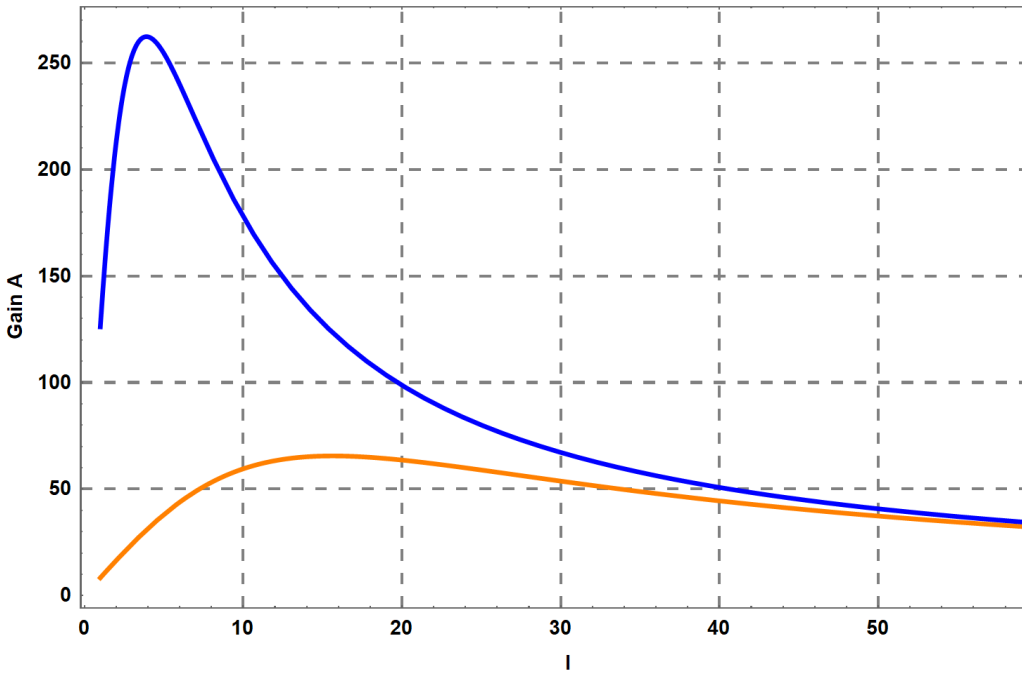

Figure 5-5 The effect of adding a resonant beam on amplification factor (Orange line) compared to a unloaded lever (Blue line), the unit for the horizontal axis is μm

Figure 4-5 highlights the need to design the microbeam and micro-level structure together. These two structures need to be designed concurrently for optimal system

performance. It's important to note that neither the micro-lever nor the micro-resonant beam can be designed separately. In this thesis, we focus on combining the design of the micro-lever and resonant beam. Our goal is to improve the structure's sensitivity. We'll start with a basic design and later compare it with new designs. As observed, the two values approximately converge around a length of 50 microns. Taking into account the fabrication guidelines and design parameters, we have opted for a length of 50 microns for our design moving forward. In subsequent design sections, we will utilize this 50-micron length as a benchmark. This will facilitate comparisons among different micro-lever structures and their relative performance.

It's important to highlight the "amplification factor" presented in the earlier equation. In our analysis, we overlooked the bending that occurs within the micro-lever structure. When an input force is introduced to the lever, not all energy is directed to the output. A portion is expended due to the bending of the structure and the microbeams. Furthermore, the force often originates from the proof mass, which is attached to a suspension beam. This suspension possesses its inherent stiffness and spring constant, both of which influence the force's transfer to the lever. In essence, the actual amplification might be notably lower than projected since we omitted the effects of internal bending for the sake of simplification. Existing literature typically suggests that a wider microbeam is preferable, as it tends to behave more like a rigid body.

5.2. Designs and Simulations

Having explored the characteristics of micro-lever structures, the amplification factor, and their influence on resonant force amplifiers in this chapter, we will now extend our investigation into the design of these micro-lever structures. This follows our discussion in the previous chapter where we examined the impact of boundary conditions on enhancing the sensitivity of resonant force sensors. In this chapter, our objective is to assess the influence of micro-lever structures on the resonators introduced earlier, as well

as to present novel designs. Ultimately, such enhancements are expected to contribute to the overall sensitivity of the sensor.

Figure 5-6 illustrates the lever that we are examining in this analysis. This lever bears a resemblance to the one depicted in Figure 5-4, often referred to as the "First kind" lever amplification in the literature. Notably, there is a sizable electrode positioned on the input side. In our simulations, this electrode serves the purpose of applying force, and we also employ it in drawing the layout to exert an electrostatic force on the lever. In the experimental section, we will delve into the details of the experimental results and various aspects of the design.

On the output side, we connect the resonators with different boundary conditions and subsequently measure the shift in resonance frequency for these resonators due to the application of a constant force. The results obtained from these measurements are then compared to each other to assess the effects of the lever on the resonators' performance.

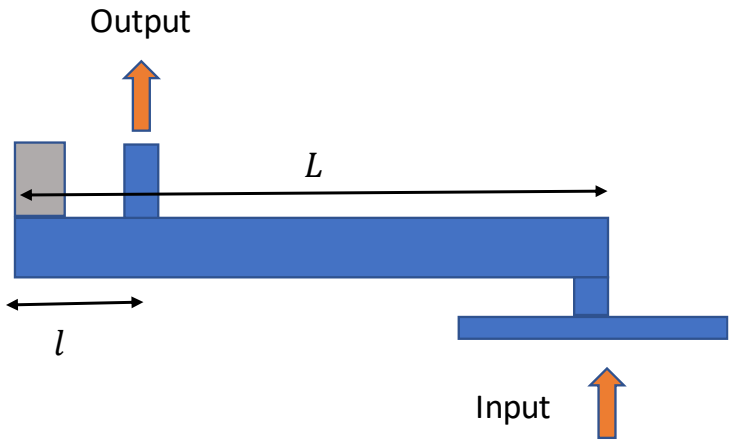

Figure 5-6 Schematic of the lever structure

We maintained a fixed distance of approximately 50 Micron between the pivot point and the resonant beam. By establishing this as our baseline design, we could assess and

compare the overall sensitivity of the entire system, effectively combining the resonator and the lever.

The initial phase in designing the micro-liver structure involves positioning the resonators onto a lever structure. Our aim is to analyze the overall sensitivity of these devices through simulation. The Figure 5-7 depicts the micro-level structure featuring the clamped-clamped beam. Subsequently, the same structure is presented with the free-free beam. From previous sections, it has been established that the sensitivity of the free-free beam surpasses that of the clamped-clamped beam. It is pertinent to note, however, that in structures discussed in the preceding chapter, the boundary beam was considerably thinner than the resonant beam. In the current structure, both the boundary and resonant beams share identical widths. Given that these beams possess the same width, we anticipate that the increase in sensitivity may not be as pronounced when compared to structures with thinner boundary beams. Ultimately, our objective here is to analyze the overall sensitivity of the micro-lever, taking into account both the boundary and resonant beams.

Figure 5-7 and Figure 5-8 present a comparison of these two structures, illustrated in a schematic format for easier comparison. To streamline future comparisons and accommodate the introduction of additional designs, we have named the lever and the resonator depicted in Figure 5-7 as "Design C-C." Similarly, the lever shown in Figure 5-8 is designated as "Design F-F." In both systems, the capital $'L'$ represents the length of the lever from the center of the pivot point to the center of the small beam that applies the input force. Additionally, $'l'$ denotes the distance from the center of the pivot point to the center of the resonator beams.

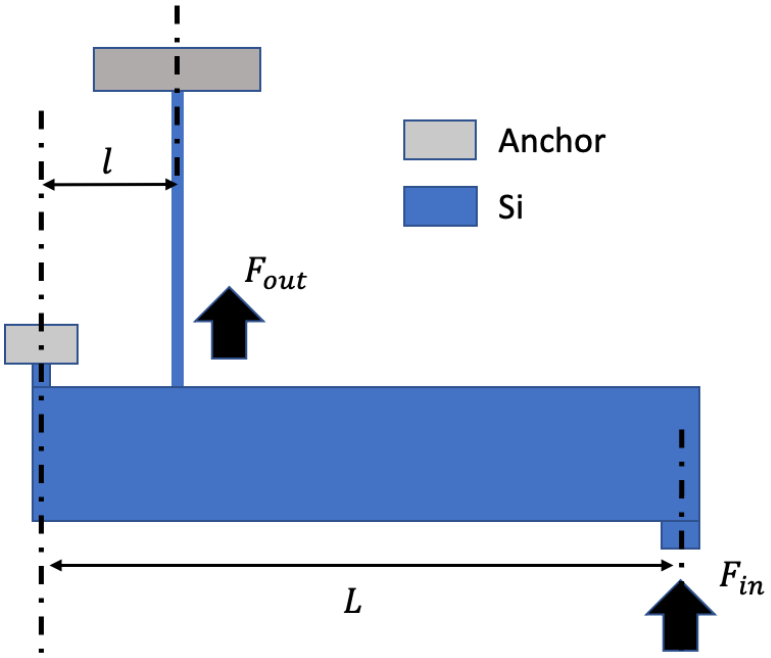

Figure 5-7 Design "C-C-Lever": Schematic of microlever structure along with a Clamped-Clamped resonator.

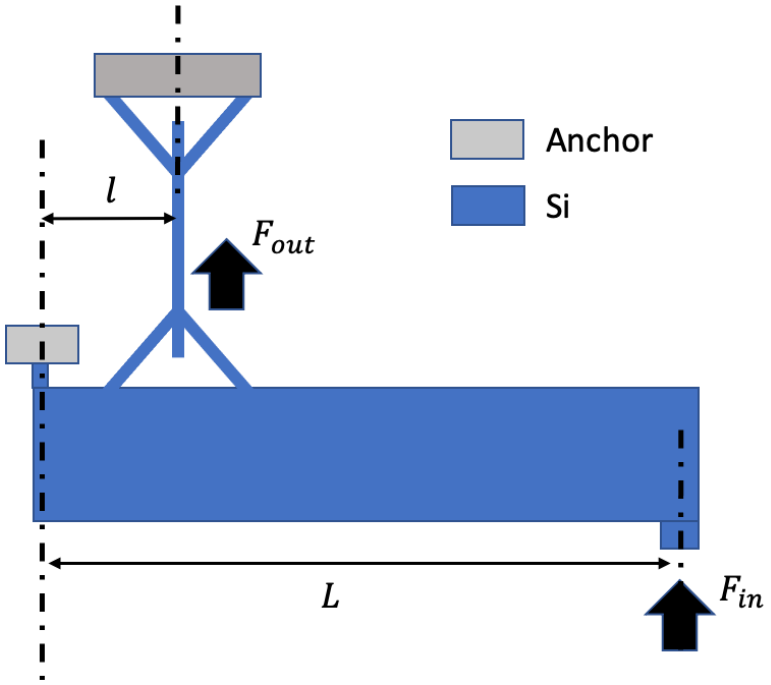

Figure 5-8 Design "F-F-Lever": schematic of a microlever structure along with a Free-Free beam resonator

So far, the levers introduced were standard ones that have been used extensively in the literature, Here, we introduce two innovative structures, coupled with resonator structures, aiming to enhance sensitivity. To achieve this enhanced sensitivity, a notch was incorporated into the lever structure. This notch facilitates greater displacement in the lever, allowing for amplified responses. Displacement is essentially a reflection of the force exerted on the same resonator. As depicted in the accompanying figure, by adding a notch between the two boundary beams of the resonator, the notch can experience increased bending. This additional bending results in greater displacement, bringing the two boundary beams closer to each other. Even a minuscule increase in displacement can lead to a larger force applied to the resonator. Detailed illustrations of this novel lever design can be found in the Figure 5-9. We have designated this system as "Design F-FNotched." Moving forward, we will refer to it as "Design C" to present the results from our simulation experiments. In this illustration, "W_N" corresponds to the depth of the notch, while "L_N" is the length of the notch.

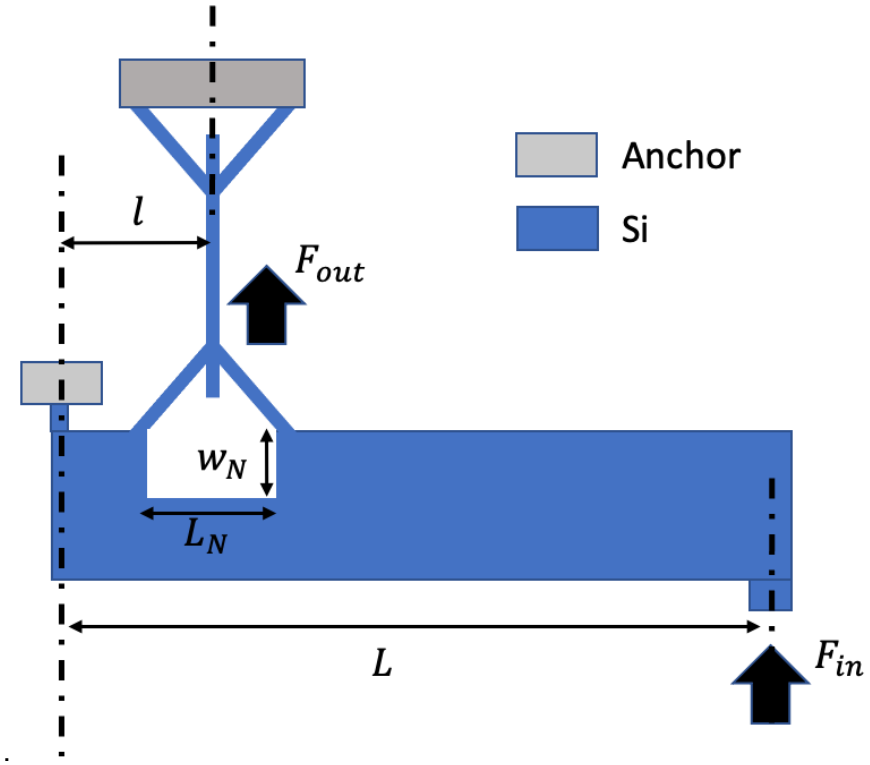

Figure 5-9 Design "F-F-Notched Lever": the schematic of novel micro-lever structure with a notch along with a Free-Free beam

Earlier in this chapter, we highlighted that the total amplification factor of the lever within the structure is determined by the axial stiffness of the resonator attached to it. If the resonator's axial stiffness is insufficient, it will diminish the amplification effect of the micro-lever structure. For instance, an increased length of the beam tends to reduce its overall amplification. With this understanding, we introduced a novel resonator design. Instead of the free-free beam, we incorporated the "Free-Clamped" design to increase the axial stiffness of the resonator beam. This adjustment aims to yield a higher amplification factor from the micro-lever structures. In the subsequent design we present, a free-clamped beam is paired with a micro-lever structure featuring a notch. The figure 4-11 presents a schematic of this design. As depicted, we have employed a clamped-free structure, which is integrated with a micro-lever structure accompanied by larger beams. Similar to previous designs, we will refer to it as "Design C-F-Notched Lever" to present the results from our simulation experiments.

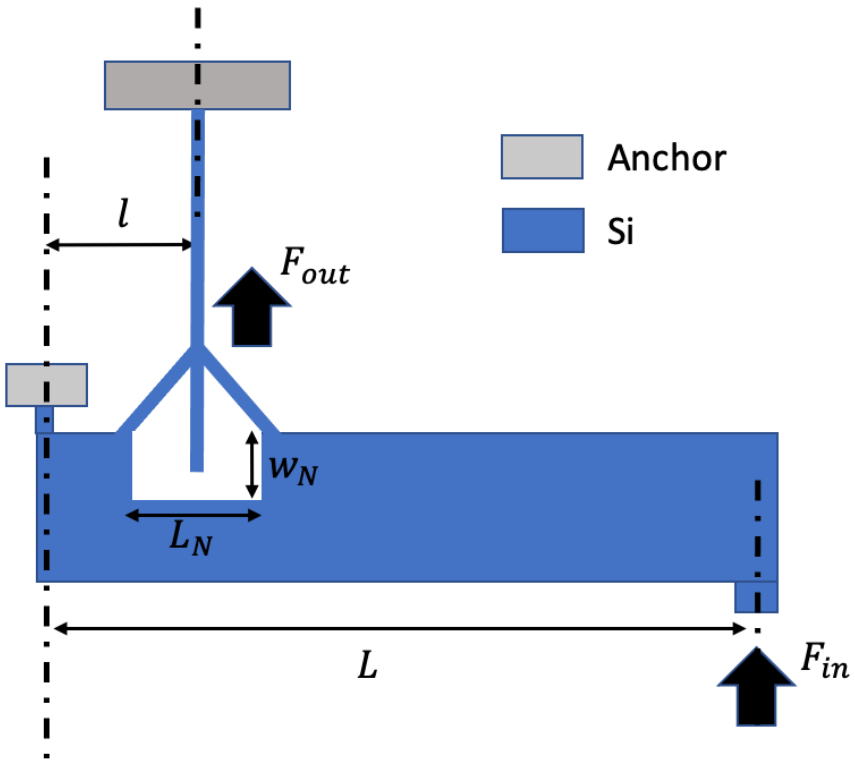

Figure 5-10 Design "C-F-Notched Lever": the schematic of a Clamped-Free resonator with a notched microlever structure.

We will compare the dimensions of these resonators and levers. The table below summarizes the dimensions of the systems introduced earlier in this subchapter. As discussed in the previous chapter, to achieve free boundary conditions, the connection point between the resonator beam and the boundary beam should be proximate to the node of the resonator's mode shapes—where the vibration of the beam is minimal and approaches zero. Given that we have a notch allowing the resonator to move within the structure, we can utilize this space. The resonator remains connected to the beam at the node of the vibration mode, explaining why the length of this beam is shorter than that of the boundary beam in a standard Free-Free beam presented in the previous chapter. We intend to simulate these structures and assess their overall sensitivity, as well as a comparison of the performances. However, before proceeding, it is essential to determine the shape, and the deflection pattern of the lever itself. We will address these considerations initially.

Table 9 Summary of the dimensions of the resonator-lever systems

Design	Resonator Type	Lever Type	Dimensions [in μm]			
			Resonant beam	Boundary beam	Lever beam	Notch
C-C-Lever	C-C	Regular	Length=300 Width=5	NA	Length=2040 Width=100	NA
F-F-Lever	F-F	Regular	Length=324 Width=5	Length=91 Width=5	Length=2040 Width=100	NA
F-F-Notch	F-F	With notch	Length=324 Width=5	Length=91 Width=5	Length=2040 Width=100	Length=80 depth=50
C-F-Notch	C-F	With notch	Length=370 Width=5	Length=59 Width=5	Length=2040 Width=100	Length=80 depth=50

When this lever is coupled with a proof mass in an accelerometer structure, it moves similarly to a clamped guided beam. To ensure that the lever device does not deviate laterally and truly behaves like a clamped guided beam, which is consistent with typical accelerometer structures, we introduced an additional beam (Figure 5-11). This was attached to the free end of the lever to increase its resemblance to the clamped guided beam. Though we designed this beam to be thin, ensuring its stiffness remains lower than the primary lever beam, it does not significantly affect the deflection shapes of the lever. Additionally, another electrode was introduced on the opposing side to facilitate

force application in both directions when necessary. As depicted in Figure 5-11, one end of the lever beam is connected to a pivot pin, which is subsequently connected to an anchor. Consequently, one end of the lever beam remains relatively stationary, while the other end—where force is applied to the structure—has more freedom of movement.

Additionally, we've placed a sizable electrode on the structure. In later measurements, we will use electrostatic force to act upon the resonator and the lever. In our simulation, force is applied to this electrode to replicate anticipated outcomes. Figure 5-11(a) displays the lever structure alongside the beam, using “Design C-F-Notched Lever” as a representative example, although this process was consistent across all structures previously discussed. Figure 5-11(b) showcases the same lever structure under applied force, illustrating the bending of the beams. Figure 5-12 highlights the beam's primary vibration mode, representing the initial resonance mode for the clamped-free beam. We aim to observe the resonance frequency shift of this beam when axial force is applied to the lever.

(a)

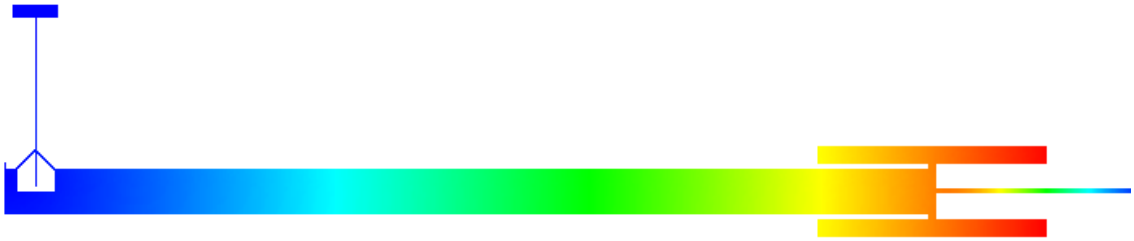

(b)

Figure 5-11 (a) Design (C-F beam with notched lever) in FEM simulations without input force (b) the same system with input force.

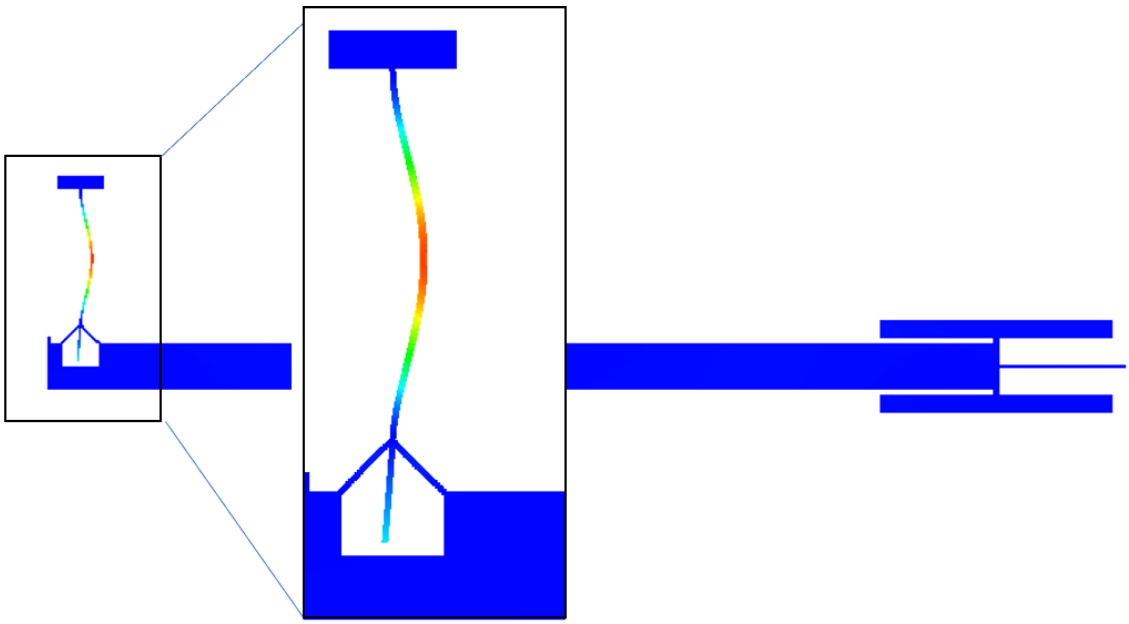

Figure 5-12 The first vibration mode of the C-F beam attached to a lever with a notch, the colors represent displacement qualitatively, red for Maximum displacement, and blue for no displacement.

To conduct simulations for these devices, we applied a force of $12.5\mu N$ to one of the electrode. The other electrode maybe used to apply the force in the other direction and does not affect on the performance of the system Subsequently, we observed the shift in resonance and determined the overall sensitivity of each system, quantified in $Hz/\mu N$. Furthermore, we recorded the resonance frequency for each device. As highlighted in the preceding chapter, for a more accurate comparison, it is essential that the new resonator system and the sensing element operate at the same frequency. Thus, we adjusted the dimensions of our models to ensure that each device's resonance frequency was consistent, enabling a comparative analysis of their relative sensitivities. The Table follows outlines the resonance frequencies and sensitivities of the simulated devices. From the results, it is evident that there has been a noteworthy enhancement in the system's sensitivity, with an increase of 20%.

Table 10Summary of the simulation results for the resonator-lever systems presented.

Design	Resonance Frequency [in Hz]	Sensitivity [in $Hz/\mu N$]
C-C-Lever	486046	31
F-F-Lever	524386	32
F-F-notch	518798	36
C-F-notch	501991	38

5.3. Fabrication

To validate our design principles and further delve into experimental designs, sample devices were fabricated. The devices were fabricated in-house at Simon Fraser University, utilizing two distinct clean room facilities available on-site: the Engineering Science Clean Room (Class 1000) and 4DLabs Clean Room (Class 100). The fabrication

process employed a highly doped silicon-on-insulator wafer. The process consists of two deep reactive-ion etching (DRIE) masks: one for the front side of the device layer and another for the handle layer. Fabrication process required numerous trial runs to ensure the parameters and procedures were optimized for maximum yield and high-quality device fabrication. In this section, we will delve into the fabrication process. After outlining all the stages, we will address some of the significant challenges encountered during fabrication. The Figure 4-13 presents a schematic used for the device layout. This is a section of the layout, which has been consistently replicated for other devices and resonators. In the depiction, there is a sizable electrode at one end, and this electrode is connected to various types of resonators and levers. This structure serves as a blueprint for the fabrication of devices within this process.

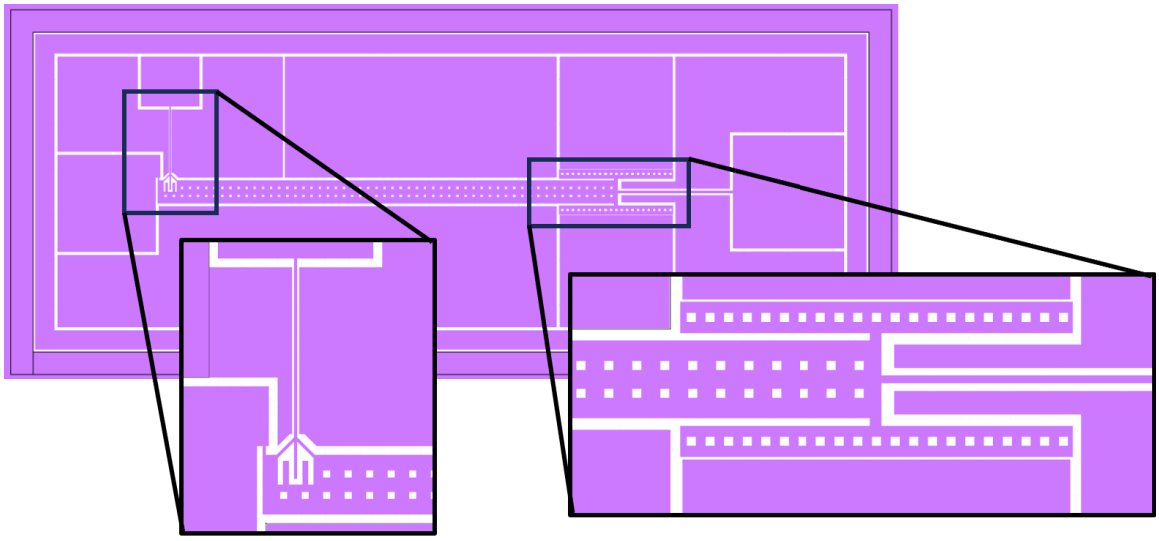

Figure 5-13 An example of the lever design layout and showing the resonator and force electrodes in more details.

Silicon-on-Insulator (SOI) Wafer Preparation and Oxidation

Initiating the microfabrication is the SOI wafer, a. wafer\ comprising of pure silicon, insulating oxide, and another layer of silicon. This chosen 6-inch, 500-µm-thick wafer, with <100> crystal orientation, serves as the foundational substrate. To create an insulating barrier and to pave the way for subsequent processes, a 2µm layer of SiO2 was thermally

grown. This oxidation process is vital as it establishes a robust masking layer for later etching steps. The device layer of these wafers is highly doped with boron, resulting in p-type doping. The resistivity of these wafers is approximately $1 - 5\ m\Omega - cm$.

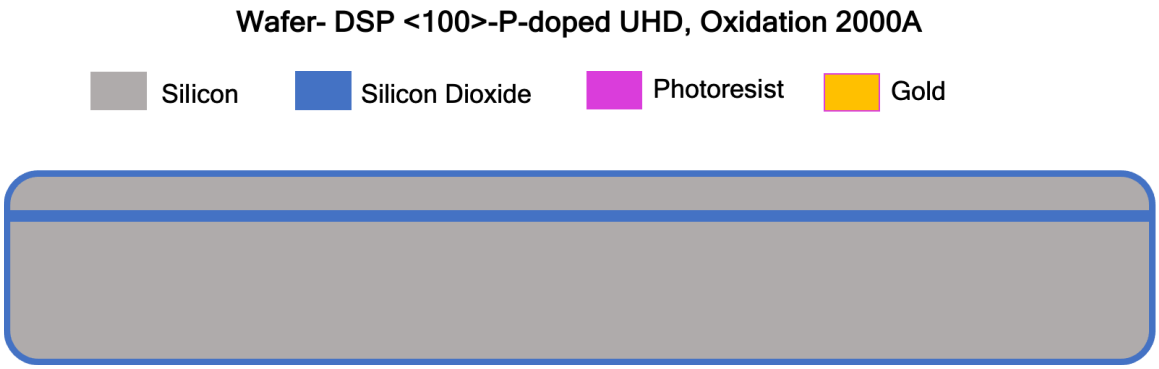

Figure 5-14 Oxidized SOI wafer with 2um of oxide on surface and 2um of buried oxide

Photolithography for Front-Side Patterning

A key step in microfabrication is photolithography, which transfers the desired patterns onto the wafer. This step include 10 minutes HDMS priming. The wafer's top side was uniformly coated with $1\ \mu m$ of AZ703 photoresist using spin coater at 1200rpm for 1 minute, 1-minute soft bake at $90℃$, one minute hardbake at $110℃$. Upon exposure to ultraviolet (UV) light through a mask for $80\ mj/cm^2$, followed by the development process for 55 seconds that removes the exposed areas based on the positive photoresist used, thus translating the mask pattern onto the wafer.

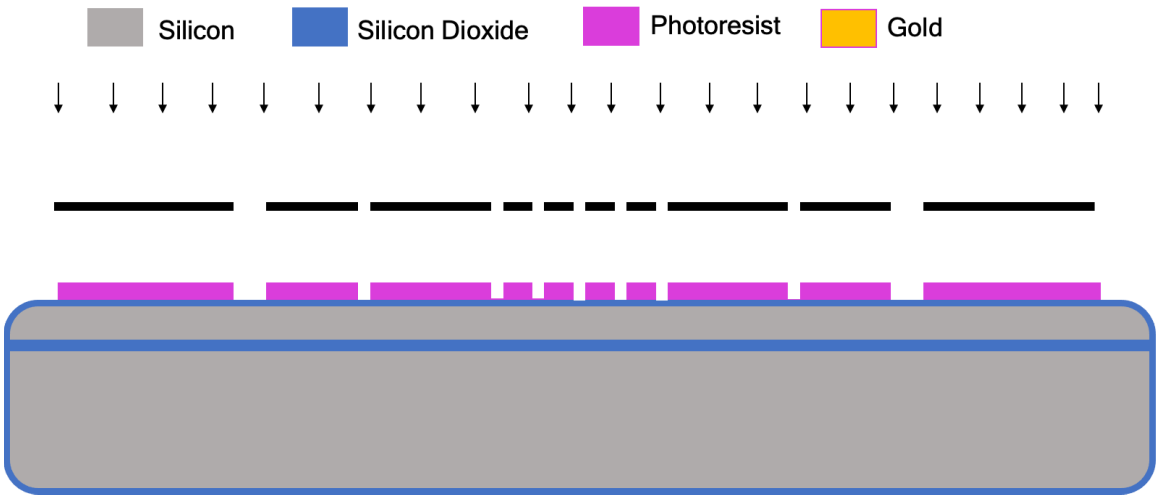

Figure 5-15 Photolithography step

Reactive Ion Etching (RIE) of Front Side

With the pattern set in the photoresist, the wafer then endures reactive ion etching (RIE). This anisotropic etching process utilizes chemically reactive plasma to remove material deposited on the wafer. The ions in the plasma are directed perpendicularly to the wafer's surface, resulting in high vertical etch rates. Given its precision, RIE ensures that structures are created with high fidelity to the initial pattern. This step has been done for 600 seconds to be sure that all the oxide has been removed.

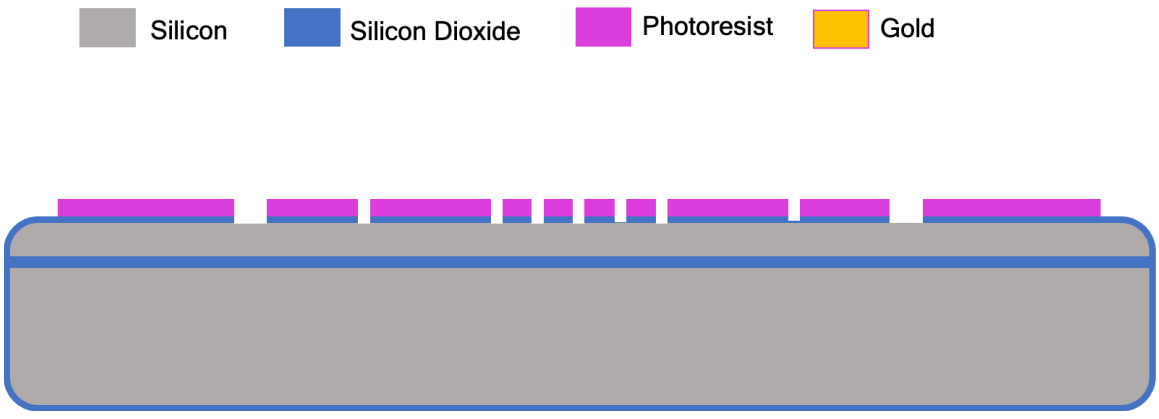

Figure 5-16 RIE of Oxide Mask

Back Side Photolithography and Deep Reactive Ion Etching (DRIE)

Mirroring the front-side process, the back side of the wafer undergoes photolithography to ensure patterns are established. DRIE then comes into play. DRIE exhibits high etch rates for silicon and allows for deep, high-aspect-ratio structures. Using alternating passivation and etching cycles, DRIE etches deeply but vertically, preventing lateral undercutting. We etched the handle layer until the buried oxide

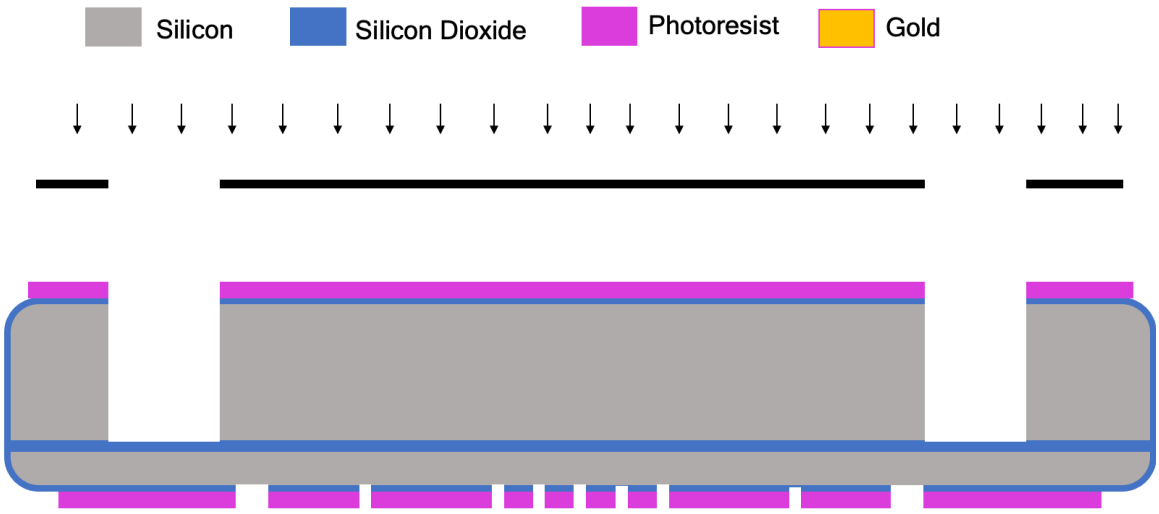

Figure 5-17 Backside lithography and DRIE of handle layer

Front Side DRIE Process

To fabricate the MEMS structures on the front side, the wafer is flipped and reloaded for another round of DRIE. This time, 100µm of the device layer is etched, carving out the microstructures that define the device's layout, resulting a Aspect Ratio of 50.

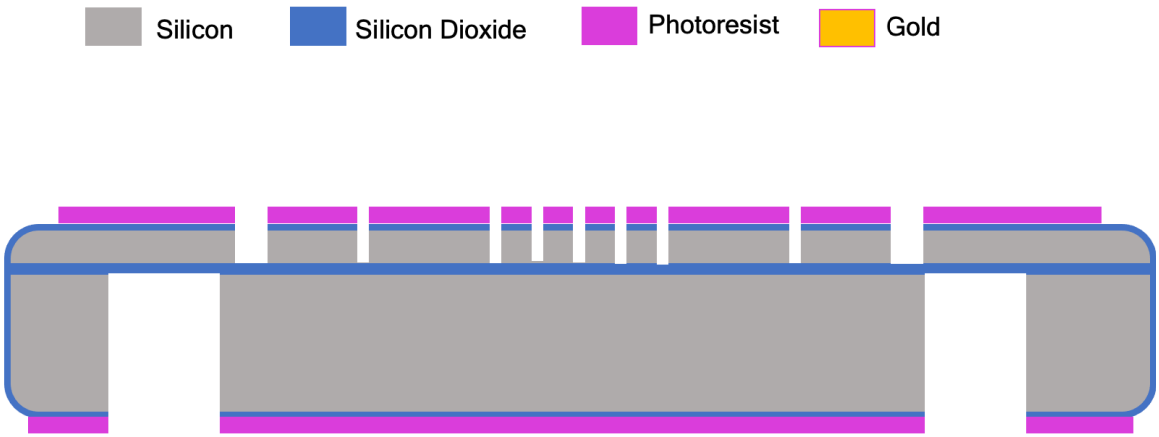

Figure 5-18 DRIE of Silicon on the device layer

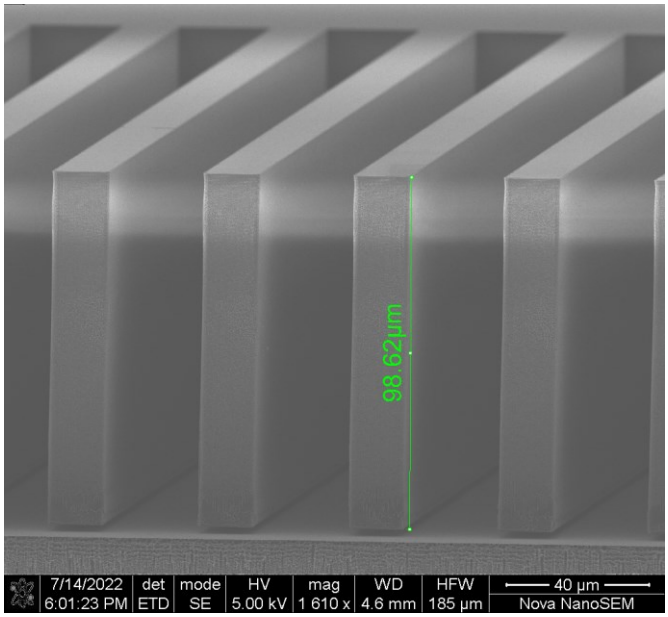

Figure 5-19 SEM of the cross-section for DRIE

Polymer Removal

During the passivation step in deep reactive ion etching (DRIE), a significant amount of polymer is deposited on the sidewalls within the trenches. To address this, a terminal treatment followed by a cleaning process is imperative. This thermal treatment is executed using a rapid thermal oven, which offers enhanced temperature control. This facilitates a gradual increase and decrease in temperature, ensuring the minimization of

additional stress within the structure. The temperature is raised to 700°C to ensure complete removal of the polymers. Subsequently, a cleaning step is employed using agents such as nano-strip or piranha. This step is crucial, as any residual polymers can compromise the final blanket coating of gold used for contacts, leading to potential shorts in the structures.

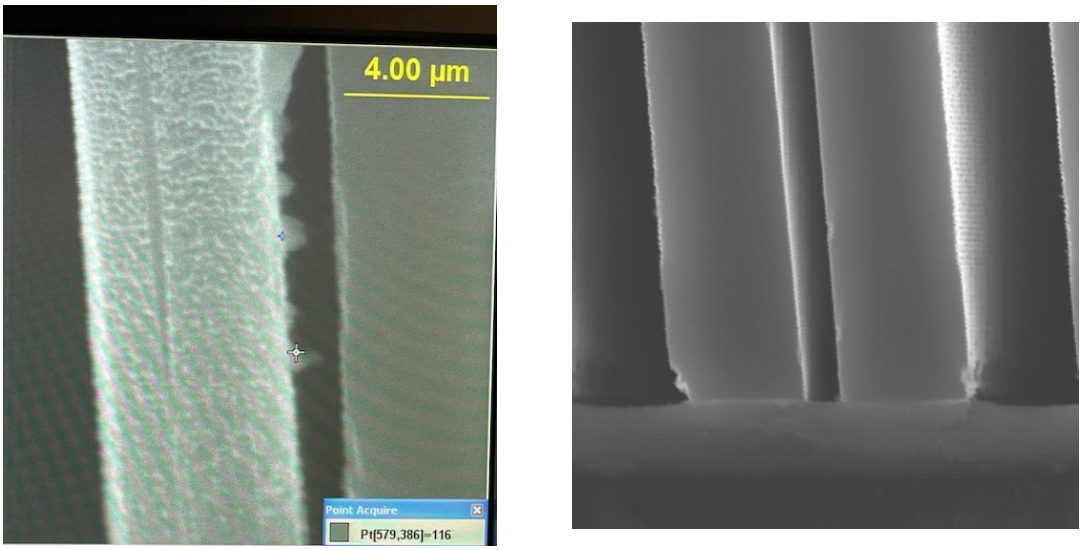

(a) (b)

Figure 5-20 (a) polymers inside the gas (b) removal of the polymers after heat treatment

Vapor HF Etching and Device Release

In the microfabrication of these devices, one of the concluding stages involves the release of the structures. This release process is executed using vapor HF. The structures are placed in a vapor HF chamber at 40°C for an hour to etch the buried oxide, as well as on the external surfaces of the structure. During a prior cleaning stage, the photoresist atop the structure is removed. As shown in previous figures, once the oxide is etched away, the device becomes detached from the wafer, leaving behind only a frame. This release stage essentially facilitates the dicing process. The motivation behind this approach is that conventional dicing can introduce significant contamination to the wafer.

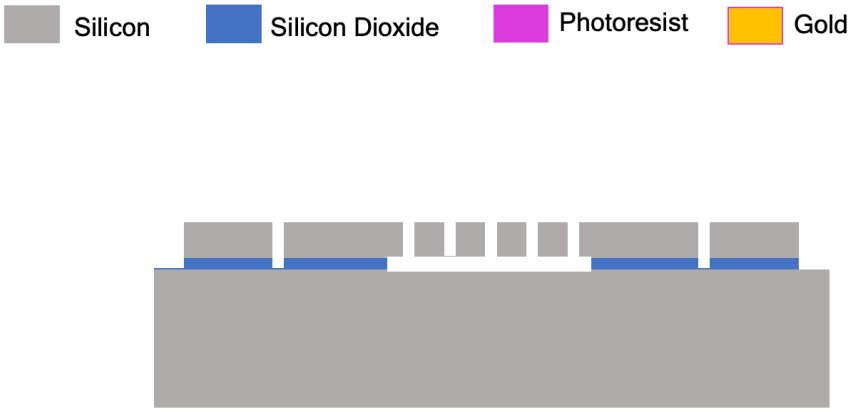

Figure 5-21 Schematic cross section of the devices after release

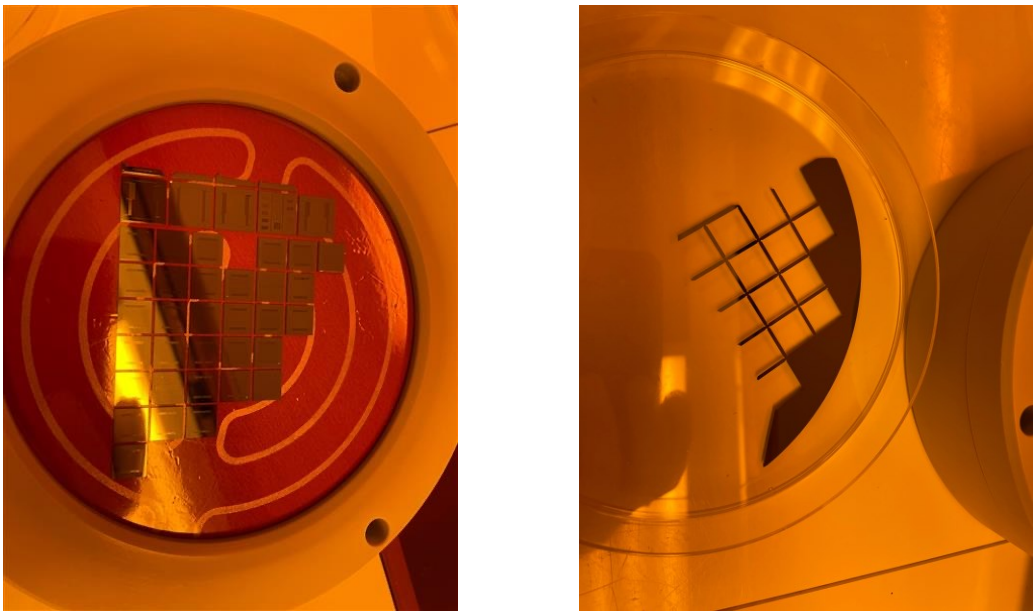

(a) (b)

Figure 5-22 (a) devices after release and separation on VHF chuck (b) the frame that detached from the devices.

Metallization

In the final phase of the microfabrication process, we deposit gold on the wafer using a blanket coating technique. This approach obviates the need for patterning the gold

on the wafer, thereby eliminating the requirement for an additional mask. Patterning gold on the wafer often necessitates processes such as lift-off, which occasionally lead to increased contamination. Furthermore, a significant limitation is that the DRIE tool in our clean room cannot be exposed to metals within its chamber. To use a mask for DRIE, a PECVD oxide deposition would be necessary. However, based on our experience, PECVD oxide is not effective due to its subpar quality, and it does not yield the desired aspect ratio. Thus, we adopt the blanket coating method, encompassing the entire wafer. The metallization comprised 20 nanometers of chromium and 200 nanometers of gold.

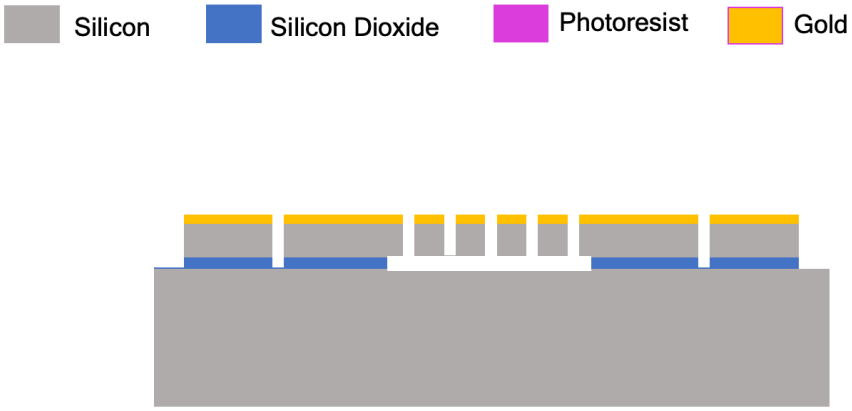

Figure 5-23 Schematic cross section of the devices after metallization

Packaging and Wire-bonding

Upon completion of the device fabrication, we employ LCC44 packages for packaging. Silver paste is utilized to affix the die to the package, which is then cured. Subsequently, the die is wire-bonded to the package to finalize the process.

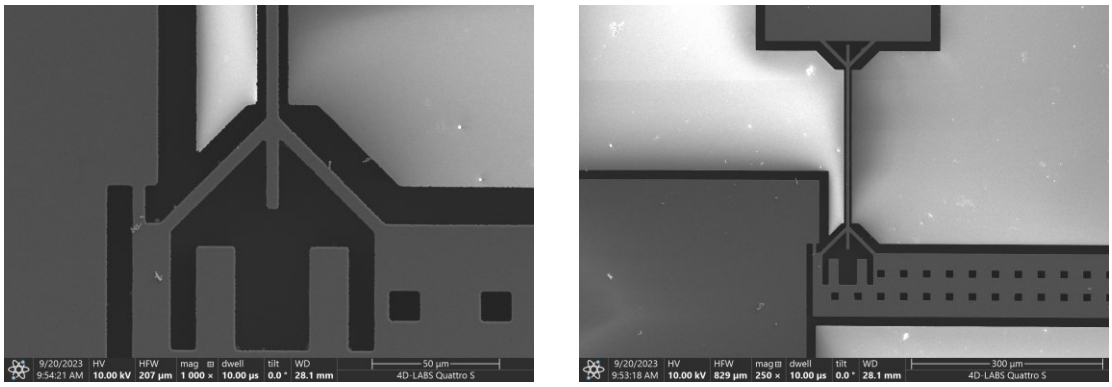

Figure 5-24 SEMs of the fabricated devices , here the Free Free beam with notched lever, Design "C". , the two extra beams within the notch are for prevention of over etching and/or grass formation during the DRIE step.

5.4. Experiments

Figure 5-25 presents a more detailed view of the design for Design “C-F-notch” resonator and lever, as an example, including the electric electrode configurations. The electrode configuration remains largely consistent across all the devices. As depicted in the figure, there are two electrodes positioned on the left and right sides of the resonant beam. The resonant beam itself is situated at the center. These electrodes serve the purpose of exciting the resonator at its resonance frequency. Additionally, there is an electrode located at the top directly connected to the resonant beam, which is used to apply a DC voltage. In the figure, this electrode is denoted by the letter "R". The excitation electrodes and the sensing electrodes are represented by "E1" and "E2" respectively. Furthermore, an additional electrode is positioned at the top of the other side of the lever to apply electrostatic force on the resonator. This electrode remains consistent across all the devices to ensure the same voltage difference and, subsequently, the same force is applied to all the devices. In the figure, this electrode is identified by the letter "F".

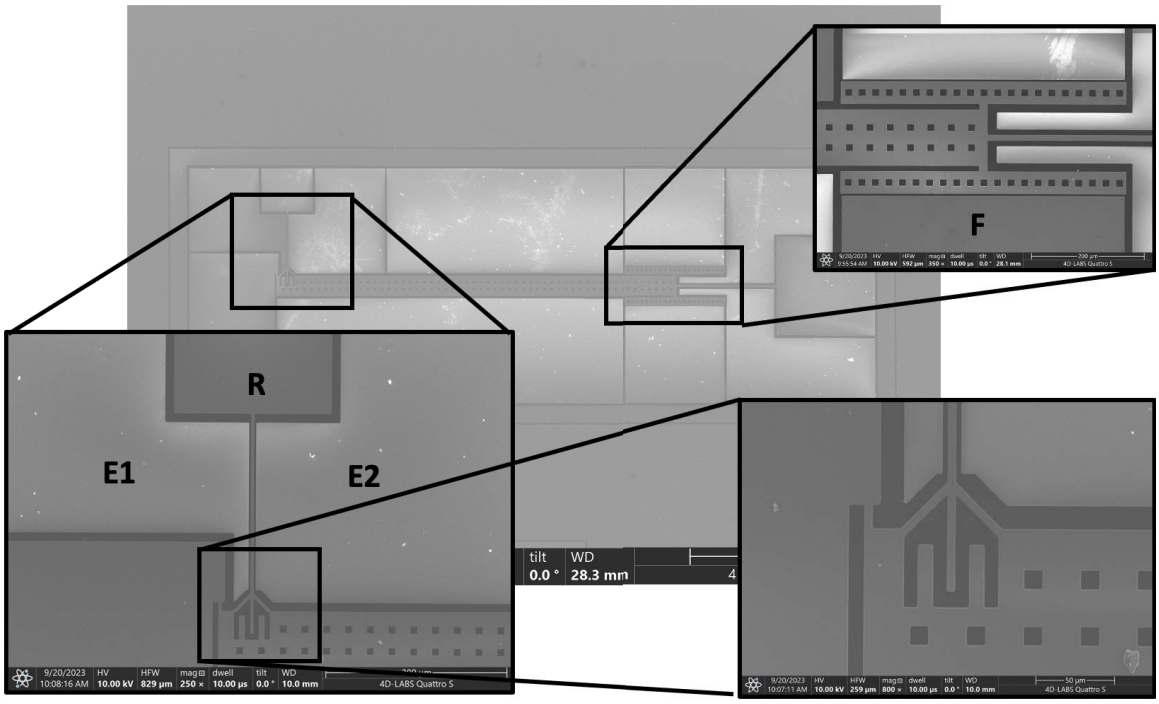

Figure 5-25 SEM images of the Design "D" along with details of the electrode configuration, the two extra beams within the notch are for prevention of over etching and/or grass formation during the DRIE step.

As we discussed the fabricated devices, each featuring a sizable electrode on top, as shown in Figure 5-26, for applying electrostatic force. These devices were positioned within a vacuum chamber, maintaining a vacuum level of approximately 20mTorr to increase the quality factor by removing the viscous damping. The devices' resonance frequency was determined using a lock-in amplifier and the synchronous demodulation method [104]. To negate any resonance shift caused by electrostatic voltages, all resonant beams were held at a consistent DC voltage during measurements. The resonance frequency of each beam was identified by applying the same AC voltage with the lock-in amplifier. Figure 5-26 shows the schematic of the experimental setup in which the bias voltage is shown as V, the DC bias applied to the resonators. The ΔV denotes the voltage applied to exert an electrostatic force on the lever.

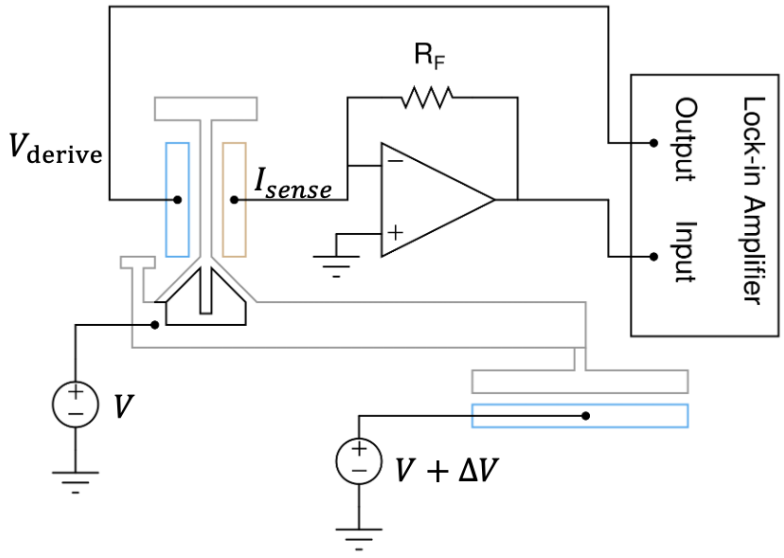

Figure 5-26 The schematic of the measurement setup for lever and resonant beam characterization using a lock-in amplifier, in the figure , the symbol V is for the Bias voltage

Figure 5-27 presents the measured data for the Clamped-Clamped resonant beam as an example, showing its resonance frequency without axial force as a symbol of measured resonance signals, similar measurements have been performed on other samples to measure the resonance frequencies and their quality factors.

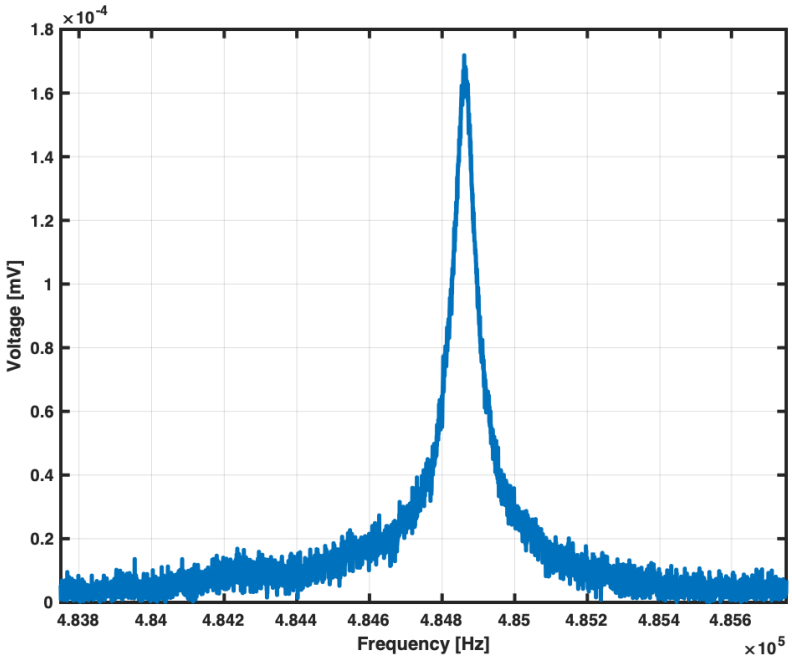

Figure 5-27 A measured resonance signal for a Free-Free beam

Following the measurement of the resonance frequency of the beam, the subsequent step involves increasing the voltage difference between the resonator and the electrode responsible for applying the electrostatic force. In this scenario, we manipulate the voltage levels between the electrodes, denoted as "F" and "R". We proceed to measure the resultant changes in resonance frequency for all the devices. For this analysis, we apply a voltage difference of $25\ volts$, which corresponds to a force of $17.5\ \mu N$ based on the dimensions of the electrode. Figure 5-28 presents the measurement results for the resonance frequency of the resonant beams, comparing the results for both with and without axial force. The "Clamped-Free" design, indicated as 'D', exhibits the highest sensitivity when subjected to the axial force applied across all structures. It should be noted that all devices share an identical electrode and are subjected to the same voltage, ensuring uniform force application. By measuring the shift in the resonance we can calculate the total sensitivity, Table 12 summarizes the results.

(a)

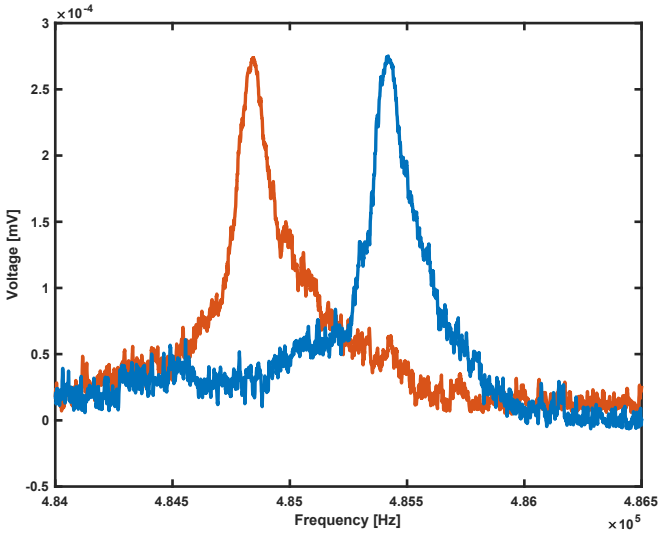
×10^-4
3
2.5
2
1.5
1
0.5
0
-0.5
Voltage [mV]
4.84
4.845
4.85
4.855
4.86
4.865
Frequency [Hz]
×10^5

(b)

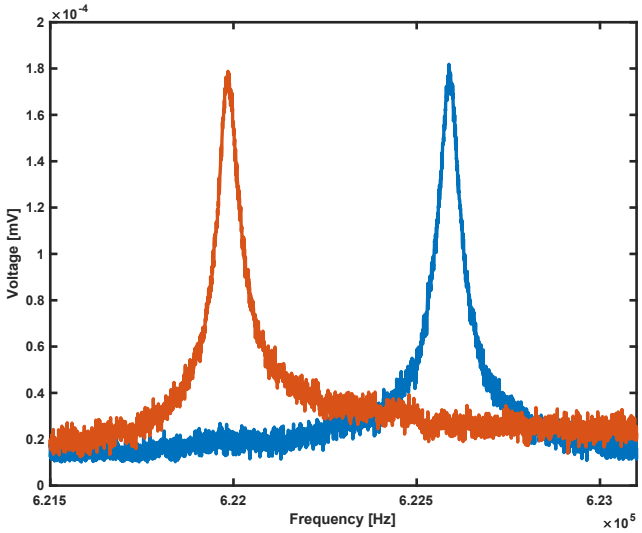
×10^-4
2
1.8
1.6
1.4
1.2
1
0.8
0.6
0.4
0.2
0
Voltage [mV]
6.215
6.22
6.225
6.23
Frequency [Hz]
×10^5

(c)

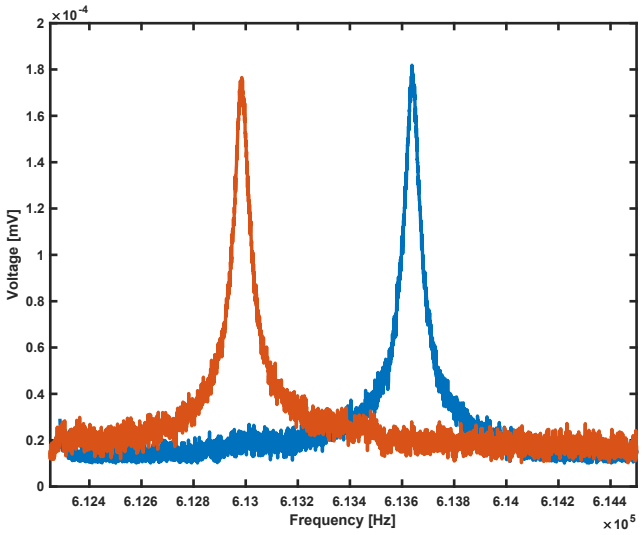

(d)

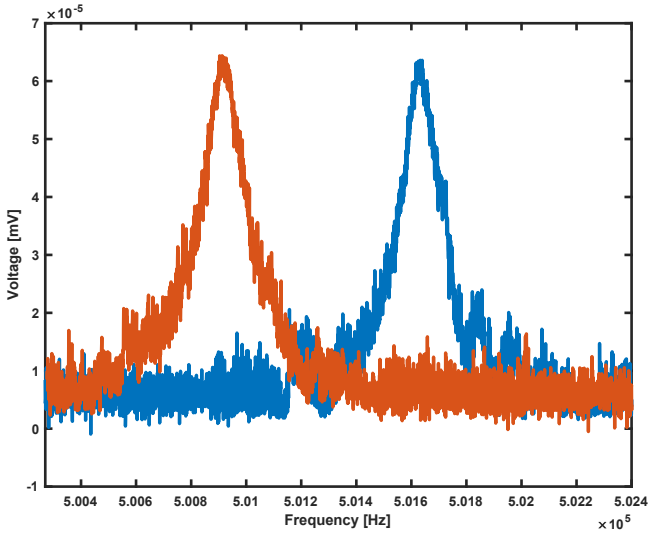

Figure 5-28 Measurement results of the resonance frequency for four different designs: (a) Design "A", (b) Design "B", (c) Design "C", and (d) Design "D". The results compare resonance frequencies in structures both without and with axial force. All designs are subjected to a consistent \(\Delta V \) of 25 volts, corresponding to a force of 17.5 micro-newtons.

Table 11 Summary and comparison of the measurement results for the designs introduced in this chapter

System	Resonance Frequency [in Hz]	Quality Factor	Sensitivity [in $Hz/\mu N$]
A	484846	6000	33
B	621981	11500	35
C	612845	12000	38
D	500910	9000	41

5.5. Summary

In this chapter, we delved into the study of levers and their role in mechanical amplifiers, emphasizing their contribution to enhancing sensitivity in resonance sensors. Our research also illuminated the impact of loading factors on these mechanical amplifiers. Taking this understanding further, we proposed innovative structures intended to surpass the traditionally employed levers, with the aim of improved sensitivity. we achieved a notable enhancement in sensitivity through the techniques and modifications presented in this chapter. We will reintegrate the designs of the lever and resonator with the proof mass, in the design and characterization of resonant accelerometers discussed in the next chapter.

Chapter 6. High-sensitivity resonant accelerometer

In Chapter 2, we introduced the structure of the resonant accelerometers, which is comprised of three primary components: a sensing resonant element, a mechanical amplifier, and a proof mass. These three components collectively form the backbone of the resonant accelerometer. In Chapter 3, we explored innovative sensing elements designed to enhance the sensitivity of these devices. Chapter 4 delved deeper into mechanical amplifiers, presenting novel structures aimed at enhancing the overall sensitivity. The designs were based on the integration of resonator and micro-lever structures with the aim of enhancing sensitivity.

In this current chapter, we integrate these novel structures with a proof mass to construct a resonant accelerometer. We have examined various design variations for the purpose of conducting a more comprehensive comparison. We will then compare the performances of these accelerometers, particularly assessing their sensitivity in acceleration measurements.

6.1. Design

In the design outline discussed, we will employ a differential configuration. The structure essentially consists of a proof mass with sensing elements positioned on both sides, aligned in the direction of the measurement axis. When subjected to acceleration, one side experiences a tensional force, leading to an increase in its resonance frequency, while the other side undergoes a compressive force, causing a decrease in its resonance frequency.

As we reviewed in Chapter 4, each lever measures 2040 micrometers. When integrating these two levers adjacently to structure the resonant accelerometer, the proof mass's width should approximately equal 4 millimeters. Furthermore, during the fabrication stage, we noted that each fabrication cell spans an area of 1 centimeter by 1

centimeter. To optimally utilize this available area, we conceptualized a design for the proof mass of these accelerometers. Figure 6--1 shows a schematic of a differential resonant accelerometer.

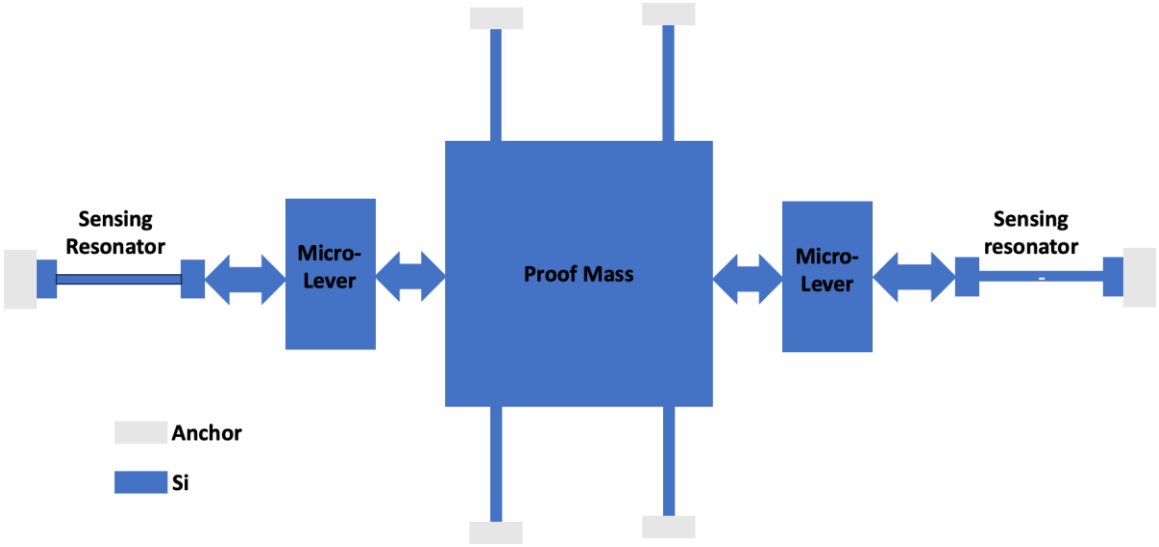

Figure 6-1 Schematic of diiferetial configuration for resonant accelerometer

In Chapter 4, we presented a novel resonant beam coupled with a micro-lever structure, aiming to achieve a highly sensitive resonant accelerometer. Drawing from our accumulated knowledge and experience in designing these structures, our accelerometer is conceptualized around a clamped-free beam, as detailed in Chapter 4, combined with the micro-lever structure containing an internal notch. Based on this design approach and our differential setup, the finalized design aligns closely with the schematic illustrated in Figure 6-2. Emphasizing symmetry in the design was crucial, especially given the use of differential sensing; the balance and uniformity in the design are of paramount importance. In our upcoming study focused on the design of these accelerometers, we will specifically examine the variations in the width of the notch within both the resonant beam and the micro-lever structure. Essentially, we will explore two distinct designs: one featuring a narrow notch and the other a wide notch. This investigation aims to discern the impact of the notch's width on the accelerometer's performance. In the subsequent subsection, we

will detail the dimensions for each design and present the results derived from our simulations.

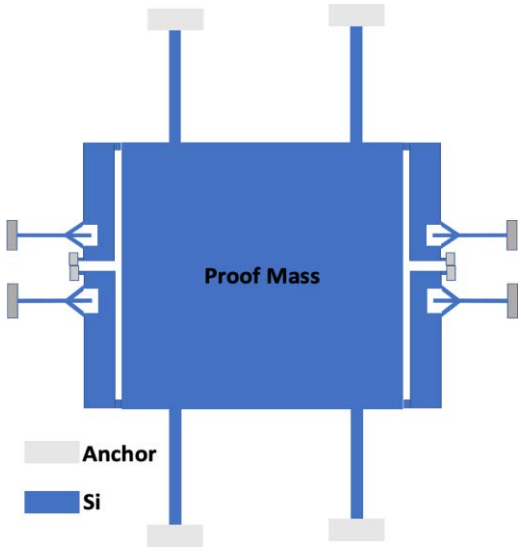

Figure 6-2 Schematic of an accelerometer with Clamped-Free beams and notched levers

6.2. Simulation

Based on the analyses presented in preceding chapters and the design considerations, we have opted to create an accelerometer using a clamped-free beam structure and the notched lever. The objective for the current section is to simulate this structure, determining its performance and dimensions that offer higher sensitivity. To facilitate a comparative study, we will also design a Clamped-Clamped Beam Resonator. This will allow for a direct performance comparison between the two types of resonant accelerometers.

Furthermore, we will explore the influence of notch dimensions on the sensor's performance. The simulation exercises for these accelerometers will employ CoventorWare software, using finite element analysis as the computational method. Specifically, we will conduct modal analyses on the 3D models both with and without

external acceleration. Subsequently, the entire structure will be subjected to a 1g force to simulate and calculate shifts in resonance frequency and to determine sensitivity in terms Hz/g. The table 13 summarizes the dimensions used in these simulations, along with the resulting data for these accelerometers.

Table 12 Summary of the dimensions and simulation results for three types of accelerometers, a Clamped-Clamped beam with regular lever, and two Clamped-Free beams with notched levers while the notch dimensions are different.

Device		Accelerometer 1	Accelerometer 2	Accelerometer 3
Resonator type		C-C	C-F	C-F
Lever type		regular	notched	notched
Proof mass size		0.005 gram		
Dimensions	Resonator beam	length=300 width=5	length=324 width=5	length=324 width=5
	Boundary beam	NA	Length=71 width=5	length=91 width=5
	Lever beam	length=2040 width=100		
	Notch	NA	length=60 depth=50	length=80 depth=50
Simulations	resonance frequency $[Hz]$	485159	473060	500082
	sensitivity $[Hz/g]$	274	294	330

As indicated in the preceding table, we have examined three different accelerometers. The first accelerometer employs a clamped-clamped beam design, while the second and third utilize a baseline clamped-free beam. All three accelerometers are coupled to an identical proof mass with a mass of 5 milligrams. The dimensions of the beams differ slightly, which is an intentional adjustment made in accordance with discussions in Chapter 3. We have adjusted the beam dimensions so that the resonance

frequencies of all three beams fall within the same range. This enables not only the comparison of absolute sensor sensitivities but also the evaluation of relative sensitivities within these structures.

Regarding boundary beam considerations, it can be observed that the notch size is narrower in accelerometers two and three, accounting for the shorter length of the boundary beam in the second accelerometer compared to the third. Figure 6-3 depicts the 3D models of the accelerometers used for sensitivity analysis. As the shapes of the resonators have already been introduced in a previous chapter, we will not revisit those structures here. Instead, we focus on presenting the 3D model that provide further detail on these devices.

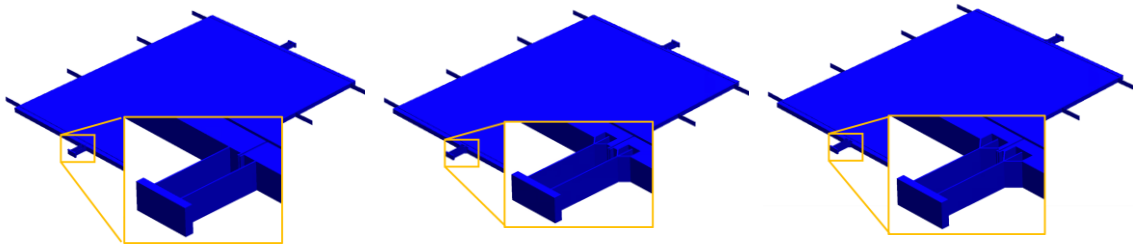

(a) (b) (c)

Figure 6-3 3D Model of the simulated accelerometers (a) Accelerometer 1 described in Table 13, (b) Accelerometer 2 described in Table 13 and (c) Accelerometer 3 described in Table 13

Based on the simulation results, it is evident that Accelerometer 3 exhibits the highest performance among the accelerometers examined. There is an increase in sensitivity of over 20% when transitioning from a simple clamped-clamped beam to a clamped-free beam with a notched lever. Additionally, it was observed that a narrower notch results in decreased sensitivity within this structure. Therefore, in this design, the presence of the gap appears to contribute to higher sensitivity, at least within the dimensions studied. This presents an intriguing topic for future research. In the next phase, we have drafted the layout based on this accelerometer design and proceeded with fabrication. The following section provides a summary of the fabrication process.

6.3. Fabrication

A mask layout was designed for all accelerometers as described in the previous section. Figure 6-4 specifically illustrates the layout for Accelerometer #3. The same proof mass and layout were employed for the other two accelerometers; the distinguishing features lie in the dimensions of the notch and the resonant beam, which are detailed for Accelerometer #3. This layout was generated using CoventorWare layout software. Following the design phase, masks were produced and subsequently utilized in the lithography and fabrication processes, which will be elaborated upon.

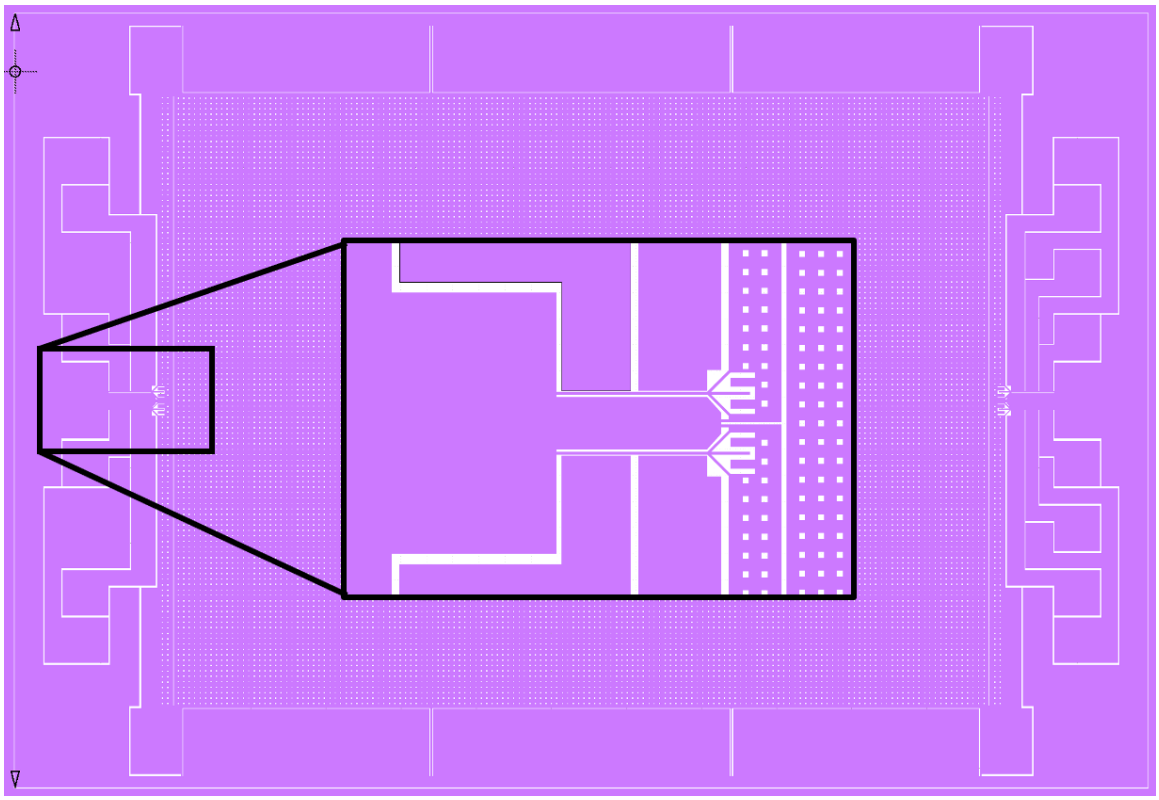

Figure 6-4 Drawn layout for accelerometer #3

The fabrication process is the same as the one was discussed in chapter 4, here we just give the summary of the fabrication process. An optimized microfabrication process flow, utilizing deep reactive ion etching (DRIE), was developed and executed to

produce MEMS structures, incorporating crucial components like suspension beams, proof mass, and electrical comb structures.

Figure 6-5 presents a composite of scanning electron microscope (SEM) images of the fabricated accelerometers. Based on our measurements, some structural elements appear thinner than initially designed. Consequently, we anticipate that the final performance of these accelerometers may exhibit higher sensitivity than that suggested by simulation results.

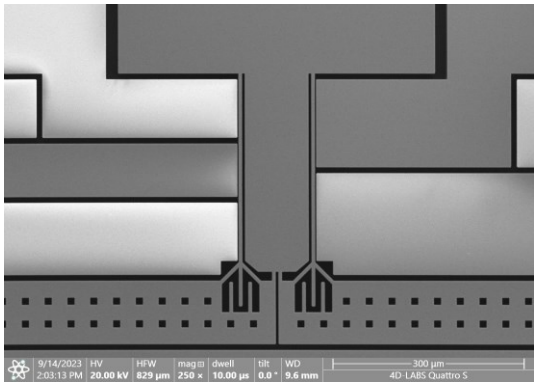

(a)

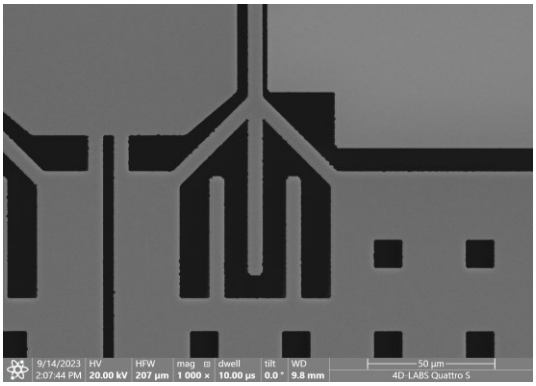

(b)

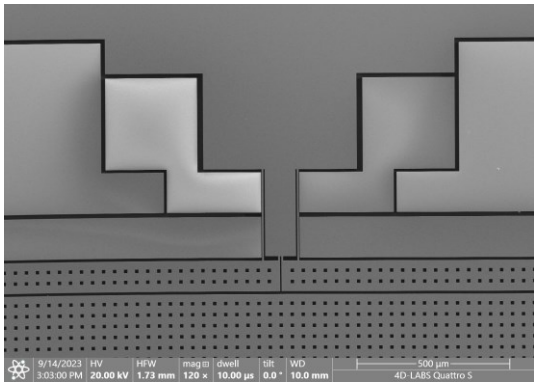

(c)

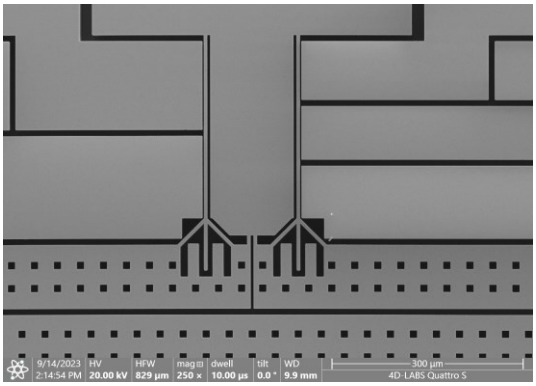

(d)

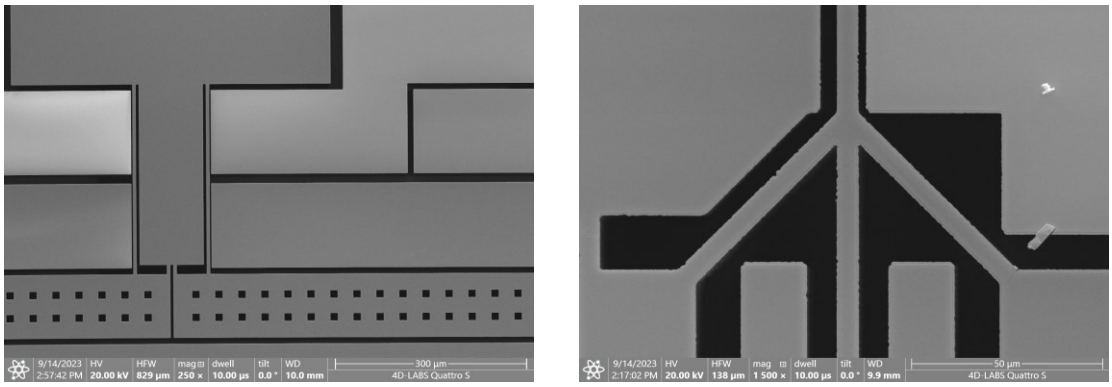

(e) (f)

Figure 6-5 SEM images of the fabricated accelerometers

6.4. Experiments

Utilizing the fabrication process delineated in prior sections, we constructed the accelerometers detailed in Table 13 and subsequently tested them. This section will present the findings from these tests.

To evaluate the sensitivity of these accelerometers, each was positioned on a tilting stage situated within a vacuum chamber maintained at approximately 20 mTorr. As illustrated in Figure 6-6, when the accelerometers rotate along the sensitive axis to an angle of 90 degrees, they undergo a 1g acceleration. Consequently, the bottom two resonators experience a compressive force, leading to a decrease in their resonance frequency. In contrast, the top two resonators undergo a tensile force, resulting in an increase in their resonance frequency. We measure the resonance frequency of these accelerometers using an approach similar to the one described in the previous section using a lock-in amplifier. Upon applying these forces, Figure 6-7 visually represents the experimental setup. The measurement setup employed here to measure the resonance frequency of the resonators is identical to the one detailed in Chapters 3 and 4. As such, we will not revisit the discussion of the measurement methodologies here.

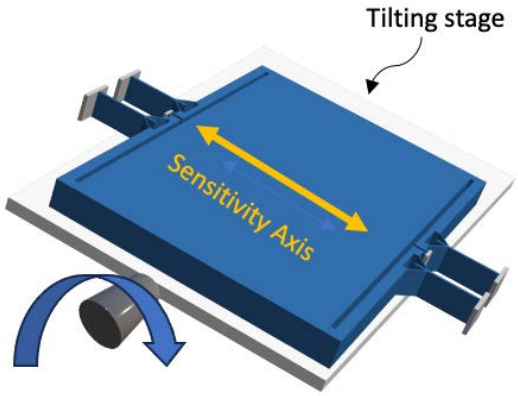

Figure 6-6 Schematic of the measurement detup for characterization of resonant accelerometers

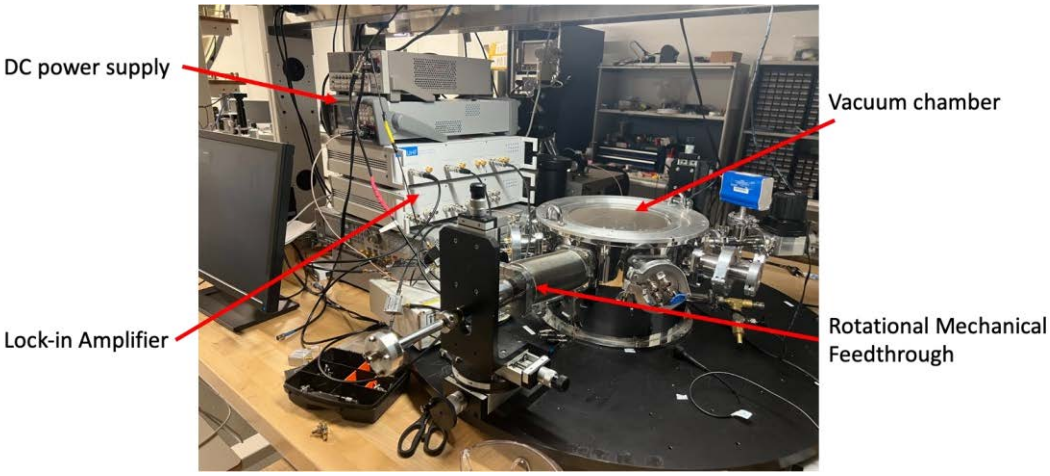

Figure 6-7 Image of the measurement setup

Figure 6-8 illustrates the shift in resonance for each accelerometer relative to the tilting stage angle. Evidently, as the accelerometers rotate within gravity's influence, their data seems to trace a sine wave pattern. Among the devices tested, Accelerometer 3, designed with a clamp-free beam, demonstrated approximately a 30% increase in sensitivity compared to the clamped-clamped design. This corroborates our earlier observations, where clamp-free beams typically exhibited a higher quality factor. This attribute implies that resonance shifts in such designs are more readily discernible due to their enhanced quality factor.

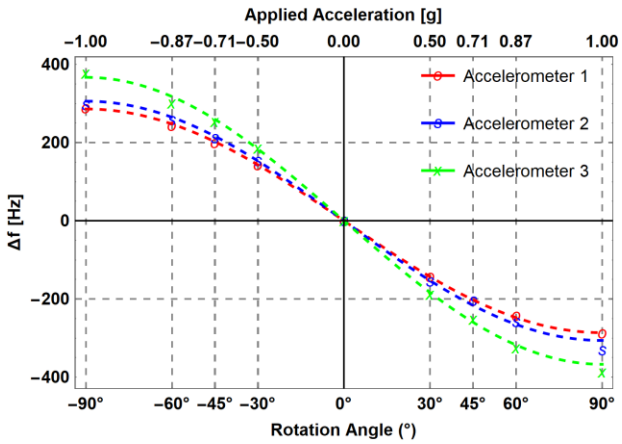

Figure 6-8 the measured shift in the resonance frequencies while the accelerometers were rotated against the gravity.

The design and fabrication of an accelerometer demand an in-depth analysis of its fundamental characteristics to evaluate its performance. Three of the most critical features of any accelerometer include its dynamic range, linearity, and noise floor. The measurements and estimations provided in this discussion are based on the theoretical design and have not been practically evaluated. Thus, while they offer valuable insights, these should be taken as preliminary estimations, pending empirical validation.

Dynamic Range

The dynamic range of an accelerometer is defined as the ratio between the maximum and minimum measurable acceleration values. In simpler terms, it gives an idea of how well the accelerometer can detect both very large and very small acceleration magnitudes. A higher dynamic range indicates the ability of the accelerometer to detect finer changes in acceleration without saturation or loss of data.

$$DR = Maximum\ measurable\ acceleration / Minimum\ measurable\ acceleration$$

For our accelerometer, a critical component to consider is its resonance frequency, which is approximately 3 kHz. This frequency is achieved through the use of a proof glass and older springs surrounding the proof mass. This design ensures that the accelerometer, when subjected to external forces, will exhibit a displacement of about 20nm per G. Given

the physical constraints of the accelerometer's structure, there is a confined space of $2\ \mu m$ in which the accelerometer can move within its frame. This constraint defines the upper limit of the accelerometer's measurement capability, allowing it to measure up to a theoretical maximum of 10 G.

On the lower end of the spectrum, the accelerometer's noise floor—the minimum detectable signal—is primarily determined by its inherent acceleration noise. In other words, it is the threshold below which the accelerometer can't distinguish between actual movement and its internal electronic noise. Referring to the formulas detailed in Chapter 2, the noise floor can be estimated considering various factors such as the dimensions, size of the proof mass, and other structural elements. This calculated noise floor, $0.7\ g/\sqrt{Hz}$, denotes the accelerometer's lower measurement limit. By juxtaposing this lower limit with the aforementioned upper limit, we can derive an estimation for the accelerometer's dynamic range, providing a comprehensive view of its potential measurement capabilities.

Linearity

Linearity is a measure of how well the output of the accelerometer corresponds to its input across its entire operational range. A perfectly linear device would have an output directly proportional to its input, with no deviation. Any deviation from this ideal proportionality denotes non-linearity. Based on the design specifications, when forces are applied to the accelerometer, the resulting reaction will be chiefly within the confines of the 10 G dynamic range. The response of the system remains highly linear, as substantiated by the detailed calculations presented in Chapters 3 and 4.

Estimating the dynamic range, linearity, and noise floor of an accelerometer is paramount to gauge its potential performance in practical applications. These values, derived from theoretical designs and calculations, provide preliminary insights into how the accelerometer might behave. However, to attain a definitive understanding and potentially improve these estimations, empirical tests are indispensable. As our accelerometer moves from the design phase to the implementation phase, these estimations will serve as foundational metrics, guiding calibration, testing, and eventual deployment.

6.5. Summary

In this chapter, we have designed, simulated, fabricated, and tested 3 types of resonant accelerometers, each with unique structural components as outlined in previous chapters. Utilizing a clamped-free beam structure and a notched lever, the designs aim to enhance accelerometer sensitivity. We employed finite element analysis using CoventorWare software for simulation, focusing on the influence of notch dimensions on sensor performance. In fabrication, standardized masks were used for lithography, incorporating features like the proof mass and resonant beams. Subsequent tests, carried out in a vacuum chamber, confirmed that Accelerometer 3, built with a clamped-free beam, showed approximately a 30% increase in sensitivity compared to its clamped-clamped counterpart. The testing phase also revealed that some fabricated structures were thinner than initially designed, suggesting the potential for even higher sensitivities. These findings offer valuable insights for future research in resonant accelerometer design.

Chapter 7. Conclusions and future work

7.1. Contributions

The research has contributed significantly to the field of resonant beam force sensors and accelerometers by introducing ground-breaking design modifications aimed at enhancing sensitivity. Specifically, the study has broken new ground by developing innovative sensor designs that depart from the conventional clamped-clamped beam structures. These novel designs use different boundary conditions, resulting in improvement in performance. Analytical and numerical models affirm that these new designs achieve an impressive four-fold increase in sensor sensitivity, a quantum leap over existing configurations.

One of the most practical aspects of these design innovations is that they are fully compatible with existing fabrication techniques and material specifications. This means that these advancements can be directly integrated into current sensor systems without the need for any disruptive or costly changes. This feature ensures the practical and immediate applicability of the research, allowing for swift performance improvements in existing sensor technologies.

In addition to sensor design, the research explored the vital role of mechanical amplifiers in improving the performance of these sensors. The study moved beyond traditional lever structures by proposing novel mechanisms that substantially increase sensor sensitivity. Furthermore, the study provided insights into the effects of various loading factors on mechanical amplifiers.

Applying these design novelties to the specialized realm of resonant accelerometers yielded promising results. Utilizing a clamped-free beam structure in tandem with a notched lever, the new accelerometer designs were tested. Finite element analysis was employed for simulation, focusing on the role of notch dimensions in affecting overall sensor performance. The simulations led to the actual fabrication and subsequent testing of these accelerometer designs, conducted under controlled conditions in a

vacuum chamber. The results showed that accelerometers designed with these novel features exhibited significant enhancements in sensitivity. Specifically, the use of a clamped-free beam led to approximately a 30% increase in sensitivity compared to traditional clamped-clamped beam designs.

In summary, the research has achieved remarkable advancements in the design of resonant force sensors and accelerometers. Through intelligent design alterations, coupled with meticulous simulation and testing, the study offers not only immediate improvements for current systems but also a rich foundation for future research aimed at pushing the boundaries of sensor sensitivity and performance.

7.2. Future work

In this research, we introduced innovative structures to enhance the sensitivity of resonant accelerometers. Several avenues for further study and potential improvements are evident from this work.

First, while the research altered the boundary conditions of the beams to elevate sensor sensitivity, the models employed were simplified and relied on classical conditions such as free-free and clamped-clamped beams. Given that additional elements were incorporated into the beam structure, these conditions may not accurately reflect the true state of the system. Consequently, future research should account for beam stiffness and dimensions in characterizing the system and optimizing sensor sensitivity.

Second, examining the nonlinearities within these new structures could yield valuable insights. The nonlinear behavior of these resonators will differ from traditional clamped-clamped beams due to their unique deflection shapes, providing another fruitful area for investigation.

Third, the temperature-dependent behavior of these accelerometers remains unexplored and warrants study. Understanding how temperature variations affect sensor performance could be instrumental for broader applications.

Fourth, our simulations presumed the lever as a rigid body without accounting for bending within its structure. Developing models that incorporate the mechanical behavior of the lever, especially under applied forces, would offer a more nuanced understanding of the system's performance.

Lastly, the noise performance in these novel structures merits examination. Given that the design innovations introduced here result in a higher quality factor, analyzing phase noise and the signal-to-noise ratio could contribute to the refinement of these systems.

These suggested areas for subsequent research not only aim to deepen our understanding of the introduced structures but also strive to optimize their performance and applicability.

References

[1] S. D. Senturia, *Microsystem design*. Boston: Kluwer Academic Publishers, 2001.

[2] G. Lammel, “The future of MEMS sensors in our connected world,” *Proceedings of the IEEE International Conference on Micro Electro Mechanical Systems (MEMS)*, vol. 2015-Febru, no. February, pp. 61–64, 2015, doi: 10.1109/MEMSYS.2015.7050886.

[3] “Accelerometer Market: Global Industry Analysis and forecast (2023-2029),” MAXIMIZE MARKET RESEARCH. Accessed: Sep. 02, 2023. [Online]. Available: https://www.maximizemarketresearch.com/market-report/global-accelerometer-market/35621/

[4] “IEEE Standard for Inertial Sensor Terminology,” *IEEE Std 528-2001*, pp. 1–26, Nov. 2001, doi: 10.1109/IEEESTD.2001.93360.

[5] F. W. Lanchester, “The pendulum accelerometer, an instrument for the direct measurement and recording of acceleration,” *The London, Edinburgh, and Dublin Philosophical Magazine and Journal of Science*, vol. 10, no. 56, pp. 260–268, Aug. 1905, doi: 10.1080/14786440509463370.

[6] L. M. Roylance and J. B. Angell, “A batch-fabricated silicon accelerometer,” *IEEE Transactions on Electron Devices*, vol. 26, no. 12, pp. 1911–1917, Dec. 1979, doi: 10.1109/T-ED.1979.19795.

[7] Lj. Ristic, R. Gutteridge, B. Dunn, D. Mietus, and P. Bennett, “Surface micromachined polysilicon accelerometer,” in *Technical Digest IEEE Solid-State Sensor and Actuator Workshop*, Jun. 1992, pp. 118–121. doi: 10.1109/SOLSEN.1992.228311.

[8] P.-L. Chen *et al.*, “Integrated silicon microbeam PI-FET accelerometer,” *IEEE Transactions on Electron Devices*, vol. 29, no. 1, pp. 27–33, Jan. 1982, doi: 10.1109/T-ED.1982.20654.

[9] J. Marty, A. Malki, C. Renouf, P. Lecoy, and F. Baillieu, “Fibre-optic accelerometer using silicon micromachining techniques,” *Sensors and Actuators A: Physical*, vol. 47, no. 1, pp. 470–473, Mar. 1995, doi: 10.1016/0924-4247(94)00943-C.

[10] R. Hiratsuka, D. C. van Duyn, T. Otaredian, and P. de Vries, “A novel accelerometer based on a silicon thermopile,” in *TRANSDUCERS ’91: 1991 International Conference on Solid-State Sensors and Actuators. Digest of Technical Papers*, Jun. 1991, pp. 420–423. doi: 10.1109/SENSOR.1991.148901.

[11] S. B. Waltman and W. J. Kaiser, “An electron tunneling sensor,” *Sensors and Actuators*, vol. 19, no. 3, pp. 201–210, Sep. 1989, doi: 10.1016/0250-6874(89)87073-8.

[12] A. Kourepenis, A. Petrovich, and M. Weinberg, “Low cost quartz resonant accelerometer for aircraft inertial navigation,” in *TRANSDUCERS ’91: 1991 International Conference on Solid-State Sensors and Actuators. Digest of Technical Papers*, Jun. 1991, pp. 551–553. doi: 10.1109/SENSOR.1991.148935.

[13] M. Helsel, G. Gassner, M. Robinson, and J. Woodruff, “A navigation grade micro-machined silicon accelerometer,” in *Proceedings of 1994 IEEE Position, Location and Navigation Symposium - PLANS’94*, Apr. 1994, pp. 51–58. doi: 10.1109/PLANS.1994.303295.

[14]A. Perunnilathil Joy, M. Kanygin, and B. Bahreyni, “A Piezo-Avalanche Accelerometer,” *Journal of Microelectromechanical Systems*, vol. 29, no. 2, pp. 144–147, Apr. 2020, doi: 10.1109/JMEMS.2020.2968069.
[15]F. Edalatfar, “Design and Fabrication of High-Performance Capacitive Micro Accelerometers”.
[16]T. B. Gabrielson, “Mechanical-thermal noise in micromachined acoustic and vibration sensors,” *IEEE Transactions on Electron Devices*, vol. 40, no. 5, pp. 903–909, May 1993, doi: 10.1109/16.210197.
[17]F. Edalafar *et al.*, “A Wideband, Low-Noise Accelerometer for Sonar Wave Detection,” *IEEE Sensors Journal*, vol. 18, no. 2, pp. 508–516, Jan. 2018, doi: 10.1109/JSEN.2017.2774705.
[18]C. Wang *et al.*, “Micromachined Accelerometers with Sub-μg/√Hz Noise Floor: A Review,” *Sensors*, vol. 20, no. 14, Art. no. 14, Jan. 2020, doi: 10.3390/s20144054.
[19]B. Bahreyni, *Fabrication and design of resonant microdevices*. in Micro & nano technologies, no. 3. Norwich, NY: W. Andrew Inc, 2008.
[20]N. Yazdi and K. Najafi, “An all-silicon single-wafer micro-g accelerometer with a combined surface and bulk micromachining process,” *Journal of Microelectromechanical Systems*, vol. 9, no. 4, pp. 544–550, Dec. 2000, doi: 10.1109/84.896777.
[21]C.-H. Liu and T. W. Kenny, “A high-precision, wide-bandwidth micromachined tunneling accelerometer,” *Journal of microelectromechanical systems*, vol. 10, no. 3, pp. 425–433, 2001.
[22]N. C. Loh, M. A. Schmidt, and S. R. Manalis, “Sub-10 cm/sup 3/ interferometric accelerometer with nano-g resolution,” *Journal of Microelectromechanical Systems*, vol. 11, no. 3, pp. 182–187, Jun. 2002, doi: 10.1109/JMEMS.2002.1007396.
[23]R. Abdolvand, B. Vakili Amini, and F. Ayazi, “Sub-Micro-Gravity In-Plane Accelerometers With Reduced Capacitive Gaps and Extra Seismic Mass,” *Journal of Microelectromechanical Systems*, vol. 16, no. 5, pp. 1036–1043, Oct. 2007, doi: 10.1109/JMEMS.2007.900879.
[24]U. Krishnamoorthy *et al.*, “In-plane MEMS-based nano-g accelerometer with sub-wavelength optical resonant sensor,” *Sensors and Actuators A: Physical*, vol. 145–146, pp. 283–290, 2008, doi: https://doi.org/10.1016/j.sna.2008.03.017.
[25]L. Aaltonen, P. Rahikkala, M. Saukoski, and K. Halonen, “High-resolution continuous-time interface for micromachined capacitive accelerometer,” *International Journal of Circuit Theory and Applications*, vol. 37, no. 2, pp. 333–349, 2009, doi: 10.1002/cta.547.
[26]Xudong Zou, P. Thiruvenkatanathan, and A. A. Seshia, “A Seismic-Grade Resonant MEMS Accelerometer,” *J. Microelectromech. Syst.*, vol. 23, no. 4, pp. 768–770, Aug. 2014, doi: 10.1109/JMEMS.2014.2319196.
[27]H. Xu, X. Liu, and L. Yin, “A Closed-Loop $\Sigma\Delta$ Interface for a High-Q Micromechanical Capacitive Accelerometer With 200 ng/$ \surd$Hz Input Noise Density,” *IEEE Journal of Solid-State Circuits*, vol. 50, no. 9, pp. 2101–2112, Sep. 2015, doi: 10.1109/JSSC.2015.2428278.
[28]P. J. Kamp, “Towards an Ultra Sensitive Seismic Accelerometer.” Accessed: Apr. 08, 2023. [Online]. Available: http://essay.utwente.nl/69298/
[29]Y. Bao *et al.*, “An optomechanical accelerometer with a high-finesse hemispherical optical cavity,” in *2016 IEEE International Symposium on Inertial Sensors and Systems*, Feb. 2016, pp. 105–108. doi: 10.1109/ISISS.2016.7435556.

[30]J. G. Flor Flores *et al.*, “A CMOS-compatible oscillation-mode optomechanical DC accelerometer at 730-ng/Hz1/2 resolution,” in *2016 IEEE International Symposium on Inertial Sensors and Systems*, Feb. 2016, pp. 125–127. doi: 10.1109/ISISS.2016.7435563.
[31]W. T. Pike *et al.*, “A Silicon Seismic Package (SSP) for Planetary Geophysics,” p. 2081, Mar. 2016.
[32]D. D. Shin, C. H. Ahn, Y. Chen, D. L. Christensen, I. B. Flader, and T. W. Kenny, “Environmentally robust differential resonant accelerometer in a wafer-scale encapsulation process,” in *2017 IEEE 30th International Conference on Micro Electro Mechanical Systems (MEMS)*, Jan. 2017, pp. 17–20. doi: 10.1109/MEMSYS.2017.7863328.
[33]Q. Lu, J. Bai, K. Wang, and S. He, “Design, Optimization, and Realization of a High-Performance MOEMS Accelerometer From a Double-Device-Layer SOI Wafer,” *Journal of Microelectromechanical Systems*, vol. 26, no. 4, pp. 859–869, Aug. 2017, doi: 10.1109/JMEMS.2017.2693341.
[34]Y. Yin, Z. Fang, F. Han, B. Yan, J. Dong, and Q. Wu, “Design and test of a micromachined resonant accelerometer with high scale factor and low noise,” *Sensors and Actuators A: Physical*, vol. 268, pp. 52–60, 2017, doi: https://doi.org/10.1016/j.sna.2017.10.043.
[35]A. Fougerat and L. Guerineau, “Ultra-low-noise MEMS accelerometer for Seismology,” p. 7188, Apr. 2018.
[36]Y. Duo *et al.*, “Self-suppression of common-mode noises of the different fiber optic interferometric accelerometers,” *Opt. Express, OE*, vol. 26, no. 12, pp. 15384–15397, Jun. 2018, doi: 10.1364/OE.26.015384.
[37]A. Utz, C. Walk, A. Stanitzki, M. Mokhtari, M. Kraft, and R. Kokozinski, “A High-Precision and High-Bandwidth MEMS-Based Capacitive Accelerometer,” *IEEE Sensors Journal*, vol. 18, no. 16, pp. 6533–6539, Aug. 2018, doi: 10.1109/JSEN.2018.2849873.
[38]W. Wu, J. Liu, J. Fan, D. Peng, H. Liu, and L. Tu, “A nano-g micromachined seismic sensor for levelling-free measurements,” *Sensors and Actuators A: Physical*, vol. 280, pp. 238–244, Sep. 2018, doi: 10.1016/j.sna.2018.07.050.
[39]A. Prasad *et al.*, “A Portable MEMS Gravimeter for the Detection of the Earth Tides,” in *2018 IEEE SENSORS*, Oct. 2018, pp. 1–3. doi: 10.1109/ICSENS.2018.8589884.
[40]M. Pandit *et al.*, “An Ultra-High Resolution Resonant MEMS Accelerometer,” in *2019 IEEE 32nd International Conference on Micro Electro Mechanical Systems (MEMS)*, Jan. 2019, pp. 664–667. doi: 10.1109/MEMSYS.2019.8870734.
[41]Y. Kamada, A. Isobe, T. Oshima, Y. Furubayashi, T. Ido, and T. Sekiguchi, “Capacitive MEMS Accelerometer With Perforated and Electrically Separated Mass Structure for Low Noise and Low Power,” *Journal of Microelectromechanical Systems*, vol. 28, no. 3, pp. 401–408, Jun. 2019, doi: 10.1109/JMEMS.2019.2903349.
[42]C. Zhao *et al.*, “A Resonant MEMS Accelerometer With 56ng Bias Stability and 98ng/Hz1/2 Noise Floor,” *Journal of Microelectromechanical Systems*, vol. 28, no. 3, pp. 324–326, Jun. 2019, doi: 10.1109/JMEMS.2019.2908931.
[43]H. Zhang, X. Wei, Y. Ding, Z. Jiang, and J. Ren, “A low noise capacitive MEMS accelerometer with anti-spring structure,” *Sensors and Actuators A: Physical*, vol. 296, pp. 79–86, Sep. 2019, doi: 10.1016/j.sna.2019.06.051.

[44]C. Zhao *et al.*, “Toward High-Resolution Inertial Sensors Employing Parametric Modulation in Coupled Micromechanical Resonators,” *Phys. Rev. Appl.*, vol. 12, no. 4, p. 044005, Oct. 2019, doi: 10.1103/PhysRevApplied.12.044005.
[45]S. Tang *et al.*, “A high-sensitivity MEMS gravimeter with a large dynamic range,” *Microsyst Nanoeng*, vol. 5, no. 1, Art. no. 1, Oct. 2019, doi: 10.1038/s41378-019-0089-7.
[46]B. El Mansouri *et al.*, “High-resolution MEMS inertial sensor combining large-displacement buckling behaviour with integrated capacitive readout,” *Microsyst Nanoeng*, vol. 5, no. 1, Art. no. 1, Dec. 2019, doi: 10.1038/s41378-019-0105-y.
[47]M. Zhao, K. Jiang, H. Bai, H. Wang, and X. Wei, “A MEMS based Fabry–Pérot accelerometer with high resolution,” *Microsyst Technol*, vol. 26, no. 6, pp. 1961–1969, Jun. 2020, doi: 10.1007/s00542-020-04747-3.
[48]M. A. Meldrum, “Application of vibrating beam technology to digital acceleration measurement,” *Sensors and Actuators A: Physical*, vol. 21, no. 1–3, pp. 377–380, Feb. 1990, doi: 10.1016/0924-4247(90)85075-F.
[49]C. Burrer and J. Esteve, “A novel resonant silicon accelerometer in bulk-micromachining technology,” *Sensors and Actuators, A: Physical*, vol. 46, no. 1–3, pp. 185–189, 1995, doi: 10.1016/0924-4247(94)00887-N.
[50]T. V. Roszhart, H. Jerman, J. Drake, and C. de Cotiis, “An Inertial-Grade, Micromachined Vibrating Beam Accelerometer,” in *Proceedings of the International Solid-State Sensors and Actuators Conference - TRANSDUCERS ’95*, Jun. 1995, pp. 656–658. doi: 10.1109/SENSOR.1995.721917.
[51]D. W. Burns, R. D. Horning, W. R. Herb, J. D. Zook, and H. Guckel, “Sealed-cavity resonant microbeam accelerometer,” *Sensors and Actuators A: Physical*, vol. 53, no. 1–3, pp. 249–255, May 1996, doi: 10.1016/0924-4247(96)01135-1.
[52]T. A. Roessig, R. T. Howe, A. P. Pisano, and J. H. Smith, “Surface-micromachined resonant accelerometer,” in *Proceedings of International Solid State Sensors and Actuators Conference (Transducers ’97)*, Jun. 1997, pp. 859–862 vol.2. doi: 10.1109/SENSOR.1997.635237.
[53]M. Aikele *et al.*, “Resonant accelerometer with self-test,” *Sensors and Actuators, A: Physical*, vol. 92, no. 1–3, pp. 161–167, Aug. 2001, doi: 10.1016/S0924-4247(01)00558-1.
[54]Seonho Seok, Sangkyung Seong, Byeungleul Lee, Jeongheon Kim, and Kukjin Chun, “A high performance mixed micromachined differential resonant accelerometer,” in *SENSORS, 2002 IEEE*, Jun. 2002, pp. 1058–1063 vol.2. doi: 10.1109/ICSENS.2002.1037259.
[55]A. A. Seshia *et al.*, “A vacuum packaged surface micromachined resonant accelerometer,” *Journal of Microelectromechanical Systems*, vol. 11, no. 6, pp. 784–793, Dec. 2002, doi: 10.1109/JMEMS.2002.805207.
[56]S. Sung, J. G. Lee, B. Lee, and T. Kang, “Design and performance test of an oscillation loop for a MEMS resonant accelerometer,” *Journal of Micromechanics and Microengineering*, vol. 13, no. 2, pp. 246–253, Jan. 2003, doi: 10.1088/0960-1317/13/2/312.
[57]D.-H. Hwang, K.-P. Chin, Y.-C. Lo, and W. Hsu, “Structure design of a 2-D high-aspect-ratio resonant microbeam accelerometer,” *Journal of Micro/Nanolithography, MEMS, and MOEMS*, vol. 4, no. 3, pp. 1–8, 2005, doi: 10.1117/1.2037070.
[58]V. Ferrari, A. Ghisla, D. Marioli, and A. Taroni, “Silicon resonant accelerometer with electronic compensation of input-output cross-talk,” *Sensors and Actuators A:*

Physical, vol. 123–124, pp. 258–266, 2005, doi: https://doi.org/10.1016/j.sna.2005.03.067.
[59]S. X. P. Su, H. S. Yang, and A. M. Agogino, “A resonant accelerometer with two-stage microleverage mechanisms fabricated by SOI-MEMS technology,” *IEEE Sensors Journal*, vol. 5, no. 6, pp. 1214–1222, Dec. 2005, doi: 10.1109/JSEN.2005.857876.
[60]L. He, Y. P. Xu, and M. Palaniapan, “A CMOS Readout Circuit for SOI Resonant Accelerometer With 4-$\mu\backslashrm g$ Bias Stability and 20-$ \mu\backslashrm g/\backslashsqrt{{\backslashhbox{Hz}}}$ Resolution,” *IEEE Journal of Solid-State Circuits*, vol. 43, no. 6, pp. 1480–1490, Jun. 2008, doi: 10.1109/JSSC.2008.923616.
[61]C. Comi, A. Corigliano, G. Langfelder, A. Longoni, A. Tocchio, and B. Simoni, “A new two-beam differential resonant micro accelerometer,” in *SENSORS, 2009 IEEE*, Oct. 2009, pp. 158–163. doi: 10.1109/ICSENS.2009.5398209.
[62]Y. Shang, J. Wang, S. Tu, and D. Chen, “A novel micromachined differential resonant accelerometer with flexural mechanisms fabricated by SOI-MEMS technology,” in *SENSORS, 2011 IEEE*, Oct. 2011, pp. 165–168. doi: 10.1109/ICSENS.2011.6127041.
[63]X. Zou, P. Thiruvenkatanathan, and A. A. Seshia, “Micro-electro-mechanical resonant tilt sensor with 250 nano-radian resolution,” in *2013 Joint European Frequency and Time Forum International Frequency Control Symposium (EFTF/IFC)*, Jul. 2013, pp. 54–57. doi: 10.1109/EFTF-IFC.2013.6702229.
[64]Y. Chiu, H. C. Hong, and P. C. Wu, “CMOS-MEMS accelerometer with differential LC-tank oscillators,” in *Proceedings of IEEE Sensors*, 2012. doi: 10.1109/ICSENS.2012.6411327.
[65]X. Guo-ming, Q. An-ping, S. Qin, and S. Yan, “Test and evaluation of a silicon resonant accelerometer implemented in SOI technology,” in *SENSORS, 2013 IEEE*, Nov. 2013, pp. 1–4. doi: 10.1109/ICSENS.2013.6688238.
[66]A. Caspani, C. Comi, A. Corigliano, G. Langfelder, and A. Tocchio, “Compact biaxial micromachined resonant accelerometer,” *Journal of Micromechanics and Microengineering*, vol. 23, no. 10, p. 105012, Sep. 2013, doi: 10.1088/0960-1317/23/10/105012.
[67]A. A. Trusov, S. A. Zotov, B. R. Simon, and A. M. Shkel, “Silicon accelerometer with differential Frequency Modulation and continuous self-calibration,” in *Proceedings of the IEEE International Conference on Micro Electro Mechanical Systems (MEMS)*, 2013, pp. 29–32. doi: 10.1109/MEMSYS.2013.6474168.
[68]A. Caspani, C. Comi, A. Corigliano, G. Langfelder, V. Zega, and S. Zerbini, “A differential resonant micro accelerometer for out-of-plane measurements,” in *Procedia Engineering*, 2014. doi: 10.1016/j.proeng.2014.11.569.
[69]B. Yang, B. Dai, H. Zhao, and X. Liu, “A new silicon triaxial resonant micro-accelerometer,” in *2014 International Conference on Information Science, Electronics and Electrical Engineering*, Apr. 2014, pp. 1283–1286. doi: 10.1109/InfoSEEE.2014.6947878.
[70]H. Ding, J. Zhao, B.-F. Ju, and J. Xie, “A high-sensitivity biaxial resonant accelerometer with two-stage microleverage mechanisms,” *Journal of Micromechanics and Microengineering*, vol. 26, no. 1, p. 15011, Dec. 2015, doi: 10.1088/0960-1317/26/1/015011.

[71]J. Zhang, Y. Su, Q. Shi, and A.-P. Qiu, “Microelectromechanical Resonant Accelerometer Designed with a High Sensitivity,” *Sensors*, vol. 15, no. 12, pp. 30293–30310, Dec. 2015, doi: 10.3390/s151229803.
[72]Q. Zhang, S. Y. Zhou, Z. Y. Ju, and L. B. Huang, “A High-Sensitivity Micromechanical Silicon Resonant Accelerometer without Mechanical Coupling,” *Applied Mechanics and Materials*, vol. 741, pp. 333–339, Mar. 2015, doi: 10.4028/www.scientific.net/AMM.741.333.
[73]X. Zou and A. A. Seshia, “A high-resolution resonant MEMS accelerometer,” in *2015 Transducers - 2015 18th International Conference on Solid-State Sensors, Actuators and Microsystems (TRANSDUCERS)*, Jun. 2015, pp. 1247–1250. doi: 10.1109/TRANSDUCERS.2015.7181156.
[74]F. Edalatfar, S. Hajhashemi, B. Yaghootkar, and B. Bahreyni, “Dual mode resonant capacitive MEMS accelerometer,” in *2016 IEEE International Symposium on Inertial Sensors and Systems*, Feb. 2016, pp. 97–100. doi: 10.1109/ISISS.2016.7435554.
[75]J. Zhang, Q. Shi, Y. Su, and A. Qiu, “Energy method for the optimization of a silicon resonant accelerometer,” in *2016 IEEE International Instrumentation and Measurement Technology Conference Proceedings*, May 2016, pp. 1–6. doi: 10.1109/I2MTC.2016.7520377.
[76]J. Zhao *et al.*, “A 0.23- $\mu\backslashtext{g}$ Bias Instability and 1- $\mu\backslashtext{g}/\backslashsurd $ Hz Acceleration Noise Density Silicon Oscillating Accelerometer With Embedded Frequency-to-Digital Converter in PLL,” *IEEE Journal of Solid-State Circuits*, vol. 52, no. 4, pp. 1053–1065, Apr. 2017, doi: 10.1109/JSSC.2016.2645613.
[77]X. Wang *et al.*, “A 0.4 $\mu\backslashtext{g}$ Bias Instability and 1.2 $\mu\backslashtext{g}/\backslashsurd $ Hz Noise Floor MEMS Silicon Oscillating Accelerometer With CMOS Readout Circuit,” *IEEE Journal of Solid-State Circuits*, vol. 52, no. 2, pp. 472–482, Feb. 2017, doi: 10.1109/JSSC.2016.2609385.
[78]E. E. Moreira, B. Kuhlmann, J. Gaspar, and L. A. Rocha, “Small Size And Highly Sensitive Differential MEMS Accelerometer Based On Double-Ended Tuning Fork Resonators,” in *2019 20th International Conference on Solid-State Sensors, Actuators and Microsystems Eurosensors XXXIII (TRANSDUCERS EUROSENSORS XXXIII)*, Jun. 2019, pp. 602–605. doi: 10.1109/TRANSDUCERS.2019.8808174.
[79]M. Pandit *et al.*, “An Ultra-High Resolution Resonant MEMS Accelerometer,” in *2019 IEEE 32nd International Conference on Micro Electro Mechanical Systems (MEMS)*, Seoul, Korea (South): IEEE, Jan. 2019, pp. 664–667. doi: 10.1109/MEMSYS.2019.8870734.
[80]M. Pandit *et al.*, “A 10 NANO-G/RT-HZ RESONANT MEMS ACCELEROMETER EMPLOYING ANTI-ALIASING CONTROL,” in *2021 IEEE International Symposium on Inertial Sensors and Systems (INERTIAL)*, Mar. 2021, pp. 1–4. doi: 10.1109/INERTIAL51137.2021.9430455.
[81]I. B. Bahadur, J. Mills, and Y. Sun, “Design of a MEMS-based resonant force sensor for compliant, passive microgripping,” in *IEEE International Conference Mechatronics and Automation, 2005*, Jul. 2005, pp. 77-82 Vol. 1. doi: 10.1109/ICMA.2005.1626526.
[82]B. Bahreyni and C. Shafai, “A Resonant Micromachined Magnetic Field Sensor,” *IEEE Sensors Journal*, vol. 7, no. 9, pp. 1326–1334, Sep. 2007, doi: 10.1109/JSEN.2007.902945.

[83]K. Ikeda *et al.*, “Silicon pressure sensor integrates resonant strain gauge on diaphragm,” *Sensors and Actuators A: Physical*, vol. 21, no. 1, pp. 146–150, Feb. 1990, doi: 10.1016/0924-4247(90)85028-3.
[84]H. A. C. Tilmans, M. Elwenspoek, and J. H. J. Fluitman, “Micro resonant force gauges,” *Sensors and Actuators A: Physical*, vol. 30, no. 1, pp. 35–53, Jan. 1992, doi: 10.1016/0924-4247(92)80194-8.
[85]R. Abdolvand, B. Bahreyni, J. Lee, and F. Nabki, “Micromachined Resonators: A Review,” *Micromachines*, vol. 7, no. 9, p. 160, Sep. 2016, doi: 10.3390/mi7090160.
[86]João Fernandes da Silva, Lucas Allende Dias do Nascimento, and Simone dos Santos Hoefel, “Free vibration analysis of Euler-Bernoulli beams under non-classical boundary conditions,” presented at the IX Congresso Nacional de Engenharia Mecânica, Fortaleza, Ceará, Brasil, 2016. doi: 10.20906/CPS/CON-2016-1053.
[87]C. Zhao *et al.*, “A Resonant MEMS Accelerometer With 56ng Bias Stability and 98ng/Hz1/2 Noise Floor,” *Journal of Microelectromechanical Systems*, vol. 28, no. 3, pp. 324–326, Jun. 2019, doi: 10.1109/JMEMS.2019.2908931.
[88]Y. Li, B. Jin, M. Zhao, and F. Yang, “Design and Optimization of the Resonator in a Resonant Accelerometer Based on Mode and Frequency Analysis,” *Micromachines*, vol. 12, no. 5, Art. no. 5, May 2021, doi: 10.3390/mi12050530.
[89]K. Azgin and L. Valdevit, “The effects of tine coupling and geometrical imperfections on the response of DETF resonators,” *J. Micromech. Microeng.*, vol. 23, no. 12, p. 125011, Oct. 2013, doi: 10.1088/0960-1317/23/12/125011.
[90]T. A. W. Roessig, “Integrated MEMS tuning fork oscillators for sensor applications,” Ph.D., University of California, Berkeley, United States -- California, 1998. Accessed: May 29, 2023. [Online]. Available: https://www.proquest.com/docview/304422534/abstract/521AFEA3E35D4A53PQ/1
[91]H. Ding, X. Le, and J. Xie, “A MEMS Fishbone-Shaped Electrostatic Double-Ended Tuning Fork Resonator With Selectable Higher Modes,” *Journal of Microelectromechanical Systems*, vol. 26, no. 4, pp. 793–801, Aug. 2017, doi: 10.1109/JMEMS.2017.2695665.
[92]S.-S. Li, Y.-W. Lin, Y. Xie, Z. Ren, and C. T.-C. Nguyen, “Micromechanical ‘hollow-disk’ ring resonators,” in *17th IEEE International Conference on Micro Electro Mechanical Systems. Maastricht MEMS 2004 Technical Digest*, Jan. 2004, pp. 821–824. doi: 10.1109/MEMS.2004.1290711.
[93]K. Wang, A.-C. Wong, and C. T.-C. Nguyen, “VHF free-free beam high-Q micromechanical resonators,” *Journal of Microelectromechanical Systems*, vol. 9, no. 3, pp. 347–360, Sep. 2000, doi: 10.1109/84.870061.
[94]M. U. Demirci and C. T.-C. Nguyen, “Higher-mode free-free beam micromechanical resonators,” in *IEEE International Frequency Control Symposium and PDA Exhibition Jointly with the 17th European Frequency and Time Forum, 2003. Proceedings of the 2003*, May 2003, pp. 810–818. doi: 10.1109/FREQ.2003.1275195.
[95]W.-T. Hsu, J. R. Clark, and C. T.-C. Nguyen, “Q-Optimized Lateral Free-Free Beam Micromechanical Resonators,” in *Transducers ’01 Eurosensors XV*, E. Obermeier, Ed., Berlin, Heidelberg: Springer, 2001, pp. 1082–1085. doi: 10.1007/978-3-642-59497-7_256.
[96]L. C. Shao, M. Palaniapan, W. W. Tan, and L. Khine, “Nonlinearity in micromechanical free–free beam resonators: modeling and experimental

verification," *J. Micromech. Microeng.*, vol. 18, no. 2, p. 025017, Jan. 2008, doi: 10.1088/0960-1317/18/2/025017.
[97] M. Okada, H. Nagasaki, A. Tamano, K. Niki, H. Tanigawa, and K. Suzuki, "Silicon Beam Resonator Utilizing the Third-Order Bending Mode," *Jpn. J. Appl. Phys.*, vol. 48, no. 6S, p. 06FK03, Jun. 2009, doi: 10.1143/JJAP.48.06FK03.
[98] S. Kuroda, N. Suzuki, H. Tanigawa, and K. Suzuki, "Variable Resonance Frequency Selection for Fishbone-Shaped Microelectromechanical System Resonator Based on Multi-Physics Simulation," *Jpn. J. Appl. Phys.*, vol. 52, no. 6S, p. 06GL14, Jun. 2013, doi: 10.7567/JJAP.52.06GL14.
[99] N. Suzuki, H. Tanigawa, and K. Suzuki, "Higher-order vibrational mode frequency tuning utilizing fishbone-shaped microelectromechanical systems resonator," *J. Micromech. Microeng.*, vol. 23, no. 4, p. 045018, Mar. 2013, doi: 10.1088/0960-1317/23/4/045018.
[100] P. Hauptmann, "Resonant sensors and applications," *Sensors and Actuators A: Physical*, vol. 26, no. 1–3, pp. 371–377, Mar. 1991, doi: 10.1016/0924-4247(91)87018-X.
[101] P. E. Allen and D. R. Holberg, *CMOS analog circuit design*, 3rd ed. in The Oxford series in electrical and computer engineering. New York ; Oxford: Oxford University Press, USA, 2012.
[102] "CoventorWare," Coventor. Accessed: Apr. 17, 2023. [Online]. Available: https://www.coventor.com/products/coventormp/coventorware/
[103] "MEMSCAP | About MEMSCAP®." Accessed: Apr. 17, 2023. [Online]. Available: http://www.memscap.com/company/about-memscap
[104] E. Ghaderi and B. Bahreyni, "Synchronous Demodulation for Low Noise Measurements," *IEEE Instrumentation & Measurement Magazine*, vol. 24, no. 2, pp. 72–78, Apr. 2021, doi: 10.1109/MIM.2021.9400956.
[105] X.-P. S. Su and H. S. Yang, "Design of compliant microleverage mechanisms," *Sensors and Actuators A: Physical*, vol. 87, no. 3, pp. 146–156, 2001, doi: https://doi.org/10.1016/S0924-4247(00)00488-X.
[106] X.-P. S. Su and H. S. Yang, "Single-stage microleverage mechanism optimization in a resonant accelerometer," *Structural and Multidisciplinary Optimization*, vol. 21, no. 3, pp. 246–252, 2001, doi: 10.1007/s001580050189.
[107] X.-P. S. Su and H. S. Yang, "Single-stage microleverage mechanism optimization in a resonant accelerometer," *Structural and Multidisciplinary Optimization*, vol. 21, no. 3, pp. 246–252, 2001, doi: 10.1007/s001580050189.
[108] X.-P. S. Su and H. S. Yang, "Design of compliant microleverage mechanisms," *Sensors and Actuators A: Physical*, vol. 87, no. 3, pp. 146–156, 2001, doi: https://doi.org/10.1016/S0924-4247(00)00488-X.
[109] F. Chen, J. Cai, W. Dong, and Z. Du, "A Generalized Mathematical Model for the Bridge-Type and Lever-Type Mechanism," in *Intelligent Robotics and Applications*, H. Yu, J. Liu, L. Liu, Z. Ju, Y. Liu, and D. Zhou, Eds., in Lecture Notes in Computer Science. Cham: Springer International Publishing, 2019, pp. 296–309. doi: 10.1007/978-3-030-27526-6_26.
[110] P. Schmitt and M. Hoffmann, "Engineering a Compliant Mechanical Amplifier for MEMS Sensor Applications," *Journal of Microelectromechanical Systems*, vol. 29, no. 2, pp. 214–227, Apr. 2020, doi: 10.1109/JMEMS.2020.2965260.
[111] Z. Fang, Y. Yin, C. Chen, S. Zhang, Y. Liu, and F. Han, "A sensitive micromachined resonant accelerometer for moving-base gravimetry," *Sensors and*

Actuators A: Physical, vol. 325, p. 112694, Jul. 2021, doi: 10.1016/j.sna.2021.112694.
[112] K. Kocak and C. Yilmaz, “Design of a compliant lever-type passive vibration isolator with quasi-zero-stiffness mechanism,” *Journal of Sound and Vibration*, vol. 558, p. 117758, Aug. 2023, doi: 10.1016/j.jsv.2023.117758.
[113] X.-P. S. Su, “Compliant leverage mechanism design for MEMS applications,” Ph.D., University of California, Berkeley, United States -- California, 2001. Accessed: Jul. 18, 2023. [Online]. Available: https://www.proquest.com/docview/304685202/abstract/BCED80AE6EF34BF5PQ/1
[114] W. P. Robins, “Phase Noise in Signal Sources.pdf.” London, 1982.

Appendix A.

Details of Fabrication Process

Step Number	Description	Substeps	Parametes	Result	Equipment
1	RCA clean		RCA1 and RCA2 for all wafers, HF dip for Si	Clean wafers.	Acid Bench
2	Wafer oxidation		N/A	2um of oxide grown on top of both sides	Tube furnance
3	Front mask	Hot plate	10 min at 180C		Hot plate
		HMDS priming	10 min		Organic bench
		Photoresist deposition	60 sec at 1200rpm	2um of PR on front side	Spin coater
		Soft bake	60 sec at 90C		Hot plate
		Hard bake	60 sec at 110C		Hot plate
		Delay	10 min	Photoresist dehidration	
		Mask Processing	82 mj/cm2		Mask Aligner
		Postexpose bake	60 sec at 110C		Hot plate
		Developing	52 sec at developer (MIF 300)		Developing bench
		Water clean		Cleaned photoresit mask with thickness ~ 1.8 um	Developing bench
4	Front mask etch		RIE etch of oxide layer. 600 sec. Oxide recipe	Etched wafer	DRIE tool
5	Wafer clean	Plasma strip	5 min at 280 uTorr and 300 Watt		Plasma striper
		Wet clean	1165 PR remover, Water, Aceton bath, IPA	Cleaned wafer	Wet bench
6	Front side protection layer	Hot plate	10 min at 180C		Hot plate
		HMDS priming	10 min		Organic bench
		Photoresist deposition	60 sec at 1200rpm	2um of PR on front side	Spin coater
		Soft bake	60 sec at 90C		Hot plate
		Hard bake	30 sec at 120C		Hot plate
7	Back side mask	Hot plate	10 min at 180C		Hot plate
		HMDS priming	10 min		Organic bench
		Photoresist deposition	60 sec at 1200rpm	2um of PR on front side	Spin coater
		Soft bake	60 sec at 90C		Hot plate
		Hard bake	60 sec at 110C		Hot plate
		Delay	10 min	Photoresist dehidration	
		Mask Processing	82 mj/cm2		Mask Aligner
		Postexpose bake	60 sec at 110C		Hot plate
		Developing	52 sec at developer (MIF 300)		Developing bench
		Water clean		Cleaned photoresit mask with thickness ~ 1.8 um	Developing bench
8	Back side etch	Oxide etch	RIE etch of oxide layer. 600 sec. Oxide recipe		DRIE tool
		Silicon etch	DRIE of Sicicon. Large area recipe. 330 cycles	Etched up to oxide layer (400um from back side)	DRIE tool
9	Wafer clean	Plasma strip	10 min at 280 uTorr and 300 Watt		Plasma striper
		Wet clean	1165 PR remover, Water, Aceton bath, IPA	Cleaned wafer	Wet bench
10	Front side etch	Si etch	DRIE of Sicicon. Large area recipe. 330 cycles	Etched up to oxide layer (400um from back side)	DRIE tool
		Oxygen clean	Oxygen plasma clean		DRIE tool
11	Wafer cut		Cleaving wafer on quarters	4 parts	Cleaving area
12	VHF release	Oxygen plasma front side	20 min at 280mTorr and 300Watt		Plasma stiper
		Release	VHF 2 hours at 40C	Released Chips	Acid bench

Appendix B.

Phase Noise in Multiplier

An oscillator is designed to deliver a consistent sinusoidal voltage output. However, in practical scenarios, the output experiences variations in both magnitude and phase, leading to instability. Such deviations in phase disrupt the precision of the signal's periodic intersections with the zero-value axis, contributing to phase noise. This phase noise primarily arises from two sources: the thermal noise floor, which maintains a relatively uniform level across different frequencies, and flicker noise, which is inherent to most electronic devices and decreases in intensity as the frequency increases, following an inverse relationship.

The output voltage of an oscillator can be described by Equation (1):

$$V(t) = (A_0 + a_n(t)) \sin(2\pi f_0 t + \psi_n(t)) \tag{1.B}$$

where A_0 is the nominal peak voltage amplitude, $a_n(t)$ is the deviation from the nominal amplitude A_0, f_0 is the nominal frequency and $\psi_n(t)$ is the phase deviation from the nominal phase $2\pi f_0 t$. These deviations cause the power to be propagated at frequencies near to the nominal frequency. As a result, the power spectral density departs from the Delta function, which is ideal for an oscillator. Figure B.1 shows the power spectral density of an oscillator.

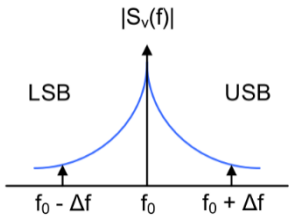

Figure B.1 Power spectral density of an oscillator

Phase noise is phase fluctuations of an oscillator. In other words, phase noise is just Phase Modulation (PM) with the noise being the message signal. Single sideband phase noise $L(f)$ is the power density of the noise sideband relative to the power of the carrier:

$$L(f) = \frac{\text{power of phase noise modulation sideband}}{\text{power of carrier}}$$

In the frequency domain, as depicted in Figure B.2, a PM modulated signal has an infinite number of sidebands. Bessel functions can be used to determine the amplitude of these sidebands. Equation (2.B) shows the relation between PM modulated signal and the sidebands where β is maximum phase deviation, and J_k are the Bessel functions of the first kind.

$$\cos(2\pi f_c t + \beta \sin(2\pi f_m t)) = \sum_{k=-\infty}^{+\infty} J_k(\beta) \cos(2\pi(f_c + k f_m)t) \tag{2.B}$$

Figure B.3 shows the first four Bessel functions of the first kind versus the peak phase deviation β of the modulating signal. Using Bessel function properties, we can convert the peak phase deviation to a power ratio as well

$$\frac{P_{SSB}}{P_C} = \left(\frac{V_{SSB}}{V_C}\right)^2 = \left(\frac{1}{2}\beta\right)^2 \tag{3.B}$$

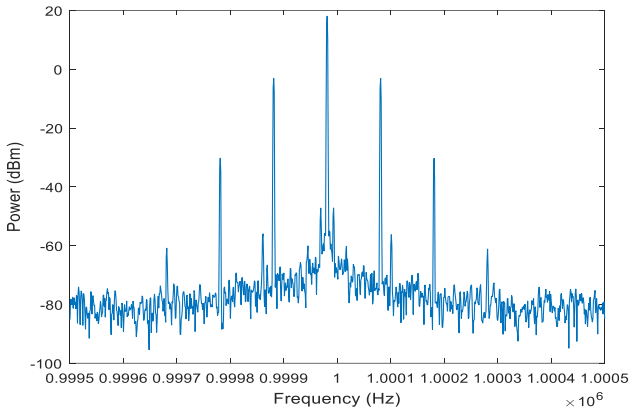

Figure B.2 A measured PM modulated signal with several sidebands

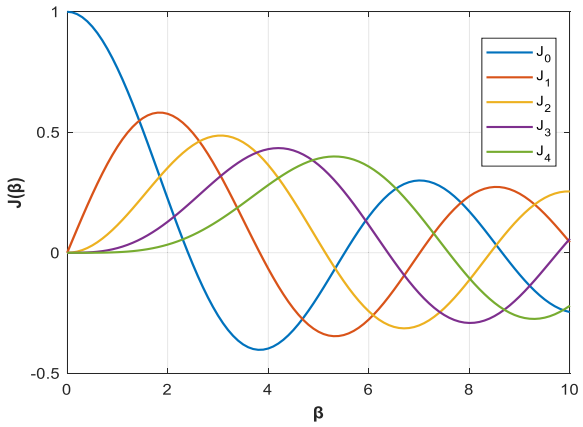

Figure B.3 Bessel function of the first kind

Oscillators have traditionally played a crucial role in the architecture of integrated circuits and the domain of communications. Consequently, the development of phase noise models for oscillators predominantly focused on the phase noise present in the electronic elements of oscillator circuits. We employ a straightforward mathematical method to model phase noise, basing it on the fundamental concept of phase noise itself. This section outlines formulas that link noise near the carrier frequency in modulated signals to the outcome of synchronous demodulation, with an emphasis on measurement scenarios. To illustrate this, we reference a basic representation of a synchronous demodulator as shown in Figure B.4. In this model, $H(j\omega)$ corresponds to the transfer function of the Device Under Test (DUT) combined with an amplifier, $\Delta\phi$ symbolizes the phase shifter's function, and W_0 denotes the environmental noise infiltrating the system.

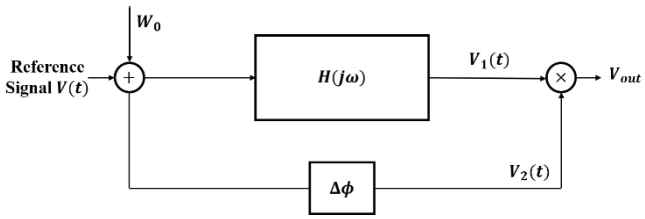

Figure B.4 Synchronous demodulator model.

To derive the mathematical expression for the output voltage of an oscillator with phase noise, we use Equation (1) for describing the reference signal. Since we investigate the effect of the phase noise, we assume that the amplitude fluctuations are negligible. This means $a(t)$ is zero. For describing the phase noise and phase fluctuations, we use the

sinusoidal representation of narrowband noise [114]; thus, the equation for the noise signal can be written as:

$$\psi_n(t) = \sqrt{2n_0}\sin(2\pi f_m t + \varphi_0) \tag{4.B}$$

where $\psi_n(t)$ is the noise in phase, n_0 is the noise power at any time, which is unpredictable and ϕ_0 is the relative noise angle. Nevertheless, when our interest is the long term mean power distribution, which is usually the case, then we may write:

$$\Psi_n(t) = \sqrt{2N_0}\sin(2\pi f_m t + \phi_n) \tag{5.B}$$

where $\Psi_n(t)$is the instantaneous value of the sinusoid corresponding to long-term RMS value N_0. Φ is an unpredictable term. For most purposes, Equation (5) is more useful than Equation (4). Hence, the output voltage of the oscillator can be described as:

$$V(t) = \sqrt{2C}\sin(2\pi f_0 t + 2\sqrt{\frac{N}{C}}\sin(2\pi f_m t + \phi_n)) \tag{6.B}$$

Where we assumed that C is the power of the carrier and N is the power of the sideband phase noise at the side frequency f_m. It is worth mentioning that the value of f_m is arbitrary; for this reason, this model can be used to analyze the contribution of any close-to-carrier phase noise sideband to the output signal of synchronous demodulator.

The reference signal described in Equation (6.B) is applied to the synchronous demodulator shown in Figure 4. We have two signals at the multiplier with their phase noise defined as narrowband PM at the frequency modulation of f_m. The expression for the signals $V_1(t)$ and $V_2(t)$, Figure 4.B, are presented in Equations (7.B) and (8.B) respectively. In these equations, $\Delta\omega$ is the phase shift introduced by the transfer function of the DUT and amplifiers, τ is used to model any delay effects, W is the effect of the input noise, ϕ_{n1} and ϕ_{n2} are independent and unpredictable phase fluctuations, $N_0 = 2N$, and J_k are the Bessel functions of the first kind. We use the Bessel function expansion method because it provides a better understanding of different sidebands contributing to the total signal.

$$V_1(t) = W + B\,cos\left(2\pi f_c(t-\tau) + \Delta\omega + \sqrt{2\frac{N_0}{C}}sin(2\pi f_m(t-\tau) + \phi_{n1})\right)$$
$$= W + B\sum_{k1} J_{k1}\left(\sqrt{2\frac{N_0}{C}}\right)cos\left(2\pi f_c t + \Delta\omega + k_1(2\pi f_m(t-\tau) + \phi_{n1})\right) \quad (7.B)$$

$$V_2(t) = A\,cos\left(2\pi f_c t + \Delta\phi + \sqrt{2\frac{N_0}{C}}sin(2\pi f_m t + \phi_{n2})\right)$$
$$= A\sum_{k2} J_{k2}\left(\sqrt{2\frac{N_0}{C}}\right)cos\left(2\pi f_c t + \Delta\phi + k_2(2\pi f_m t + \phi_{n2})\right) \quad (8.B)$$

By multiplying signals described in Equations (7.B) and (8.B) and using the following trigonometric identity:

$$\sin(\alpha)\times\sin(\beta) = \frac{1}{2}[\cos(\alpha-\beta) - \cos(\alpha+\beta)] \quad (9.B)$$

We obtain two terms from equation (9.B), the first term is the sideband signals close to DC and the second term is the sideband signals close $2f_c$. Since the signal is filtered after multiplication, we are interested in the sidebands close to DC. For small values of N_0/C such as those that occur in random noise modulation, we have:

$$J_0\left(\sqrt{2\frac{N_0}{C}}\right) \cong 1 \quad (10.1.B)$$

$$J_1\left(\sqrt{2\frac{N_0}{C}}\right) \cong \frac{\sqrt{2\frac{N_0}{C}}}{2} \quad (10.2.B)$$

$$J_2\left(\sqrt{2\frac{N_0}{C}}\right) \cong J_3\left(\sqrt{2\frac{N_0}{C}}\right) \cong \cdots \cong 0 \quad (10.3.B)$$

$$J_{-n}\left(\sqrt{2\frac{N_0}{C}}\right) = (-1)^n J(\sqrt{2\frac{N_0}{C}}) \qquad (10.4.B)$$

Thus, the 'k' value in the expansion term ranges between -1 and 1. Furthermore, it is acceptable to disregard any second-order terms of N_0/C due to their insignificance. By applying the equations and simplifications, we are able to determine the low-frequency elements of the sychronous demodulator's output. This is detailed in Equation (11.B). The output is comprised of two elements: the first is the direct current (DC) part, and the second is a sideband frequency created by phase modulation (PM) of the narrowband phase noise at the frequency f_m. In this context, $\Delta\theta$ represents the cumulative phase variation between $V_1\,(t)$ and $V_2(t)$, arising from phase alterations in both the transfer function and phase shifter, as well as any latency present within the system.Equation (11.B) offers a prediction of how phase noise from the local oscillator affects the noise output of the system at the side frequency f_m. The magnitude of this component is related to the sine of half the difference between ϕ_{n1} and ϕ_{n2}, which are erratic phase deviations, rendering the term's value unpredictable. Nonetheless, $\Delta\theta$ within the sine function is contingent on the design and parameters of the system. Minimizing the phase noise's impact on the output can be achieved by reducing the phase differential between $V_1(t)$ and $V_2(t)$, particularly through the precise adjustment of $\Delta\phi$ in the phase shifter.

$$2AB\left(\frac{1}{2}\cos(\Delta\theta) + \sqrt{\frac{N_0}{2C}}\sin(\Delta\theta)\sin\left(\frac{\phi_{n1}-\phi_{n2}}{2}\right)\cos(2\pi f_m t + \frac{\phi_{n1}+\phi_{n2}}{2})\right) \qquad (11.B)$$